Cloud-resolving simulations of the August 2005 Alpine flood

The sensitivity to microphysics parameterizations

A diploma thesis submitted to the

Institute of Meteorology and Geophysics,
University of Innsbruck

for the degree of

Master of Natural Science

presented by

Wolfgang Langhans

November 2008

Abstract

The sensitivity of two specific mechanisms of orographic precipitation to the parameterization of microphysics in a mesoscale numerical model is investigated. In this study the National Center for Atmospheric Research Weather Research and Forecasting (WRF) model is utilized with a cloud-resolving setup, in order to simulate the heavy Alpine precipitation event on 21-23 August 2005. The numerical simulations are validated against rain gauge observations and radar measurements.

Results show that WRF is capable of reproducing observed precipitation structures, but underpredicts heavy precipitation over the Alpine rim during 22 August 2005. Two characteristic mechanisms of orographic precipitation have been determined during the event. Firstly, embedded cellular convection enhances the precipitation over the Alpine foreland during the second half of 21 August 2005. Secondly, moist stable stratified flow directed perpendicular to the main Alpine barrier produces large amounts of precipitation over the northern Alpine flanks between the evening of 22 August 2005 and the morning of 23 August 2005.

A series of experiments are conducted using different microphysics schemes: two schemes with a graupel category (WSM6* and Thompson), a scheme without graupel (WSM5*), and a Kessler warm rain scheme. During both periods the WSM6* scheme produces the largest precipitation amounts, followed by the WSM5*, Thompson, and Kessler scheme. In comparison to the WSM6*, the WSM5* scheme causes a systematic displacement of the small-scale precipitation during the second period, but significant modifications to the domain-averaged precipitation are not achieved. The Thompson scheme predicts considerably less graupel mass than the WSM6* scheme. Instead, more snow is produced, which is however located at higher altitudes and thereby limits the amount of potentially available snow for melting below the freezing level. The Kessler scheme produces only small amounts of convective precipitation over the Alpine foreland during the first period and also predicts significantly less preciptiation than the other schemes during the second period due to relatively small autoconversion rates.

Additional microphysical sensitivity experiments with slightly modified cloud characteristics reveal an insensitivity of the precipitation field and suggest a larger influence of moist convection on the numerical predictability during the first period.

Contents

Chapter 1

Introduction

1.1 Motivation

Precipitation climatologies over the European Alps show large moist anomalies along their flanks and foothills (Frei and Schär 1998). The provided water constitutes the necessary supply for agricultural and economic sectors. Unfortunately, heavy Alpine precipitation events can result in severe landslides and damage in dense populated Alpine areas.

Between midday 21 August 2005 and the afternoon of 23 August 2005 heavy precipitation over Swiss, Austrian, and German Alpine regions led to damaging flooding. Record-breaking values of accumulated precipitation were obtained over the northern Alpine slopes in central Switzerland during 21 August 2005 and heavy precipitation far beyond a climatologic mean occurred during 22 August 2005 over eastern Switzerland and the northern Alpine flanks in Austria and Germany. Besides devastating impacts in Switzerland, the Austrian province of Vorarlberg suffered damages of 178 million euros (Amt der Vorarlberger Landesregierung 2005). In southern Germany the federal state of Bavaria claimed damages of about 189 millions of Euros (Bayerisches Staatsministerium für Umwelt, Gesundheit und Verbraucherschutz 2006). The total economic costs have been estimated at 3.3 billion US dollars and even 49 casualties were reported (SwissRe 2006).

MeteoSchweiz (2006b) conducted a numerical sensitivity study in order to test the importance of orographic lifting during this event and showed that the Alpine topography significantly increased the precipitation amount compared to a flatened topography. However, several different mechanisms of orographic precipitation exist, which modify both the precipitation amount and its spatial distribution. A chronological analysis of radar measurements over Switzerland (MeteoSchweiz 2006b) revealed a shift of the heavy precipitation from central Switzerland and its adjacent Alpine foreland on 21 August 2005 to the main Alpine crest in eastern Switzerland

on 22 August 2005. This displacement of precipitation is in agreement with an eastward propagation of a surface depression, but the spatial distribution of precipitation also changed due to changing mechanisms of precipitation formation. As mentioned in Zängl (2007c) and shown in Hohenegger et al. (2008), embedded convection was triggered in a moist static unstable environment during the first half of the event, while moist neutrally stratified upslope orographic precipitation has been seen as the dominating mechanism at a later stage of the precipitation event (Zängl 2007b). In this study the involved mechanisms are depicted from realistic simulations with a numerical mesoscale forecasting model. As previous studies, which will be reviewed in section 1.2, showed a large sensitivity on microphysics, special attention will be given to the influence of its parameterizations on the prediction of small-scale precipitation patterns during periods with distinctive mechanisms.

1.2 A short review of previous research

In its simplest form orographic precipitation results from stable ascent induced over mountains. This can be seen as a primary mechanism for orographic precipitation (see Fig. 1.1a). The lifting of the moist air mass causes its cooling. The subsequent condensation rate of water vapor is proportional to the steepness of the slope (Smith 1979). If a fluid with high static stability impinges on a topographic obstacle, the flow can be blocked and deflected around the obstacle. For the Alpine barrier Schneidereit and Schär (2000) demonstrated that an asymmetry of flow-regimes introduced by the Coriolis force results in the lifting of the air mass over the western Alps. Later Rotunno and Ferretti (2001) showed that partial blocking of the air mass led to an increase of precipitation on the southside of the Alps during the Piedmont heavy precipitation event in 1994. Additionally, they conducted idealized simulations and considered a horizontal gradient of saturation deficit that led to partial blocking of the unsaturated airstream (see Fig. 1.1b), while the saturated airstream, which was characterized by decreased moist static stability due to latent heating, surmounted the Alpine barrier. Finally, the resulting low-level convergence led to precipitation enhancement due to an increased lifting of the saturated airstream. Colle (2004) conducted two-dimensional idealized simulations of moist flow past a bell-shaped ridge and demonstrated that the maximum of the surface precipitation shifts rapidly upstream as soon as upstream flow blocking occurs (see Fig. 1.1b), while the precipitation over the windward slope slightly decreases. He also showed that with a higher freezing level the precipitation peak shifts from the mountain top to the windward slope, as ice hydrometeors with lower fall speeds cause a delay of the precipitation fallout. Medina et al. (2005) and Houze and Medina (2005) investigated cross-barrier flows during frontal precipitation events over the Alps during

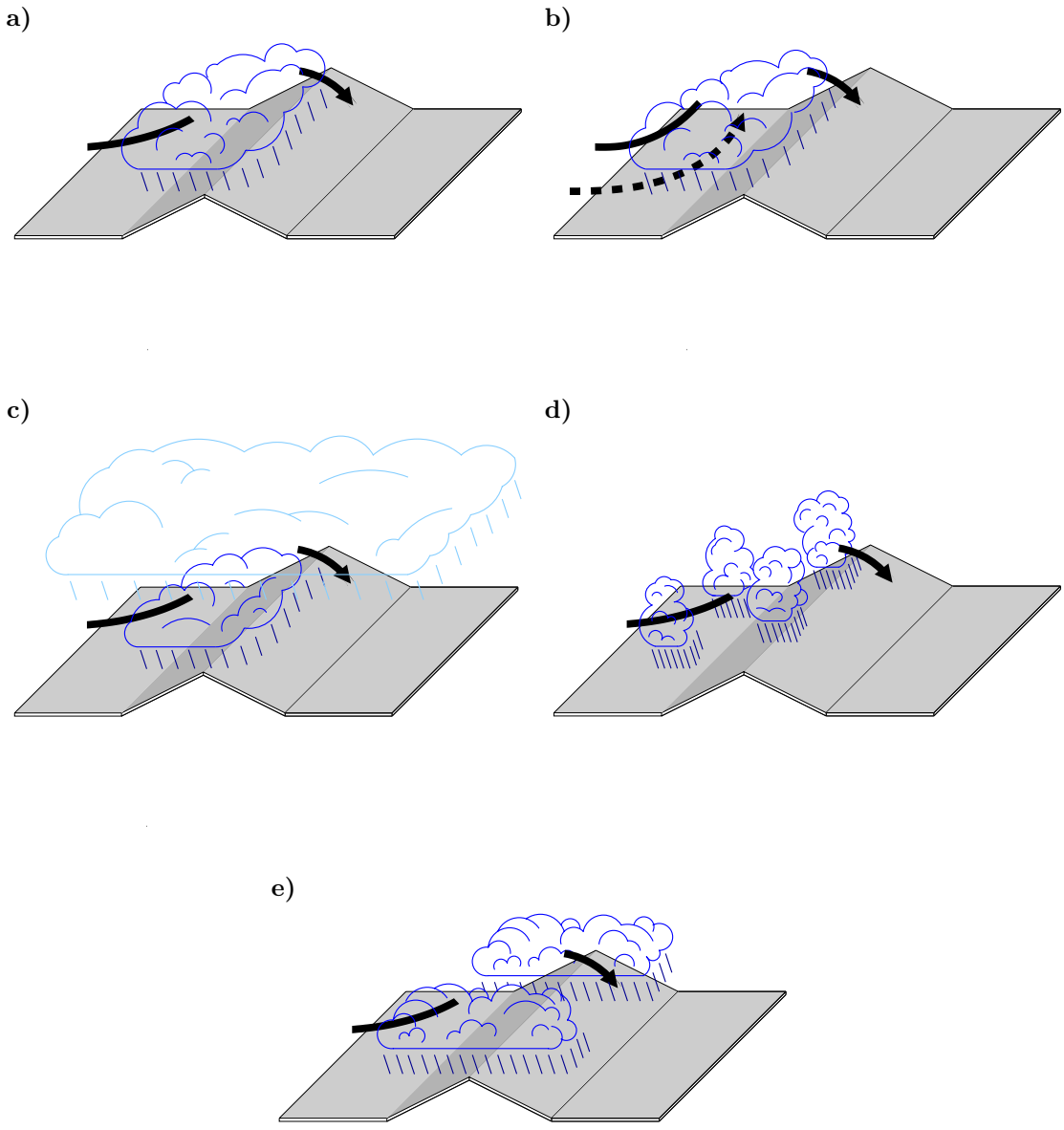

Figure 1.1: Overview of mechanisms of orographic precipitation: (a) stable stratified upslope precipitation, (b) partial blocking of the flow, (c) seeder-feeder process, (d) embedded cellular convection, and (e) stationary banded convection.

MAP (Bougeault et al. 2001) and over the Cascade Mountains of Oregon during IMPROVE-2 (Stoelinga et al. 2003). The authors concluded that flow decoupling due to sufficiently stable upslope flow conditions generates a pronounced layer of vertical wind shear. The layer is characterized by small-scale turbulent fluctuations of the vertical velocity in regions with a low Richardson number over the windward slope of the mountains, where the orographic precipitation is enhanced. The so-called seeder-feeder process, which causes enhanced precipitation due to the washout of a low-level, orographic cloud by rain drops or ice crystals falling from a high-level cloud (Bader and Roach 1977; Bergeron 1959), is sketched in Fig. 1.1c. A similar mechanism is explained in Zängl (2007b), who addressed both the influence of a frontal upper-level ice cloud on riming in an orographic cloud and the advection of hydrometeors to the lee side of mountains. The latter causes a downstream displacement of precipitation, when wind speeds are sufficiently large and the melting line located at a low altitude.

During static unstable environmental conditions the enhancement of orographic precipitation by moist convection is possible. Embedded convection is a mechanism for enhancing precipitation amount, intensity and efficiency (Kirshbaum and Durran 2004; Fuhrer and Schär 2005; Roe 2005). Moist convection over orography can be organized in a cellular pattern or in banded structures (see Fig. 1.1d,e). The latter result in strong statial variability in the accumulated precipitation field. Fuhrer and Schär (2005) showed that the generation of precipitation from cellular convective updrafts increases with increasing upstream potential instability. Also the spatial extent of the unstable stratification influences the formation of cellular convection over a mountain (Kirshbaum and Durran 2004; Fuhrer and Schär 2005). Cosma et al. (2002) indicated the necessity of small-scale topographic mountains for the formation of stationary banded convection in lee-side convergence zones. In a more recent study, Kirshbaum and Durran (2005b) simulated banded convective structures during three different shallow convective events over the Coastal Range in western Oregon. They demonstrated that the presence of roll-like convection is primarily determined by the strength of the vertical wind shear in the unstable cap cloud, but showed that small-scale topographic "noise" enhances the organized banded structure and intensity of convection. However, the formation of embedded cellular convection in unstable stratified air upstream of the mountain range can inhibit the generation of banded stationary structures. Further, three-dimensional sensitivity simulations of banded convection over an idealized Coastal Range revealed that, in contrast to an initiation of convection by random "noise" in the background temperature field, small-scale topographic features result in more intensive quasi-stationary rain bands (Kirshbaum and Durran 2005a). Additionally, they concluded that vertical wind shear and other atmospheric factors are less

important for the triggering of banded convection than the formation of lee waves over small-scale hills at the foothill of the windward slope. Consistent with these findings is another recent study by Fuhrer and Schär (2007) which identified the dominating role of indirect triggering of banded convection by gravity wave activity over topographic variations.

With fast improvements in computer technologies, more expensive numerical weather forecasts with finer mesh sizes have been conducted during recent years. Numerical studies have shown that the quantitative precipitation forecast over complex terrain benefits from this increase in horizontal grid resolutions (Colle and Mass 2000). However, Colle and Mass (2000) identified a large sensitivity of the predicted precipitation field to the parameterization of microphysics and concluded that the model skill does not necessarily improve with the degree of complexity of a microphysics scheme. In another study Colle et al. (2000) further investigated the resolution dependence of quantitative precipitation forecasts. Their results revealed an increase of model skill during heavy precipitation, when the grid point distance was decreased to 4 km. In a more recent study of the August 2005 Alpine flood Zängl (2007c) found a significant improvement of the model skill for precipitation over complex Alpine terrain when the horizontal resolution is further reduced to 1 km, because of the model's capability to resolve small-scale topographic variations at this resolution. Furthermore, the author pinpoints a continuous amplification of the sensitivity to the microphysics parameterization, when the model resolution increases.

Aiming at a better quantitative precipitation forecast, both observational and numerical studies of the microphysical growth mechanisms in clouds were conducted in the framework of the two IMRPOVE experiments over the coastal region of Washington state. Evans et al. (2005) presented ice crystal habit measurements by particle imagery during the passage of a cold front and determined the relevant crystal growth processes. Another cold-frontal rainband and its interaction with orographic precipitation is described in Woods et al. (2005), who utilized a large data set of both in-situ and remote sensing measurements. The author detected the importance of the seeder-feeder mechanism (see Fig. 1.1c) for enhancing the precipitation over the orography during this event. Garvert et al. (2005) verified airborne measurements with numerical simulations using the fifth-generation Pennsylvania State University-National Center for Atmospheric Research Mesoscale Model (MM5) and the Reisner-2 microphysics scheme (Reisner et al. 1998). Their results reveal an overprediction of the snow mass due to an inappropriate snow size distribution. As a consequence of the enhanced spill-over of snow crystals, the predicted precipitation field was characterized by an overprediction of precipitation

over the lee side of the mountain range. Using the same numerical setup, Colle et al. (2005) specifically investigated each involved microphysical budget term during this orographic precipitation event and confirmed the overestimated snow mass production. Sensitivity experiments with modified snow size distributions demonstrated a large impact on the surface precipitation. Later Woods et al. (2007) showed that the parameterization of snow habits, which are related to the mass and terminal velocity of snow crystals, influences the spatial precipitation distribution over mountainous regions, but has no significant effect on stratiform precipitation over flat terrain. Thompson et al. (2004) conducted several microphysics sensitivity experiments over a two-dimensional bell shaped mountain range to test new microphysical relations. In a second paper Thompson et al. (2008) introduced several modifications to the Reisner-2 microphysics scheme, which are now implemented in the Weather Research and Forecasting (WRF) modeling system. Other microphysics schemes available in the WRF mesoscale model, namely the Lin (Chen and Sun 2002) and WSM6* (Hong and Lim 2006) schemes, were compared against each other in Hong et al. (2008), who demonstrated the influence of varied graupel sedimentation velocities on the formation and timing of a convective storm.

Besides the uncertainty induced by the treatment of microphysics, quantitative precipitation forecast with cloud-resolving models is restricted by low predictability during the presence of moist convection. Hohenegger et al. (2006) conducted ensemble simulations of three MAP cases, that are influenced by moist convection to a varying degree. The authors showed that the predictability strongly depends on the propagation of perturbations by gravity waves, which are excited in regions of moist convection. Hohenegger et al. (2008) showed that numerical ensemble simulations with explicitly resolved clouds yielded more realistic precipitation fields for the August 2005 Alpine flood. Furthermore, their simulations produced ensemble spreads, that were sensitive to the movement of the associated cyclone and the strength and location of the involved low-level jet. It was found that the variability among their simulations relates to both moist convection and the influence of the low-level jet. Trentmann et al. (2008) assessed the variability of quantitative precipitation forecast during moist convection by a multi-model approach of cloud-resolving simulations. Their results show that the location, timing, and intensity of convective precipitation over low-mountain terrain is significantly influenced by the model setup, and the initial and lateral boundary conditions. These side effects of high-resolution precipitation modeling were also discussed in Zängl (2004), who conducted numerical sensitivity simulations of an orographic precipitation event during MAP. The comparison with surface observations revealed that the predicted pre-

cipitation field is sensitive to both model numerics and physical parameterizations other than microphysics.

1.3 Goals and outline of the thesis

Investigations of a heavy precipitation event, that occured in the Alps in August 2005, are carried out in this thesis. The mesoscale numerical model WRF is utilized to perform cloud-resolving simulations of the flooding event using four different microphysics schemes, namely WSM6*, WSM5* (Hong and Lim 2006), Thompson (Thompson et al. 2008), and Kessler (Kessler 1969), in the finest of four model domains. The numerical experiments are analyzed and validated against a large set of observational rain gauge measurements and data from a weather radar network. For a better understanding of the deficiencies and skilfulness of the simulations, statistical skill scores are calculated based on the comparison to the observational data. The thesis tries to answer the following scientific questions:

• What are the most important mechanisms of orographic precipitation during this event and how do they influence the amount and spatial distribution of precipitation?

• How sensitive are numerical simulations to microphysics parameterizations for distinctive precipitation mechanisms over complex Alpine terrain?

The remainder of this thesis is organized as follows. Both the numerical setup and the observational precipitation measurements are described in chapter 2. A theoretical background on frequently used parameters is given in chapter 3 together with a short description of microphysical processes and their parameterization in bulk microphysics schemes. The synoptic situation and a detailed analysis of the available rain gauge and radar measurements is presented in chapter 4. Numerical results of the WRF reference run and the simulations with modified microphysics are described in chapter 5 and 6, respectively. The thesis closes with a short summary and conclusions in chapter 7.

Chapter 2

Numerical model and observational data

The Weather Research and Forecasting modeling (WRF), which has been developed at the National Center for Atmospheric Research (NCAR), is used for numerical simulations of the August 2005 Alpine flooding event. A continuos development and a large research community ensure the up-to-dateness of this mesoscale forecast model. In this study a sequence of numerical simulations with two-way and one-way nested model domains are conducted. Specifications of the numerical model and the domain setup are described in section 2.1. In section 2.2 the available observational data, which consists of several rain gauge networks and radar measurements is presented and their processing depicted.

2.1 Description of the numerical model

The Advanced Research WRF (ARW) dynamical core, Version 2.2 applies a time-splitting integration using a 3rd-order Runge-Kutta scheme to solve the non-hydrostatic Euler equations in flux form (Skamarock et al. 2005). The time-split integration scheme (Skamarock and Klemp 1992) allows for a smaller time step in a separate integration of fast propagating acoustic waves. The variables are spatially discretized on a staggered Arakawa-C grid and a 5th-order accurate upstream discretization scheme is applied for their advection. As suggested by Zängl (2004), the explicit horizontal diffusion is calculated in physical space. Thereby the eddy viscosities are computed by a Smagorinsky first-order closure. At the upper domain boundary a modified 6-km deep diffusive gravity-wave absorbing condition, as described in Zängl (2007a), is used. The modifications to the standard implementation of the damping layer result in stronger damping of long horizontal wavelengths. In

the vertical WRF uses terrain-following σ levels, that are defined as

$$\sigma = \frac{p - p_{top}}{p_{sfc} - p_{top}} \ , \tag{2.1}$$

whereby p is the hydrostatic pressure at a level, and p_{sfc} and p_{top} are the pressure at the surface and model top, respectively. In the vertical 39 unevenly-spaced σ levels are applied, which corresponds to 38 half-σ levels. The lowermost half-σ level is located at $\sigma = 0.999$, which corresponds to about 7 m above ground. The vertical resolution decreases monotonically with height to $\Delta z \simeq 900$ m at the model top (100 hPa). Note that all numerical simulations in this study are performed with an adaptive hybrid vertical coordinate system (Zängl 2007a), in which the terrain-following σ coordinate levels are gradually transformed with increasing height. Thereby small-scale topographic structures decay with height and reduce the numerical error that arised from the calculation of the horizontal advection on sloping coordinate surfaces (Zängl 2007a).

Figure 2.1a shows the setup of model domains used in the numerical simulations. Up to three two-way nested model domains are used with a horizontal mesh size of 27 km, 9 km, and 3 km, respectively. Firstly, two-way nested model simulations are conducted with three domains, in order to provide the lateral boundary conditions for several subsequent one-way nested simulations on a finer model domain 4 with 1 km horizontal grid point distance (see Fig. 2.1). The applied method with consecutive simulations allows one to vary between different microphysics parameterizations on the innermost model domain 4, while on the outer domains the microphysics parameterization is kept constant. All one-way nested simulations are initialized identically and use the same initial and lateral boundary conditions. The latter are generated every ten minutes, in order to provide a dynamic inflow without large perturbations that arise from the linear interpolation between two time steps. Only water vapor, but not hydrometeor mixing ratios, are passed to the finer model domain 4 by the lateral conditions. Hence, the formation of precipitation needs some spin-up time ("cold start"). The size of the 1-km domain has been chosen large enough to allow for an upstream formation of precipitation and to permit the development of convective precipitation structures before the air mass gets modified by the orography. The domain is made up by 280×211 grid points in the horizontal directions. Its topography is shown in Fig. 2.1b. Unfortunately, the chosen method with two separate runs does not allow for terrain blending at the outer columns/rows of the 1-km model domain. Such a blending is used in two-way nested runs, to ensure a smooth transition between the topography of the coarse and fine nested model domains. The 1-km model domain covers large

parts of Switzerland, western Austria, and the German Alpine foreland.

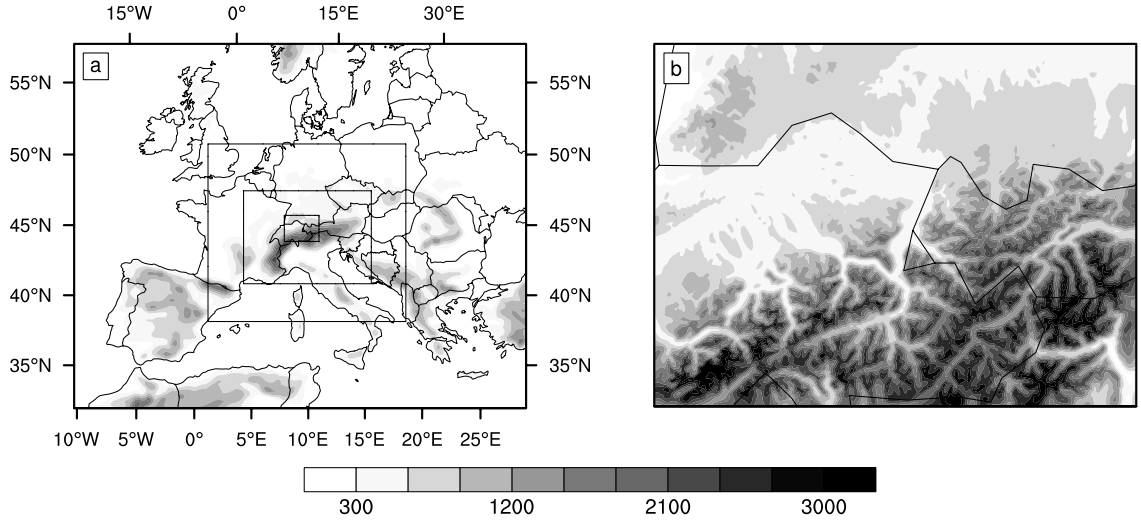

Figure 2.1: The topography of (a) the coarsest model domain and (b) of domain 4. The positions of domains 2-4 are indicated in (a). Topography is shaded every 300 meters.

Both initial and boundary conditions for the two-way nested simulations are produced by the WRF preprocessing system (WPS). The WPS performs the horizontal and vertical interpolation from the analysis of a global model to a specified physical grid. The initial and boundary conditions for the two-way nested runs are obtained from ECMWF (European Centre for Medium Range Weather Forecasts) analysis data on pressure-levels[1]. The operational analysis data is provided on 16 pressure levels on a $0.25° \times 0.25°$ latitude-longitude grid. Two separate two-way nested reference runs are conducted that cover a period of 36 hours each and are initialized at 0000 UTC 21 August 2005 and 0000 UTC 22 August 2005, respectively. Preliminary 72-hours simulations initialized at 0000 UTC 21 August 2005 showed a splitting of the heavy moisture flux upstream of the most affected Alpine area after 48 hours, which led to significant errors in the precipitation field. For both simulations the starting times are chosen such as to allow for a spin-up time of six hours before 0600 UTC, when the observation intervall of the routinely daily accumulated precipitation, which will be used for validation purposes, starts.

In domains 1-2 sub-grid scale cumulus precipitation is parameterized by the new Kain-Fritsch mass-flux scheme, which is described by Kain and Fritsch (1990, 1993).

[1]The comparison of the WPS results with the ECMWF model-level analysis data revealed a systematic dry bias (~ 1.2 g kg^{-1}) of the water vapor mixing ratio at lower levels. The error was fixed at a very late stage of this thesis.

Tests showed an improvement of precipitation structures and a better agreement with observed precipitation fields in domain 3, when no cumulus parameterization was applied. In domain 4, convective precipitation is assumed to be explicitly resolved. The longwave part of the radiation is calculated with the Rapid Radiative Transfer Model (RRTM; Mlawer et al. 1997). A modified Dudhia (1989) short-wave scheme is used that comprises the shading effects of mountains. The surface layer scheme is described by similarity theory. It provides the friction velocity and exchange coefficients for the land-surface and planetary boundary layer (PBL) scheme. A 5-layer thermal diffusion land-surface model calculates the heat and moisture fluxes at the surface. The PBL parameterization is accomplished with the Yonsei University (YSU) scheme, a non-local first-order scheme that uses a prescribed profile to determine the vertical diffusion coefficients. In domains 1-3 microphysics are described by the so-called WRF single-moment bulk microphysics scheme WSM6*, which is presented in section 3.4.2. Several one-way nested sensitivity simulations are conducted in domain 4, in which the microphysics are parameterized by the WSM6*, the WRF single-moment bulk microphysics scheme WSM5* (no graupel), the Kessler scheme, and the Thompson scheme, respectively. Consult sections 3.4.1 to 3.4.3 for a description of each of these schemes. Table 2.1 summarizes the attributes of all performed numerical simulations and introduces abbreviations, which will be used in the following.

Name	Domains	BC	Nesting	Microphysics
WSM6*_2_4	1-4	ECMWF	2	WSM6*
WSM6*_2	1-3	ECMWF	2	WSM6*
REF	4	WSM6*_2	1	WSM6*
WSM5*	4	WSM6*_2	1	WSM5*
THOM	4	WSM6*_2	1	Thompson ($\mu = 0$ for graupel)
THOM_GD	4	WSM6*_2	1	Thompson ($\mu = 1$ for graupel)
THOM2	4	WSM6*_2	1	Thompson (modified graupel production)
KES	4	WSM6*_2	1	Kessler
MAR	4	WSM6*_2	1	WSM6* (smaller N_c)

Table 2.1: Overview of all conducted numerical simulations, their boundary conditions (BC), and nesting method (one-way or two-way). The topography in the coarsest and finest domain is shown in Fig. 2.1. Note that each simulation has been conducted for two different initialization times at 0000 UTC 21 August 2005 and 0000 UTC 22 August 2005.

2.2 Observational data

2.2.1 Rain gauge measurements

For validation purposes, data from several institutes are compared against the numerical simulations. The applied data sets are provided by the Central Institute for Meteorology and Geodynamics (ZAMG), the German weather service (DWD), the Swiss weather service MeteoSwiss, and the Austrian hydrological service (HZB). The DWD measurements cover the German states of Bavaria and Baden-Wurttemberg, which form the southern part of Germany. For Bavaria, both hourly rain measurements from 119 automatic stations and daily manual observations (KLIMA) at 430 stations are used. For all of the 119 automatic rain stations also KLIMA observations are available. The daily accumulated sums from the automatic stations proved to be identical to the KLIMA observations, as both measurements get routinely adjusted. For the Baden-Wurrtemberg region, only the 24-hours accumulated precipitation KLIMA data from 218 station measurements are available.

The ZAMG data consists of highly temporally resolved automatic measurements (TAWES) and KLIMA station observations. Again here at each of the 158 automatic rain stations a KLIMA measurement of daily accumulated precipitation is provided. However, in contrast to the DWD data, differences between the accumulated sums of the automatic and the KLIMA measurements exist, as measurements have not been adjusted by the ZAMG. At six of the 265 KLIMA stations, measurements from two rain gauges are available. To avoid overrating the model biases arising at their locations, these measurements are averaged. The distances between the rain gauges at these locations are much smaller than the horizontal grid spacing of the 1-km and 3-km grids in domain three and domain four, respectively. Thus their spatial

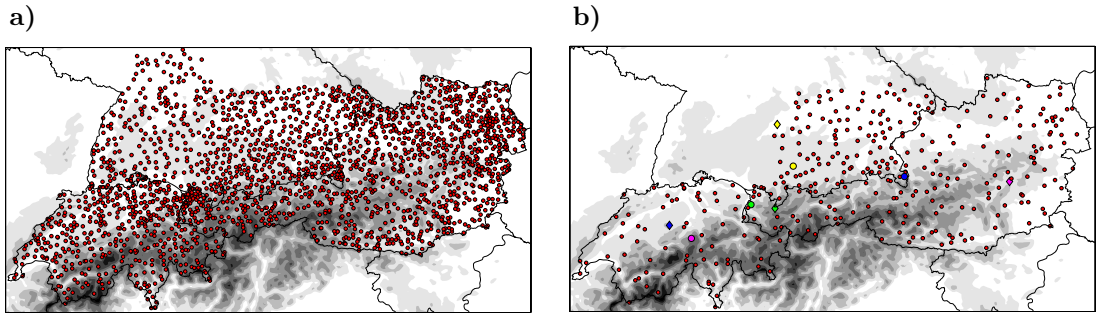

Figure 2.2: The locations of available stations in the Alpine catchment are shown for (a) manual, daily measurements and (b) highly temporally resolved automatic measurements. In (b) the positions of the stations in Günzburg, Napf, Warth, and Bruck/Mur are indicated by the yellow, magenta, green, and blue diamonds, respectively. The positions of the stations in Kaufbeuren, Engelberg, Fraxern, and Berchtesgaden are indicated by the yellow, magenta, green, and blue bullets, respectively.

differences in precipitation distribution are not resolved by the model and the averaging of the station measurements becomes even more meaningfull. Seventy of the MeteoSwiss rain stations belong to a net of automatic stations (ANETZ), covering Switzerland very well. Hereby, a ten minute temporal resolution is available. At the remaining 425 Swiss NIME stations manual daily measurements are conducted. The HZB provides daily precipitation sums at 783 stations in Austria.

As a result of different data providers and regional discrepancies of the station density, the dense measurement net of KLIMA and HZB observations is used for the validation of daily accumulated precipitation, whereas for shorter validation periods only the less dense net of automatic stations is used in Austria. The simulated precipitation over Baden-Wurttemberg can not be validated for periods shorter than 24 hours. The Swiss ANETZ and NIME measurements are used for validations of daily sums and for shorter periods only the ANETZ measurements can be used. Figure 2.2 shows the positions of both the manual and automatic rain gauge measurements in the Alpine catchment area.

For the calculation of the accumulated precipitation during a given time period, the available rain measurements are extrapolated in time, if at least 80 % of the possible measurements during this period are available and valid. If a data lack during a period is larger than 20 %, the accumulated precipitation at the station is not computed for this period. The extrapolation of available rain measurements at a station works as following:

$$\text{Accumulated precipitation} \quad = \quad \frac{\text{Accumulated available precipitation}}{n_a} \times n_p$$

Here n_a is the number of available measurements during the period and n_p the total number of measurements at the station, that could be possibly available during the period.

2.2.2 Radar measurements

The Central European Weather Radar Network (CERAD) provides radar composites from operational radars in Austria, Germany, Switzerland, Hungary, Croatia, Slovenia, Poland and the Czech Republic. The horizontal resolution of one image pixel is 2 km. A detailed description of the CERAD product is given in Randeu et al. (1996). The data, provided by ZAMG, consists of half-hourly rain rates, which are subdivided into eight classes[2].

For the comparison to the numerical simulations, accumulated precipitation is calculated by summing up all the half-hourly rain rates within a certain period.

[2] $[0. - 0.2], [0.2 - 0.8], [0.8 - 3.], [3. - 8.], [8. - 22.], [22. - 75.], [75. - 100.], [> 100.]$ mm h^{-1}

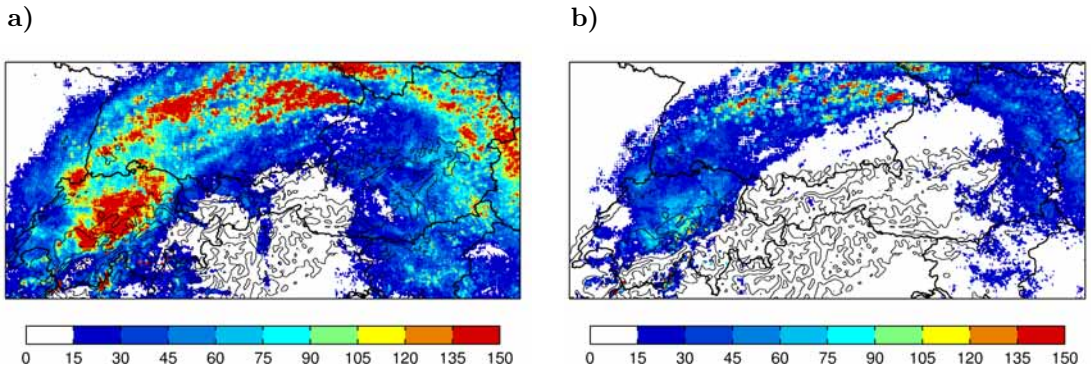

Figure 2.3: Accumulated precipitation between 0600 UTC 21 Aug and 0600 UTC 22 Aug 2005, as calculated from (a) the upper limit and (b) the lower limit of each radar rain rate class.

But, because of the categorization of the rain rates into discrete classes, multiple integration methods can be applied. The calculation of accumulated precipitation can practically be achieved by the summation of the mean values, the upper limits, or the lower limits of each class. However, the results show a tremendous variability. The precipitation amounts strongly depend on the chosen method, as the difference between lower and upper limit of a class is very large, e.g. 25 mm for the seventh class. Figure 2.3 shows the large spread between accumulated precipitation fields derived by summing up the lower and the upper class limit, respectively.

In order to assess the most realistic quantitative precipitation distribution from the CERAD product, the radar data is compared to several rain gauge stations in the Alpine catchment. Figure 2.4 demonstrates the evolution of accumulated precipitation at four stations. Additionally, the radar-derived precipitation measurements at the same locations are shown. Note that the dashed lines account for the upper and lower limits of the above mentioned integration techniques, while the gray solid line represents the computation based on the mid-values of the class intervals. Figure 2.4a shows the accumulated precipitation at Günzburg, which belongs to the Bavarian Alpine foreland. Here the lower limit of the radar spread is in good agreement with both the temporal evolution and the relatively low intensity of precipitation. At Napf in central Switzerland the calculation by the mean values of the radar classes achieves the best agreement with the evolution of the observed surface precipitation (see Fig. 2.4b). However, the integration of the top of each rain rate class still underestimates the observed surface rainfall at Warth/Vorarlberg (see Fig. 2.4c). At Bruck, which is located at the southeastern rim of the Alpine barrier, again, the calculation by the mean value of each rain rate class results in a close agreement with the rain gauge measurement. Note that the radar overestimates the observed precipitation at several stations in the Alpine foreland, but underestimates precipitation at locations with heavy rainfall in the center of the Alps. In the

remainder of this study, specifically in section 4.3, the calculation of accumulated precipitation is based on the class mean values. The class mean values seem to produce a fairly good overall agreement with rain gauge measurements.

Besides the above mentioned difficulties in data processing, additional problems arise from the precipitation intensity measurements by the operational radar technology. Processes that affect the backscattered signal are, e.g., ground cluttering, partial or total beam blockage in complex orographic areas, and the radar calibration. The determination of an appropriate reflectivity-rain rate relation is hindered in regions with rimed ice-crystals and below clouds, where rain starts to evaporate.

As a consequence of both the attributes of operational radar measurements and the above shown sensitivity of precipitation calculation caused by discrete rain classes, the precipitation fields derived from the CERAD radar composites will not

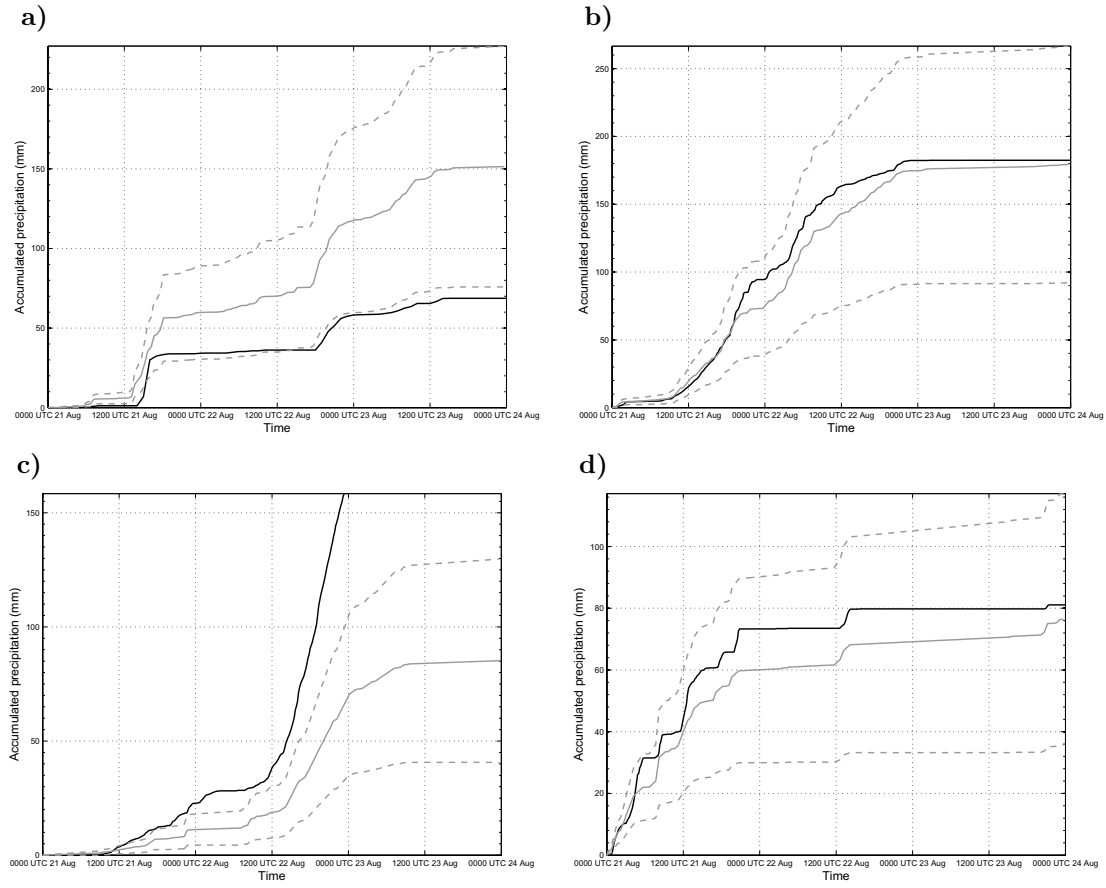

Figure 2.4: Temporal evolution of accumulated precipitation at (a) Günzburg in Bavaria, (b) Napf in central Switzerland, (c) Warth in western Austria, and (d) Bruck a.d. Mur in southeastern Austria. The CERAD radar measurements are drawn in gray. Gray dashed lines indicate the possible spread of the calculation of accumulated precipitation and the gray solid line shows the computation based on the mid-values of the class intervals. Precipitation from automatic rain gauge measurements are shown by the black lines. The locations of the stations (a),(b),(c), and (d) are indicated by the yellow, magenta, green, and blue diamonds in Fig.2.2b, respectively.

be discussed in a quantitative manner in the remainder of this thesis. However, the structure and spatial distribution of precipitation estimated by the radar still adds valuable information about the prevailing mechanisms of precipitation formation. In section 4.3 precipitation patterns and affected areas will be determined and due to half-hourly measurements also the evolution of certain precipitation patterns will be analyzed.

Chapter 3

Theoretical Background

Mechanisms of orographic precipitation strongly depend on the mesoscale interaction of the flow with the mountain. Theoretical studies of mesoscale flow past topography provide the dynamical background for this study. Analytical solutions of the linearized momentum equations for such flows were discussed in Queney (1948) and Smith (1979). Schär (2002) reviewed the fundamental parameters that determine the dynamical regime of dry flow. These are shown in section 3.1. Also the calculation of the equivalent potential temperature, a conserved parameter in saturated air flows, is described there. Indices for moist instability are summarized in section 3.2. To investigate the influence of microphysics on precipitation, the complexity and possible interactions between different hydrometeors need to be understood. The formation of precipitation can be assigned to warm phase, mixed phase, or pure ice phase processes. The most fundamental processes are briefly described in section 3.3. Theoretical formulations of some of the processes, characteristic assumptions, and parameterizations within microphysics schemes are explained in section 3.4.

3.1 Dimensionless mountain height vs. equivalent potential temperature

Linear and highly non-linear flow regimes are possible for a fluid passing a topographic obstacle. Schär (2002) presents a regime diagram for the possible flow patterns of a stratified rotational fluid over an obstacle. The dynamics are determined by two non-dimensional parameters, the Rossby number R_0 and the dry dimensionless mountain height H_d:

$$R_0 = U/(Lf) \tag{3.1}$$

$$H_d = N_d h_m/U \ , \tag{3.2}$$

whereby U is a uniform upstream velocity, L a characteristic mountain half-width, f the Coriolis parameter, and h_m the mountain height. The atmospheric stability is characterized by the dry Brunt-Väisälä frequency N_d.

For dry flow over the Alps ($R_0 \sim 1$) the differentiation between a flow-over and a flow-around regime depends on the atmospheric conditions, which are incorporated in the dry dimensionless mountain height H_d. The application of this number is only reasonable for dynamical processes without phase changes like condensation or evaporization. To include the effects of latent heating and cooling, only its moist counterpart H_m, based on the moist Brunt-Väisälä frequency N_m, is meaningful. While for the dry case a transition from the flow-over to the flow-around regime occurs at $H_d \simeq 1$, the determination of a critical moist H_m is precarious. The decrease of effective stability due to the release of latent heat and the vertical variation of static stability due to vertical moisture gradients lead to an uncertain critical value for saturated flows (Colle 2004). Additionally, the mountain height h_m is often not clearly assignable, as the small-scale topography varies strongly in Alpine regions. Given these restrictions, dimensionless mountain heights are avoided in this work. Instead, the equivalent potential temperature θ_e is used to identify dynamical flow regimes of saturated air over mountains. Following Bolton (1980) θ_e can be expressed by the following set of equations:

$$\theta_e = \theta \times \exp\left[\left(\frac{3.376}{T_L} - 0.00254\right) \times r(1 + 0.81 \times 10^{-3} r)\right] \tag{3.3}$$

$$\theta = T \times \left(\frac{p_{00}}{p}\right)^{0.2854} \tag{3.4}$$

$$T_L = \frac{2840 \text{ K}}{3.5\ln(T) - \ln(e) - 4.805} + 55 \text{ K} \quad . \tag{3.5}$$

Here θ is the potential temperature in K, T_L the dry air temperature at the lifting condensation level in K, T the dry air temperature in K, r the water vapor mixing ratio in g kg^{-1}, $p_{00} = 1000$ hPa, p the pressure in hPa, $e = \frac{pr}{\epsilon + r}$ the water vapor pressure in hPa, and $\epsilon = \frac{R}{R_v} = 0.622$ is the ratio of the gas constants of dry air and water vapor. As θ_e is conserved for saturated adiabatic flows, it is a helpful quantity for classifying moist dynamical flow regimes in mountain meteorology.

3.2 Indicators for moist instability

Indices for the static stability of a saturated air flow are necessary for the discussion of moist convection. The upstream potential instability, as indicated by a negative sign of $\frac{\partial \theta_e}{\partial z}$, is generally seen as a necessity for cumuliform orographic cloud types. However, numerical experiments in Kirshbaum and Durran (2004) show that a better

predictor for embedded convection is the moist Brunt-Väisälä frequency N_m. In this work, the moist Brunt-Väisälä frequency N_m is defined after Durran and Klemp (1982) as

$$N_m^2 = g\left[\frac{1+(L_v r_s/RT)}{1+(\epsilon L_v^2 r_s/c_{pd}RT^2)} \times \left(\frac{d\ln\theta}{dz} + \frac{L_v}{c_{pd}T}\frac{dr_s}{dz}\right) - \frac{dr_w}{dz}\right] , \tag{3.6}$$

where $g = 9.81$ m s^{-2} is the gravitational acceleration, $L_v = 2.501 \times 10^6$ J kg^{-1} the latent heat of vaporization, r_s the water vapor mixing ratio at saturation in g g^{-1}, $R = 287$ J kg^{-1}K^{-1} the ideal gas constant of dry air, and r_w the total water mixing ratio in g g^{-1}. It is found, that statically stable saturated layers exist although $\frac{\partial\theta_e}{\partial z} < 0$, but ${N_m}^2 > 0$. Fuhrer and Schär (2005) verified these results and detected the necessity of regions with ${N_m}^2 < 0$ for the formation of embedded convection. By applying a linear analysis, they additionally showed that the growth rate of embedded convection strongly depends on the depth of the unstable layer. They start with a linearized set of Boussinesq approximated equations and consider a wave ansatz for the vertical velocity $w = Ce^{i(kx+ly+mz-\omega t)}$ in order to gain a dispersion relation for the complex frequency

$$\omega = \pm\left(\frac{k^2+l^2}{k^2+l^2+m^2}N_m^2\right)^{0.5} + kU , \tag{3.7}$$

where k, m, and l are the wave numbers in x, y, and z direction, respectively, in a Cartesian coordinate system, and U is the mean velocity in x direction. Perturbations of the vertical velocity grow exponentially, when ω exhibits an imaginary part, which is only the case for $N_m^2 < 0$.

3.3 Microphysical processes

Following Pruppacher and Klett (1980) microphysical warm phase, mixed phase, and ice phase processes are briefly described in this section:

Homogeneous nucleation of water:
If only water is present, spontaneous phase changes can result from temperature and density fluctuations in the water vapor phase. Water vapor condenses to liquid water as soon as the vapor pressure equals or exceeds the saturation vapor pressure. If so, small molecular clusters of liquid water, which are permanently formed in subsaturated conditions, reach critical sizes and can even further grow (Pruppacher and Klett 1980). Due to the fact that the saturation vapor pressure over a curved water surface is higher than over a plane surface and also increases with smaller droplet sizes, an initially built small water droplet

requires very high supersaturation ($\sim$ 300 − 400%) to survive. Such high values of supersaturation are not observed in natural clouds, which leads to the assumption that homogeneous nucleation plays no role in the cloud water formation.

Heterogeneous nucleation of water:
If water-soluble, hygroscopic or water-insoluble, but partially wettable aerosol particles are present in moist air, which is almost always the case in the lower and middle troposphere, heterogeneous nucleation of water is possible. Aerosol particles can act as cloud condensation nuclei (CCN) even at the observed low values of supersaturation ($< 1\%$). CCN allow for the activation of drop formation by a collection of water molecules, as the saturation water pressure with respect to a solution containing dissolved CCN is smaller than that with respect to pure water. The CCN concentration depends on the origin of the air mass (e.g., maritime, continental), meteorological conditions, the absolute height above sea level, and the presence of pollution sources.

Ice nucleation:
Homogeneous ice nucleation, which means spontaneous freezing of liquid water, normally occurs at temperatures below −40°C. Thereby no secondary material is needed. However, water-insoluble and sufficiently large aerosol particles can serve as ice nuclei (IN) and enable heterogeneous formation of ice crystals at temperatures warmer than −40°C. Typically, such particles are solid silicate particles like clay. The chemical composition of an aerosol particle determines its nucleability, its preferred mode of crystal activation, and its temperature range of activity (Pruppacher and Klett 1980). Three ways for heterogeneous ice crystal activation exist (Pruppacher and Klett 1980). Firstly, ice crystals can result from deposition of water vapor onto the IN and a subsequently transformation of the vapor into ice. Secondly, IN freeze on contact with supercooled drops or, finally, immerse into a supercooled droplet and initiate freezing from inside. The IN concentration decreases nearly exponentially with temperature. Again, the shape and weight of the crystals depends on their temperature, influencing the fall speed and radiative properties.

Diffusion growth of water drops and ice-crystals:
If a cloud droplet is situated in a supersaturated environment, condensation of water vapor onto the drop reduces the relative humidity in its close proximity. The established humidity gradient from close to the surface of a droplet to its surrounding air leads to a water vapor flux onto this water particle, which subsequently gains in mass and size. Thereby the supersaturation of the surrounding air is removed

by condensation and deposition of water vapor. Afterwards, typical droplet sizes range from approximately 0.1 μm to 10 μm, which are smaller than the observed rain drop sizes.
The same process accounts for ice crystals, with the difference that the diffusional growth rate depends on both temperature and supersaturation. As a consequence, a large variety of different crystal habits occur.

Collision and coalescence:
While initially small droplets are generated by diffusional growth, precipitation-sized droplets are primarily produced due to collision and coalescence. This process is usually known as a "warm-rain" mechanism of precipitation formation, although it is also observed with supercooled droplets. Hydrodynamic interactions between droplets result from different particle radii, their corresponding terminal velocities, and wake regions above falling particles. The collision efficiency between droplets at a given height is primarily determined by the ratio of their radii, but also influenced by turbulence, droplet charges and external electrical fields (Pruppacher and Klett 1980). A "sink" for coalescence is the rebound of deformable larger droplets and the break-up of droplets due to high rotational kinetic energy of the unified droplet pair. Bimodal particle size distributions result from coalescence, as larger particles grow at the expense of smaller ones.
In contrast to drop-drop collisions, the efficiency of ice crystals collecting drops, which is accretion or riming, is limited by both an upper and lower critical drop size and by a minimum ice crystal size. The shape of the ice crystal determines the lower critical size for the onset of riming. A large variety of rimed particles exist. These are differentiated by their stage of riming, which determines their size, density, and shape. Rimed particles are, e.g., graupel, snow pellets, and hail.
Field experiments show that the aggregation of colliding ice-crystals strongly depends on the air temperature. A maximum of aggregation occurs at 0°C, because the surfaces of ice-crystals become sticky, and at approximately -15°C due to the entangling of dendrite shaped particles. Such agglomerations of ice crystals are called snow crystals or aggregates.

Wegener-Bergeron-Findeisen process (WBF):
Besides diffusion growth of ice crystals, the WBF leads to additional growth of ice crystals, if supercooled water droplets are present. This process, which is known as the "cold-cloud" formation of precipitation-sized particles, results from the difference between the saturation vapor pressure over water and ice at temperatures below 0°C. The air is always slightly more supersaturated with respect to ice than with respect to liquid water, due to the lower saturation vapor pressure over ice. If the air is in a

subsaturated condition with respect to liquid water, the water droplets evaporate, whereas the air might still be supersaturated with respect to ice. This causes the growth of ice crystals by vapor diffusion at the expense of the liquid droplets. This process ends when all ice crystals reach sufficiently large size to precipitate or when all liquid water is consumed.

3.4 Parameterization of microphysics

3.4.1 Kessler

Kessler (1969) formulated a very simple scheme to describe basic physical processes involved in the formation of precipitation. The scheme treats only warm cloud physics, which means that no ice or mixed phase interactions are considered. This represents a substantial limitation to its practical applicability and microphysical completeness. Only water vapor, cloud water, and rain drops exist and the interaction between these three species is solely described by four processes.
Firstly, the conversion rate of cloud water q_c to precipitation particles q_r by collision and coalescence is described by the so called autoconversion (CC). Additionally, the accretion rate (AC) of small droplets by rain drops is incorporated. Secondly, the sedimentation of rain and the evaporation rate of rain (EP) to water vapor q_v is included. Finally, the scheme comprises the condensation rate of vapor and the evaporation rate of cloud water (G).
Note that in WRF the advection of each hydrometeor array is already accomplished ahead of the microphysics call. The hydrometeor interactions result in tendencies ($g\ g^{-1}\ s^{-1}$) of the mixing ratio of each species q_v, q_c, and q_r, which need to be updated after each time step Δt, according to the following set of equations:

$$q_v = \max(q_v - (\mathrm{G} - \mathrm{EP})\Delta t, 0) \tag{3.8}$$
$$q_c = q_c + (\mathrm{G} - \mathrm{CC} - \mathrm{AC})\Delta t \tag{3.9}$$
$$q_r = q_r - (\mathrm{EP} + \mathrm{CC} + \mathrm{AC})\Delta t \tag{3.10}$$

Equation 3.8 ensures that no negative water vapor mixing ratios are produced by the evaporation of cloud water and rain. Apparently, all budget terms act both as sink and source terms. They are defined as

$$\mathrm{CC} = f_n c_1 \max(q_c - c_2, 0) \tag{3.11}$$
$$\mathrm{G} = \frac{q_v - q_s}{1 + \frac{p}{p-e_s} q_s \frac{f_5}{(T-29.65)^2}} \tag{3.12}$$
$$\mathrm{AC} = q_c(1 - f_n) \tag{3.13}$$
$$\begin{aligned}\mathrm{EP} = \min \Bigg[& \Big[(1.6 + 124.9(0.001\rho q_r)^{0.2046}) \frac{(0.001\rho q_r)^{0.525}}{2.55\ 10^8 (p q_s) + 5.4\ 10^5} \Big] \ldots \\ & \dim(q_s, q_v)/(0.001\rho q_s), \ldots \\ & \max\big[-(\mathrm{G} + q_c), 0. \big], \ldots \\ & q_r \Bigg] .\end{aligned} \tag{3.14}$$

Equation 3.11 reveals a linear relation between CC and q_c, if a certain threshold c_2 of cloud water q_c is reached. Figure 3.1 shows the increase of the autoconversion rate with cloud water content q_c, as soon as the critical value $c_2 = 1$ g kg^{-1} is exceeded. For smaller mixing ratios, CC is zero. The inclination of the function is given by the parameter c_1. Figure 3.1 also demonstrates the increase of rain production with rain mixing ratio q_r. The factor $f_n = (1 + c_3 q_r^{c_4})^{-1}$, which strongly depends on the rain mixing ratio q_r, coordinates the ratio of rain production from CC and AC. For $f_n = 1$, as described above, rain is solely produced by CC. For smaller f_n, the conversion by AC increases, while the conversion by CC decreases. The relation regains its linearity (see equation 3.13) at very high rain mixing ratios ($f_n \to 0$). This effect simply accounts for the enhanced collision efficiency between droplets, when larger and faster falling rain drops are present. Due to this accretion process, the conversion to rain sets in already at very low values of cloud water mixing ratio.

The functionality for condensation and evaporation of cloud water is given by G in equation 3.12. If the supersaturation of moist air, which is the difference between water vapor mixing ratio and saturation mixing ratio $q_v - q_s$, is positive, condensation of water vapor reduces the relative humidity and increases the cloud water mixing ratio. Otherwise, when the air is subsaturated, evaporation increases the vapor mixing ratio at the expense of cloud liquid water. The denominator in 3.12 can

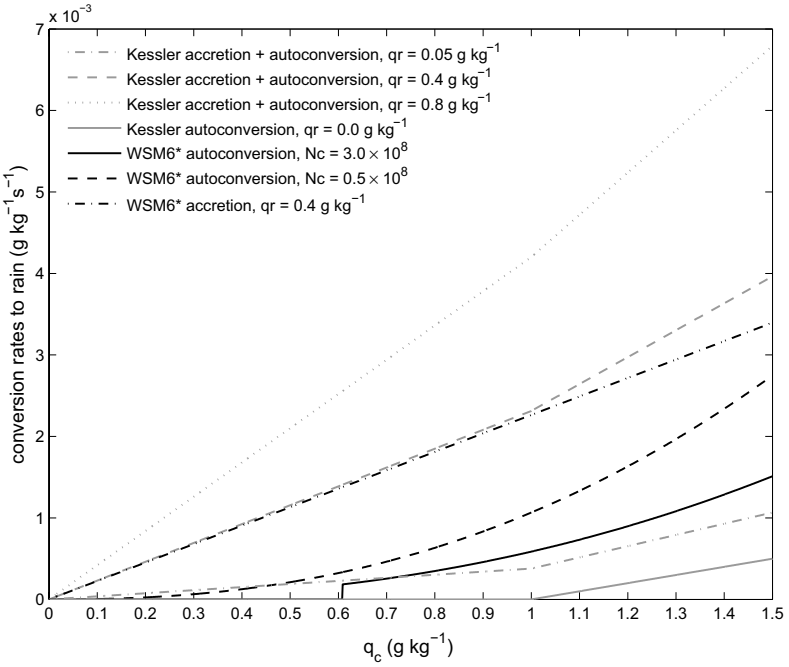

Figure 3.1: Conversion rates (g kg^{-1}s^{-1}) of cloud water q_c to rain from the Kessler and the WSM6* scheme. Conversion rates are calculated for four rain mixing ratios q_r for Kessler and two cloud number concentrations N_c for WSM6* (see legend).

be derived from the Magnus formula and contains the pressure p, saturation vapor pressure e_s, temperature T, and a constant $f_5 = 17.67 \times (273.15 - 29.65)\frac{2.5\times10^6}{1004.6}$.

Several preconditions restrict the evaporation of rain (see Eq. 3.14). The "min" function in Eq. 3.14 is utilized to ensure that the largest possible evaporated water mass is the current mixing ratio of rain. Furthermore, it makes sure that, if the cloud liquid water is not yet completely evaporated by G, the evaporation of rain is zero. The cloud liquid water has to be removed first. If these conditions are met and only in subsaturated conditions, the evaporation of rain is proportional to the saturation deficit $q_s - q_v$.

Finally, the scheme also considers the influence of the release or consumption of latent heat due to condensation or evaporation of cloud water, respectively, and the consumption of latent heat by the evaporation of rain. The potential temperature is updated each time step by

$$\theta = \theta + \frac{L_v}{c_p}\frac{\theta}{T}\Delta m \ . \tag{3.15}$$

Hereby, the right term simply accounts for the temperature modification due to phase changes of mixing ratio Δm, as defined by $\Delta T = \frac{L_v}{c_p}\Delta m$.

3.4.2 WRF single moment bulk microphysics schemes (WSM)

Three WSM schemes are implemented in the WRF model. They differ in the number of prognostic hydrometeor arrays. The WSM3* scheme includes only three categories of hydrometeors, namely vapor, cloud water/ice, and rain/snow. Apparently, one category accounts for condensate and one for precipitation. The categories are treated temperature dependently. Cloud water exists below the melting line, while ice is located only above. The same accounts for the secession of rain and snow. Due to this temperature separation, supercooled cloud water or melting snow can not be considered in this scheme. Because its calculation is very inexpensive, the WSM3* scheme is still used in operational weather forecasts. The WSM5* scheme contains five separate hydrometeor arrays, that are vapor, cloud water, rain, ice, and snow. Thus, it allows for melting processes and accounts for supercooled liquid water.

The WSM6* scheme additionally predicts the mixing ratio for graupel and the intercations of graupel with other species are implemented. Altogether six different hydrometeor species are included. In the following, some basic assumptions and formulations of this sophisticated single-moment bulk microphysics scheme are explained.

Following Lin et al. (1983), exponential size distributions are assumed for the number concentration (m^{-4}) of the hydrometeors rain, snow, and graupel. They are

expressed as

$$\begin{aligned} N_r(D_r) &= N_{0_r} \exp(-\lambda_r D_r) \\ N_s(D_s) &= N_{0_s} \exp(-\lambda_s D_s) \\ N_g(D_g) &= N_{0_g} \exp(-\lambda_g D_g) \ , \end{aligned} \tag{3.16}$$

whereby N_{0_r} and N_{0_g} are constant intercept parameters of the size distribution (m^{-4}). The intercept parameter for snow N_{0_s} decreases with temperature

$$N_{0_s} = 2 \times 10^6 \exp\left[0.12(T_0 - T)\right] \ , \tag{3.17}$$

because observational studies show a broadening of the snow size distribution at higher temperatures (Houze et al. 1979). D_r, D_s, and D_g are the diameter of the rain, snow, and graupel distributions, respectively. The slope parameters λ_r, λ_s, and λ_g can be calculated by

$$\begin{aligned} \lambda_r &= \left(\frac{\pi N_{0_r} \rho_r}{\rho q_r}\right)^{0.25} \\ \lambda_s &= \left(\frac{\pi N_{0_s} \rho_s}{\rho q_s}\right)^{0.25} \\ \lambda_g &= \left(\frac{\pi N_{0_g} \rho_g}{\rho q_g}\right)^{0.25} \ , \end{aligned} \tag{3.18}$$

where ρ is the air density and ρ_r, ρ_s, and ρ_g are constant densities of the hydrometeors rain, snow, and graupel, respectively, and q_r, q_s, and q_g are their mixing ratios. In contrast to other schemes (e.g., Lin et al. 1983), in which the ice number concentration N_i (m^{-3}) is diagnosed from the cloud temperature by applying a temperature dependent relation, here a revised approach of the ice microphysics treatment is used. This approach is described in Hong and Lim (2006). The temperature dependent ice number concentration leads to wrong cloud-radiation feedbacks, especially from anvil and cirrus clouds (Hong and Lim 2006) and is replaced by a diagnostic relation, that incorporates the ice mixing ratio q_i. The relation is expressed as

$$N_i = 5.38 \ 10^7 \times (\rho q_i)^{0.75} \ . \tag{3.19}$$

The coefficients in this expression depend on the shape of the ice crystals, which are here assumed to be bullets.

A time split technique is used for reasons of numerical stability. If the time step is larger than a critical value of 120 seconds, it is first divided by this critical value to obtain a number of small time steps. As in all WRF microphysics schemes, the sedimentation of precipitating hydrometeors will be calculated in a loop over

the small time steps to keep the calculation numerically stable. Following Lin et al. (1983) the mass-weighted terminal velocities of rain, snow, and graupel are expressed by empirical relations

$$\begin{aligned} V_r &= \frac{841.9\Gamma(4+0.8)}{6}\left(\frac{\rho_0}{\rho}\right)^{0.5}\frac{1}{\lambda_r} \\ V_s &= \frac{11.72\Gamma(4+0.41)}{6}\left(\frac{\rho_0}{\rho}\right)^{0.5}\frac{1}{\lambda_s} \\ V_g &= \frac{330\Gamma(4+0.8)}{6}\left(\frac{\rho_0}{\rho}\right)^{0.5}\frac{1}{\lambda_g}\ , \end{aligned} \tag{3.20}$$

whereby $\Gamma(x)$ is the Gamma function $\Gamma(x) = \int_0^\infty t^{x-1}e^{-t}\mathrm{d}t$. The density terms appear in order to include the increase of the terminal velocity with height (i.e. decreasing density). Figure 3.2 shows the linear assumptions for the terminal velocities of the hydrometeor species. Apparently, rain has the highest fall speed and snow the lowest. The sedimentation of ice crystals is implemented by the terminal velocity $V_i = 1.49\ 10^4 D_i^{1.31}$, where the diameter-mass relation of ice crystals is given by $D_i = 11.9 M_i^{0.5}$. Substituting $\left(\frac{\rho q_i}{N_i}\right)$ for M_i and with Eq. 3.19 one yields the velocity-mixing ratio relation

$$V_i = 3.2998(\rho q_i)^{0.1638}\ , \tag{3.21}$$

which is also plotted in Fig. 3.2. Note that a critical ice mixing ratio limits the size of the ice crystals by a corresponding diameter of 500×10^{-6} m. Larger ice-crystals are converted to snow.

A detailed description of all production and loss terms of each species is presented in Hong et al. (2004). Some of them are discussed below and are important for the further understanding of the numerical experiments conducted in the following sections.

Autoconversion (Praut) of cloud water to rain is not calculated by the linear assumption from Kessler (1969), but has now better physical roots (Tripoli and Cotton 1980). The collection of cloud water by rain drops (Pracw) is based on the continuous model of collection growth, in which large particles grow with the same rate (Pruppacher and Klett 1980). These two terms are expressed as

$$\begin{aligned} \mathrm{Praut} &= -\frac{0.104 g E_c \rho^{4/3}}{\mu (N_c \rho_w)^{1/3}} q_c^{7/3} H(q_c - q_{c0}) \\ \mathrm{Pracw} &= \frac{\pi 841.9 E_{rc} N_{0r} q_c}{4}\left(\frac{\rho_0}{\rho}\right)^{0.5}\frac{\Gamma(3+0.8)}{\lambda_r^{3+0.8}}\ . \end{aligned} \tag{3.22}$$

Hereby μ is the dynamic viscosity of air (kg m^{-1} s^{-1}), N_c the droplet number con-

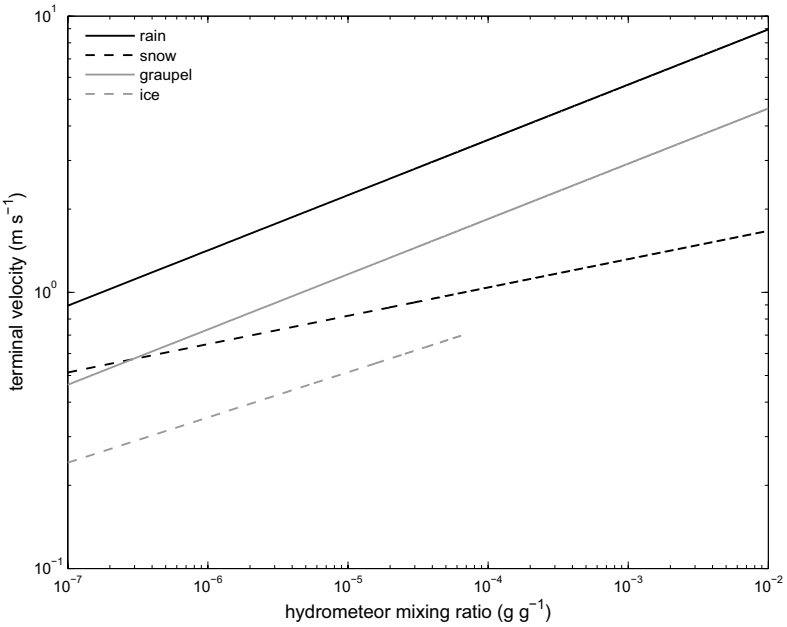

Figure 3.2: Mass-weighted WSM6* particle terminal velocities are plotted against mixing ratios of hydrometeor species. Velocities are calculated at 900 hPa and $T = -5°C$.

centration (m^{-3}), g the gravity acceleration (m s^{-2}), and $E_c = 0.55$ the collection efficiency of cloud droplets. With $H(x)$ the Heaviside step function, the autoconversion is suppressed below a critical cloud water value of q_{c0}, which is defined as $q_{c0} = \frac{4\pi\rho_w r_{cr}^3 N_c}{3\rho}$. The critical mean droplet radius for autoconversion r_{cr} is 3×10^{-6} m. If N_c, the number concentration of cloud droplets, is decreased, the critical cloud water mixing ratio is lowered and rain production from autoconversion increased. This assumption is still adapted from the Kessler type formulation, but allows a better involvement of the cloud drop size. The formulation of the accretion Pracw of cloud droplets includes the collection efficiency $E_{rc} = 1$, the intercept parameter of rain N_{0r}, the cloud mixing ratio q_c, and the constants of the mass-velocity relation of rain.

Figure 3.1 shows the rain production rates of the WSM6* scheme for two different number concentrations of cloud droplets. For $N_c = 0.5 \times 10^8$ m^{-3} the critical mixing ratio is very small and autoconversion large. For $N_c = 3.0 \times 10^8$ m^{-3} the autoconversion rate is reduced and sets in for a mixing ratio higher than approximately 0.61 g kg^{-1}. However, in both cases the critical mixing ratio is smaller than in the Kessler scheme and higher autoconversion rates are gained. Obviously, for a rain mixing ratio of 0.4 g kg^{-1} the sum of autoconversion and accretion in the Kessler scheme is only slightly higher than only accretion in the WSM6* scheme.

Heterogeneous freezing (Pihtf) reduces the cloud water content, when temperatures

are between 0°C and −40°C. The corresponding term is formulated as

$$\text{Pihtf} = 100 \times \left[\exp\left(0.66(T_0 - T)\right) - 1\right] \frac{\rho q_c^2}{\rho_w N_c} \tag{3.23}$$

and follows from Bigg (1953), who showed that the freezing temperature of supercooled water depends on the liquid water volume. The right term in equation 3.23 expresses this volume dependency, while the exponential function poses the temperature dependency. Obviously, for low cloud droplet number concentrations the freezing process of supercooled cloud water increases, because the heterogeneous freezing is inverse proportional to N_c. For low cloud number concentrations N_c (large cloud droplets) the freezing will be higher.

3.4.3 Thompson

Thompson et al. (2004) and Thompson et al. (2008) added a large number of improvements to the Reisner et al. (1998) scheme, which is implemented in the NCAR Penn State Mesoscale Model Version 5 (MM5). The scheme has been further developed, in order to better capture winter precipitation with drizzle and freezing-drizzle and aims at a more accurate forecast of aircraft icing. The implementation of the snow category has been strongly modified as well. Already Reisner et al. (1998) showed that a prognostic ice number concentration is important for a good agreement with observational data. Thus, the Thompson scheme does not only predict six hydrometeor mixing ratios, including vapor, cloud water, rain, snow, ice, and graupel, but additionally predicts the ice number concentration.

Following Walko et al. (1995), general gamma functions describe the shapes of the water, graupel, and ice crystal size distributions, which can be expressed as

$$N(D) \;=\; N_0 D^{\mu} \exp(-\lambda D)\ , \tag{3.24}$$

where N_0 is the y-intercept, λ the slope, and μ a shape parameter, which determines the diameter of the modus of the distribution. Note that the gamma distribution reduces to the exponential Marshall-Palmer size distribution, if μ is zero. Exponential size distributions are assumed for the liquid, ice, and graupel species in section 6.3 within the Thompson simulation. In section 6.4.2 the sensitivity of the precipitation field to the size distribution of the graupel species is tested by assuming $\mu = 1$ for the graupel size distribution.

In the Thompson scheme, the rain and graupel intercepts depend on their mixing ratio. Thereby a reduction of the mixing ratios increases the number concentration. For a plot of the mass-weighted terminal velocities consult Thompson et al. (2008). A comparison to Fig. 3.2, which shows the assumptions made in the WSM6*

scheme, reveals that in both schemes the terminal velocity of snow increases linearly with its mixing ratio. However, the curve in the Thompson scheme is steeper and results in a lower terminal velocity for small amounts of snow. Due to the varying y-intercepts of rain and graupel their terminal velocities increase non-linearly with mixing ratio in the Thompson scheme, causing a very small fall speed at low mixing ratios and a very high terminal velocity for larger mixing ratios. These relations aim at a better representation of the terminal velocity of drizzle and small rain particles. For large mixing ratios the terminal velocity of graupel is similar to a typical assumption made for hail. Another change to the terminal velocity is included, as melting snow and graupel are assumed to fall with the same speed as rain.

In order to account for a larger number of small snow particles and a smaller number of large particles, Thompson et al. (2008) applied the sum of an exponential and gamma function for the snow size distribution. Furthermore, in contrast to other bulk microphysics schemes, a non-spherical snow crystal mass-diameter relation is assumed, which is now expressed as $m(D) = 0.069D^2$, instead of using the spherical $m(D) = \frac{\pi}{6}\rho_s D^3$ relation.

In contrast to the WSM schemes, but similar to Lin et al. (1983), a temperature dependent primary ice number initiation is applied. The relation follows Cooper (1986) and can be written as

$$N_i = 0.005 \exp\left[0.304(T_0 - T)\right] \ . \tag{3.25}$$

A complete list of all participating mass exchange terms is included in Thompson et al. (2008). One of these processes, namely the conversion of rimed snow to graupel, is discussed next. Thompson et al. (2008) discuss the conditions that need to be fullfilled to transform snow to graupel. They computed the ratio of riming of snow and depositional growth of snow and assumed a linear increase of the graupel production, as soon as a certain critical ratio is reached. Explicitly, as the ratio increases from 5 to 30, the graupel production enhances from 5 % to 75 % of the riming rate. The residual part of the riming production contributes to the snow category. To further investigate its degree of influence, a modified assumption will be applied in an experiment in section 6.4.3. Figure 3.3 shows the growth rate of the graupel mass as a function of the ratio between riming of snow and depositional growth of snow. Both the original and the altered assumptions are plotted. The modification implies that graupel is produced already for a ratio of 3. Furthermore, the percentage of transformed rimed snow reaches from 25 % to 95 %, which is always at least 20 % more than in the original formulation.

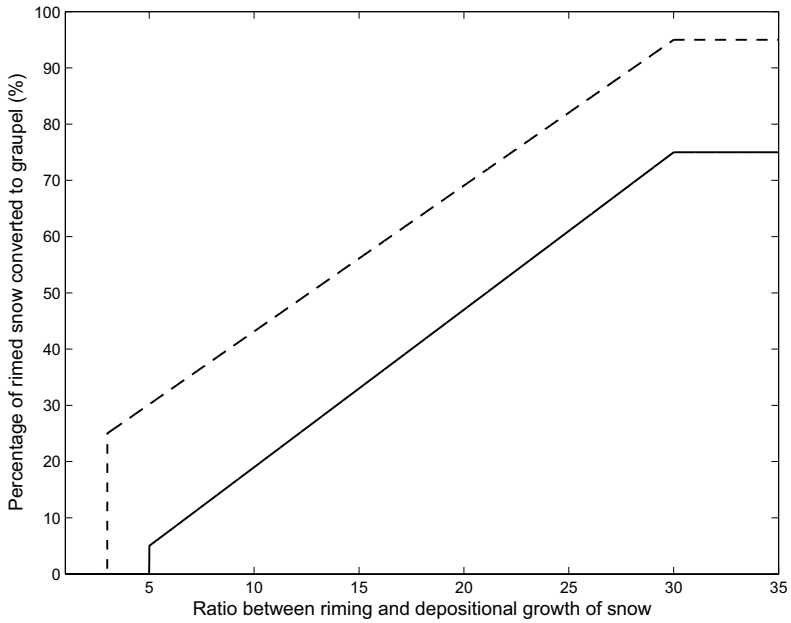

Figure 3.3: The solid line shows the original assumption in the Thompson scheme for the percentage of rimed snow transformed to snow vs. the ratio between riming growth and depositional growth of snow. The dashed line shows an enhanced graupel production, which is tested in the sensitivity experiment in section 6.4.3.

3.5 Statistical scores for model validation

In order to allow a detailed comparison between model output y and observational data o, the predicted precipitation is interpolated from m model surface grid points to n rain gauge stations. With horizontal gridpoint distances of 3 and 1 kilometer in the WRF domains 3 and 4, respectively, the model grid resolution is sufficiently high to allow for an interpolation to the coarser station net. A triangle-based cubic interpolation is applied. In order to validate and estimate the performance of a forecast, statistical scores are calculated:

Domain average: The domain average gives a first estimate of the total amount of precipitation, which can be compared to other simulations. It is simply defined as the arithmetic mean precipitation of all surface grid points m:

$$\mathrm{AVG} = \frac{1}{m}\sum_{i=1}^{m} y_i \tag{3.26}$$

Station averages: Station averages are both calculated for n station measurements and the forecasted precipitation interpolated to n station locations. In the following the average values retrieved from interpolated model forecasts and station measurements will be abbreviated as AVG_{sy} and AVG_{so}, respectively. A model's tendency to over- or underestimate precipitation can be identified by

subtracting the average values AVG_{sy} and AVG_{so}. For model-model intercomparison the above listed domain-averaged precipitation is more meaningful, because it represents the larger data set of m gridpoints. The simulated and observed station averages are simply the arithmetic mean value of precipitation at all n stations:

$$\mathrm{AVG}_{sy} = \frac{1}{n}\sum_{i=1}^{n} y_i \qquad \text{and} \qquad \mathrm{AVG}_{so} = \frac{1}{n}\sum_{i=1}^{n} o_i \tag{3.27}$$

Root-mean squared error: The model performance can be validated by averaging the squared differences between forecasted and observed precipitation at each station. This so called mean squared error (MSE) represents the average error of the field. In order to retain the correct units of the quantity and for a better interpretation, the root-mean squared error (RMSE) is calculated by taking the root of the MSE. Apparently, a RMSE score of zero belongs to a perfect forecast. However, it is difficult to put an accurate interpretation on non-zero RMSE scores, as its value is not primarily related to a certain model skill. Thus, only a comparison to scores retrieved from different simulations is meaningful:

$$\mathrm{RMSE} = \left(\frac{1}{n}\sum_{i=1}^{n}\left(y_i - o_i\right)^2\right)^{0.5} \tag{3.28}$$

Normalized absolute error: For large amounts of precipitation, as it is the case in this study, a more appropriate score is the normalized absolute error (NAE):

$$\mathrm{NAE} = \frac{1}{n}\sum_{i=1}^{n}\frac{\left(y_i - o_i\right)^2}{0.5(y_i + o_i)} \tag{3.29}$$

Obviously, the denominator is the arithmetic mean of the observed and predicted precipitation. Hence, the NAE gives less weight to large amounts of precipitation and emphasizes smaller amounts. The NAE is calculated by scaling the mean absolute error (MAE) with the relative error and can be rewritten as

$$\mathrm{NAE} = \frac{1}{n}\sum_{i=1}^{n} \overbrace{|y_i - o_i|}^{\mathrm{MAE}} \; \overbrace{\frac{|y_i - o_i|}{0.5(y_i + o_i)}}^{\text{relative error}} \tag{3.30}$$

Chapter 4

Synoptic situation and precipitation field

Before model simulations and precipitation fields are analyzed, a solid background of the prevailing synoptic situation is necessary. Subsequently, observed precipitation fields need to be explored in order to understand the spatial precipitation distribution. Detailed investigation of observed precipitation structures on an Alpine scale is essential for the validation of the numerical simulations conducted during this study. For this work both rain gauge measurements and radar composite data are available. Technical details on precipitation measurements are presented in section 2.2.

In section 4.1 ECMWF analysis data is used to described the large-scale synoptic situation. Analysis of daily precipitation measurements are presented in section 4.2, in order to obtain an overview of the affected areas. Finally, precipitation patterns retrieved from the CERAD radar composites and automatic rain gauge measurements are shown in a chronological sequence in section 4.3.

4.1 Large-scale synoptic situation

For better clarity of the synoptic situation the geopotential height in 300 hPa and relative humidity at 700 hPa, as depicted by the analysis of the European Centre of Medium-Range Weather Forecasts (ECMWF), is shown in Figure 4.1. On 20 August an upper trough begins to cut off above France (see Fig. 4.1a). Embedded in the eastward progressing system it passes the Alps on its southside and deepens until 22 August (see Fig. 4.1c and MeteoSchweiz 2006b). Along with the upper trough comes a surface depression with its occluded frontal system. The surface low over the Gulf of Genoa carries Mediterranean air counterclockwise around the Alps and finally forms a strong low-level jet directed towards the northern Alpine slopes.

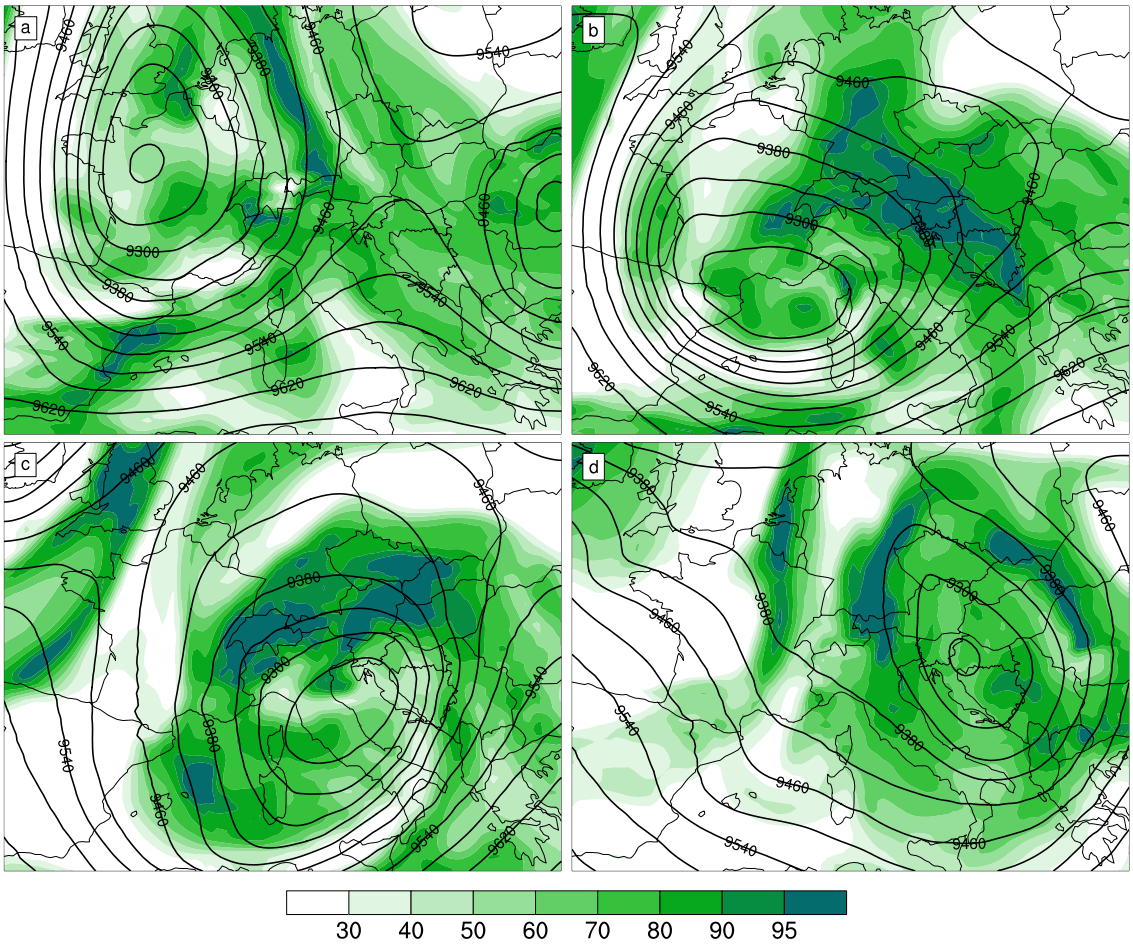

Figure 4.1: 300-hPa geopotential height (40 gpm increments) and 700-hPa relative humidity (gray shaded) in % of the ECMWF analysis at (a) 0600 UTC 20 Aug, (b) 0600 UTC 21 Aug, (c) 0600 UTC 22 Aug , and (d) 0600 UTC 23 Aug 2005.

Batches of high humidity (> 95%) are positioned at the southeastern parts of the Alps at 0600 UTC 21 August, but are advected to the northern Alpine slopes until 22 August 0600 UTC (see Figs. 4.1b,c).

Figure 4.1d finally shows a very sharply confined north-south orientated band of high moisture over western Austria and its Alpine foreland at 0600 UTC 23 August , which slowly propagates together with the cyclone to the East. Winds in the northern Alpine regions are northeasterly on 20 August, but turn to north on 22 August and therefore blow nearly perpendicular to the Alpine barrier. Figures 4.2c,d show that the wind speeds in 850 hPa are approximately 12 m s^{-1} during the period of Alpine parallel flow, and roughly 17 m s^{-1} during the period of low-level flow perpendicular to the Alps. During the entire event the quasi-stationarity of the system and the relatively slow eastward propagation are one reason for the continuous moisture supply at the northern rim of the Alps. The prevailing cyclonic synoptic situation over the Alps might also attribute to a large-scale lifting process.

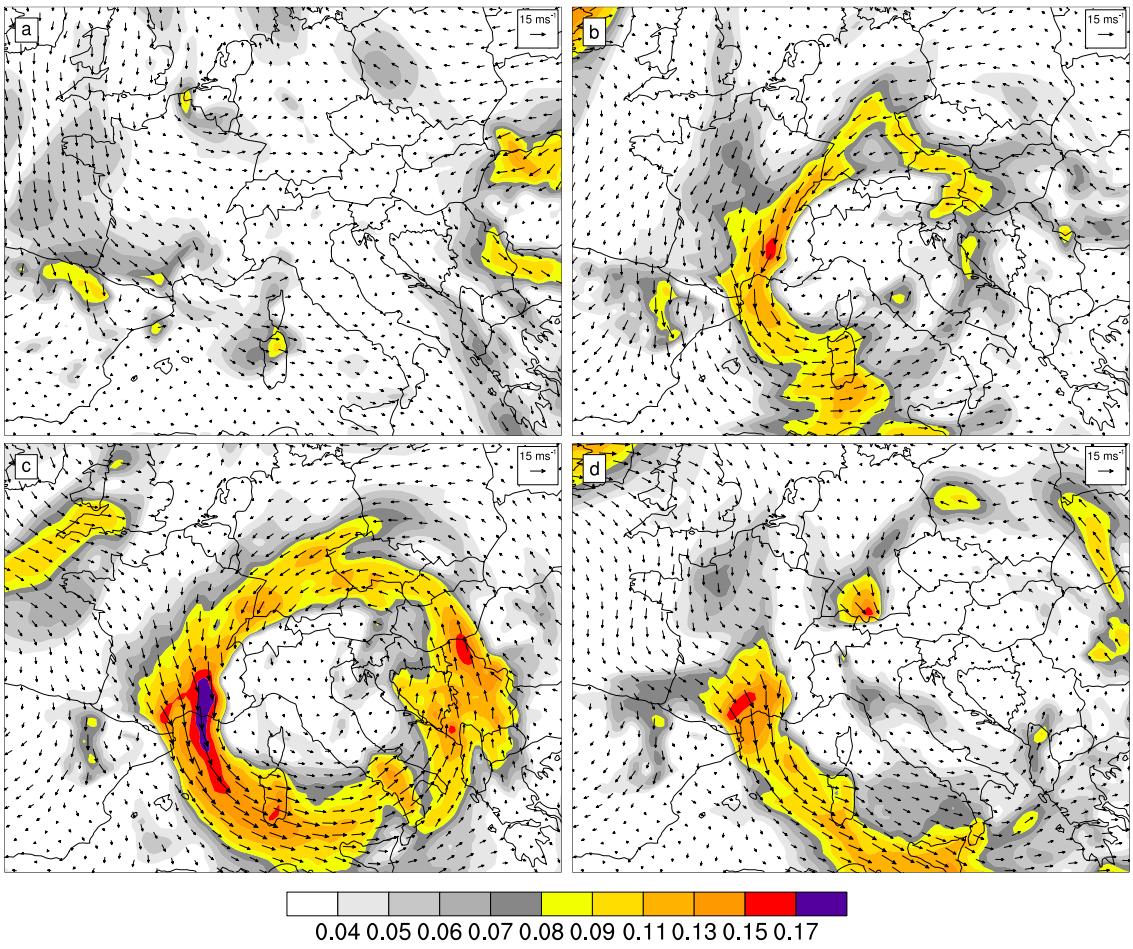

Figure 4.2: 850-hPa moisture flux (kg m^{-2} s^{-1}) and wind vectors of the ECMWF analysis at (a) 0600 UTC 20 Aug, (b) 0600 UTC 21 Aug, (c) 0600 UTC 22 Aug , and (d) 0600 UTC 23 Aug 2005.

This type of cyclone movement can roughly be categorized as a "Zugstrasse-Vb" type (Van Bebber 1890) and is often accompanied by heavy precipitation at northern Alpine slopes (Mudelsee et al. 2004). Differences to the Vb movement occur during the final period of cyclolysis during the evening of 23 August, when the surface pressure system weakens over eastern Europe, instead of moving north, which would be the typical path for a Vb cyclone. Other European flooding events were induced by similar large scale synoptic conditions, e.g., in Switzerland during June 1910 and Germany in August 2002 (MeteoSchweiz 2006b).

4.2 Daily accumulated precipitation field

Figure 4.3 shows daily accumulated precipitation from KLIMA measurements for the periods between 0600 UTC and 0600 UTC on the following day. On 21 August

highest amounts of precipitation are gained in central Switzerland. There, a large area is affected by more than 90 mm of precipitation, and at some stations more than 120 mm of precipitation are measured (e.g., Stans 135 mm, Sangernboden 121 mm, Napf 127 mm, Kurzeneialp 123 mm). The maximum of daily precipitation occurs in Wasen in Emmental with 170.7 mm. Significantly less precipitation falls over the southern parts of Switzerland, resulting in a quite strong north-south precipitation gradient.

Apart from the maximum precipitation over the northern Alps in central Switzerland, a secondary, less intensive precipitation maximum can be identified over northern parts of Switzerland and Baden-Wurttemberg. In Fig. 4.3a two preferred areas of increased precipitation appear, which are elongated from northeast to southwest in a banded manner. The two bands are clearly distinguishable by a relative minimum of precipitation between them. The one to the north produces slightly more rain ($>$ 75 mm), whereas the one to the south seems to be less intensive. These features give rise to the assumption that convection increased the rainfall already ahead of the main Alpine rim. Moderate precipitation at the eastern edge of the Alps is well recognizable and signalizes the orographic lifting of the northward moving air mass (see Figs. 4.1b and 4.2b).

Due to the eastward drift of the cyclone, the winds at the northern Alps turn from east to north during 22 August, causing higher amounts of accumulated precipitation than on 21 August. Figure 4.2b reveals enormous sums of precipitation at stations located along the northern rim of the Alps. More than 180 mm are measured at several stations, e.g., Säntis (187 mm), Au (214 mm), Schoppernau (194 mm), and Balderschwang (216 mm). A maximum precipitation of 241.8 mm is recorded in Weesen. Again, the southern parts of Switzerland receive significantly less precipitation than the northern flanks. As a consequence of the strong east-west directed moisture gradient (see Fig. 4.1d), a strong gradient of precipitation also appears at the eastern end of the rainband. Furthermore, Fig. 4.3b shows a strong spatial variability of precipitation over the Alpine foreland. Heavy precipitation in Switzerland seems to be bound to high orography with little precipitation falling over the Alpine foreland. However, intermediate precipitation is observed already somewhat upstream of the Alpine crest to the north of the western parts of Austria.

Finally, during 23 August precipitation diminishes also in the Bavarian regions (see Fig. 4.3c), however with still relatively high observed precipitation sums in Wallgau (73 mm), Kochel (73 mm), Samerberg (85 mm), Kreuth (85 mm), Wendelstein (102 mm), and Aschau (107 mm). Maximum precipitation is measured in Niederndorferberg/Austria (118.1 mm). All of these stations are located at the

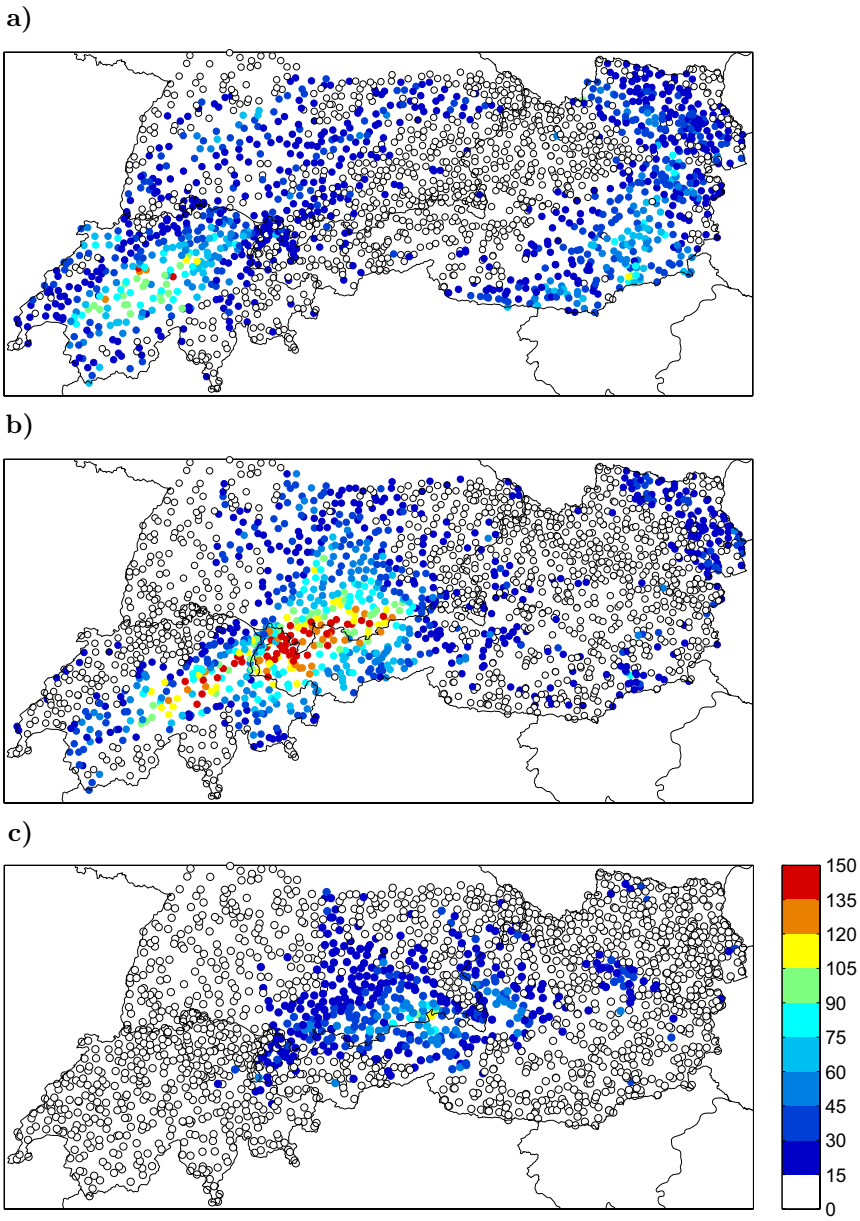

Figure 4.3: Daily accumulated precipitation (mm) from KLIMA measurements from 0600 UTC to 0600 UTC on the following day for (a) 21 Aug, (b) 22 Aug, and (c) 23 Aug 2005.

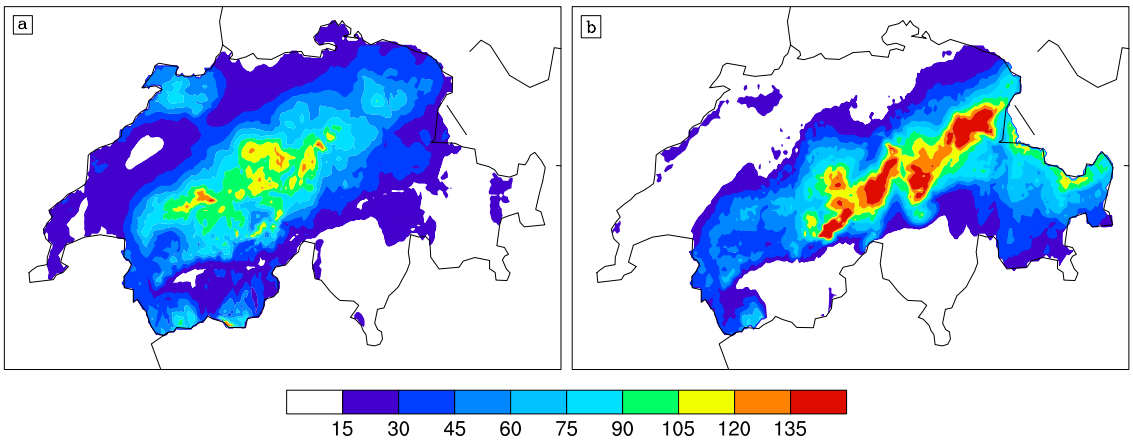

Figure 4.4: Gridded MeteoSwiss pluviometer data of accumulated precipitation (mm) from 0600 to 0600 UTC on the following day for (a) 21 Aug and (b) 22 Aug 2005. Note that observations are only available over Switzerland.

northern Alpine edge. Obviously the area of maximum accumulated precipitation is now, in comparison to the previous day, located even further to the east. Other Alpine regions are not affected by mentionable precipitation any longer.

For quantitative analysis MeteoSchweiz (2006b) and MeteoSchweiz (2006a) interpolated precipitation measured by 482 rain gauge stations, including the above discussed Swiss observational data, onto a regular grid with approximately 2 km horizontal grid spacing. Furthermore, climatological and topographic effects have been taken into account. Figure 4.4 shows the gridded MeteoSwiss pluviometer data, which gives an overview of the quantitative precipitation distribution over Switzerland.

On 21 August the maximum precipitation over central Switzerland is clearly visible in Fig. 4.4a. Again it indicates the relatively small area affected by heavy precipitation, insignificant precipitation to the south of the main Alpine crests, and the considerable amounts of precipitation over the Swiss Alpine foreland. Also a local maximum over the Swiss Jura mountains is recognizable.

Figure 4.4b signalizes even heavier precipitation over the Alpine rim during 22 August and shows stronger precipitation gradients both towards the north and to the south of the main Alpine crest. Still little precipitation is produced over southern parts of Switzerland, but in contrast to 21 August also the Alpine foreland records significantly less precipitation than the main crest. Due to the cyclone movement, as already mentioned above, heavy precipitation is now located some kilometers further to the east.

4.3 Chronological analysis of precipitation patterns

In the following, measurements from the Central European Weather Radar Network (CERAD) are presented as a sequence of 6-hour totals of precipitation in order to elucidate the temporal evolution of precipitation structures. The data quality, known problems, and technical details are discussed in the corresponding chapter on observational rain measurements in section 2.2. For a better quantitative analysis, additionally, 12-hour accumulated precipitation from automatic weather stations are included in the following.

Figures 4.5a,b show plots with 6-hours accumulated precipitation retrieved from the radar images between 0000 UTC 21 August and 1200 UTC 21 August. Although heavy precipitation is not yet visible, it should be mentioned that precipitation occurring ahead of the main event had already moistened the surface which might have played an essential role for the hydrological run off (Bezzola and Hegg 2007). Moderate precipitation with localized peaks only occurs over southeastern Austria, where the northwestward directed moisture flux (see Fig. 4.2b) impinges on the southeastern rim of the Alps. Figure 4.5c shows a few automatic weather stations

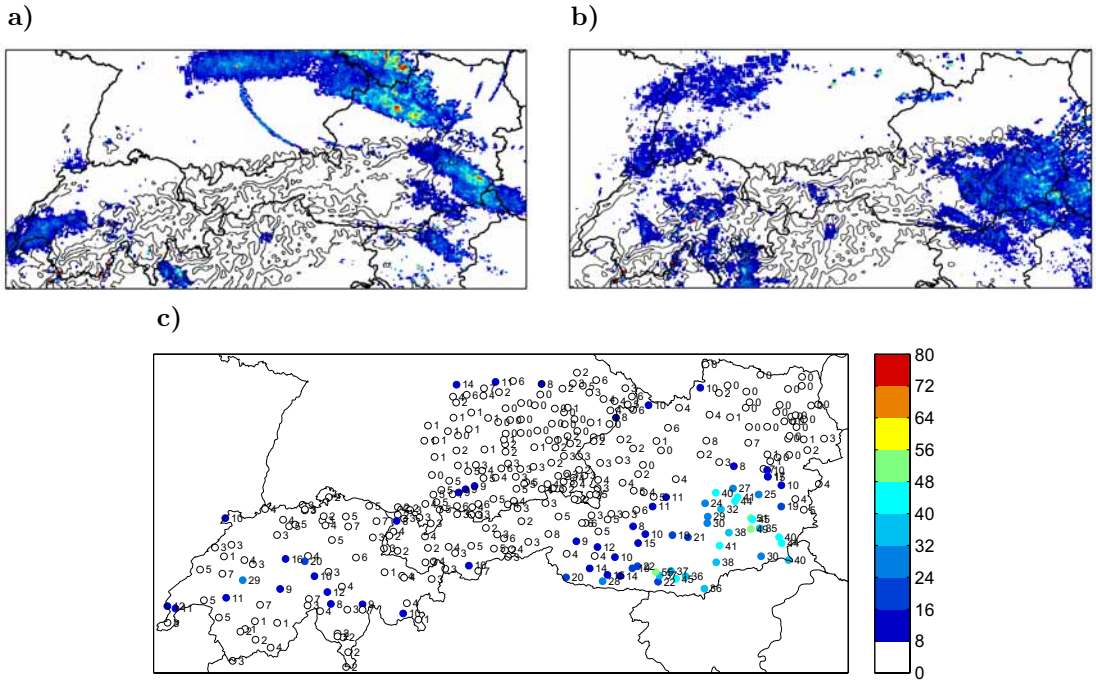

Figure 4.5: Accumulated precipitation depicted from radar composites between (a) 0000 UTC 21 Aug and 0600 UTC 21 Aug, (b) 0600 UTC 21 Aug and 1200 UTC 21 Aug, and from (c) automatic rain gauge measurements between 0000 UTC 21 Aug and 1200 UTC 21 Aug 2005.

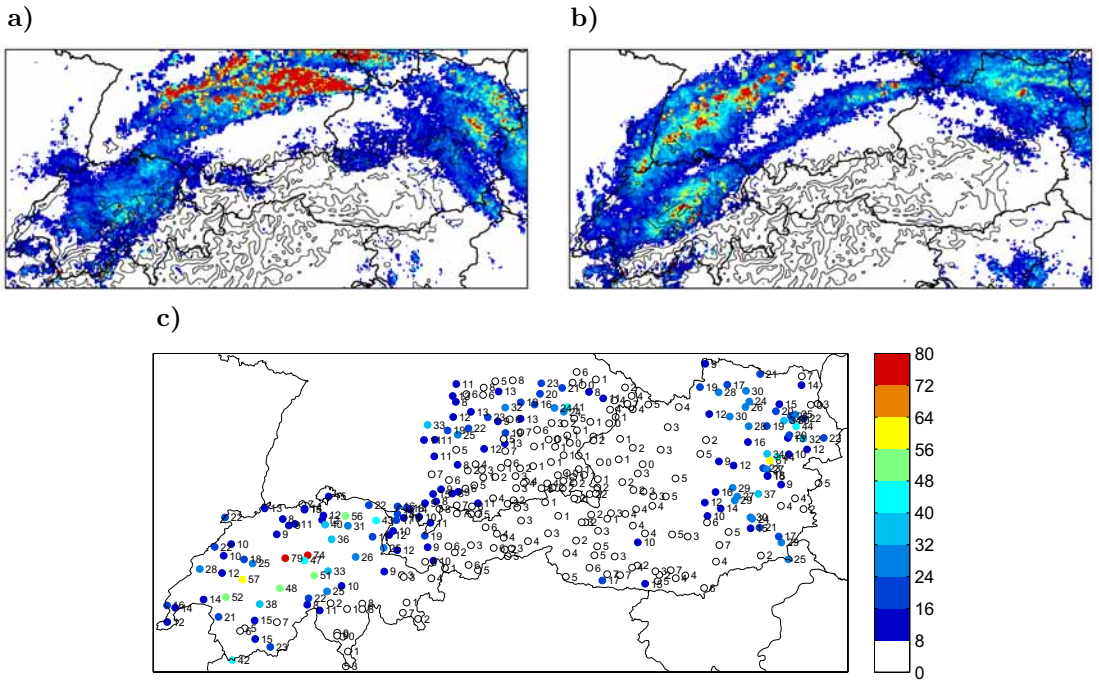

Figure 4.6: Accumulated precipitation depicted from radar composites between (a) 1200 UTC 21 Aug and 1800 UTC 21 Aug, (b) 1800 UTC 21 Aug and 0000 UTC 22 Aug, and from (c) automatic rain gauge measurements between 1200 UTC 21 Aug and 0000 UTC 22 Aug 2005.

with rain measurements exceeding 50 mm. Disordered weak echoes come from south and central Switzerland and the northern and southern parts of the Black Forest mountain region. A maximum of accumulated precipitation of 55.1 mm is obtained in Arriach/Austria. Other areas receive only little precipitation (< 15 mm), except for central Switzerland, where two stations receive more than 20 mm.

In Fig. 4.6a large areas of extremely high radar echoes appear over southern Germany after midday of 21 August. The narrowness of these two visible high-intensity features gives reason for the assumption that convective cells are triggered in the westerly flow and that hail might have caused high radar reflectivities in these regions. Lightning plots[1] prove that this convective activity is right at the same locations and also show the westward movement of these cells. Figure 4.6c shows that remarkable amounts of precipitation (e.g., 33 mm in Günzburg, 32 mm in Geisenfeld-Eichelberg, 41 mm in Mamming-Schneiderberg) are obtained at a few scattered stations in northwestern Bavaria. In contrast to that, the stations in the southern parts of Bavaria, which are located closer to the Alps, receive less than 10 mm. Only few of the stations located close to the Bavarian Alps measure higher amounts, e.g., 18 mm in Sigmarzell. Precipitation over the southeastern parts of

[1]available at: http://www.wetterzentrale.de

Austria has increased, but in comparison to the previous period, the location shifted slightly to the North. Also the Swiss Jura and the Vosges mountain range are now affected by precipitation. Weak echoes appear over these regions. Over central Switzerland and its adjacent Alpine foreland an increase in precipitation is visible. During this period the onset of vast precipitation occurs over central Switzerland and Fig. 4.6c shows a large area receiving more than 40 mm in 12 hours. But in contrast to the previous period, now highest intensities are not restricted to central Switzerland anymore. Strong signals are also caused by convective precipitation over the Alpine foreland in northeastern Switzerland.

Characteristic features appearing between 1800 UTC 21 August and 0000 UTC 22 August (see Fig. 4.6b) are again two narrow bands of large accumulated precipitation. Both are aligned from northeast to southwest. The one to the North reaches from northern Bavaria to the Swiss Jura mountains and shows heavier intensities than the southern band. The latter one reaches from northern parts of Austria to central Switzerland. Figure 4.6a, together with 4.6b, confirm the results from the rain gauge measurements over northwestern Bavaria (see Fig. 4.6c) and add some valuable information about the banded structure of these precipitation features. High intensities are also captured over the Czech Republic. Maximum precipitation falls over the northern flanks of the central Swiss Alps, the Black Forest mountains and the Swiss Jura regions. The maximum 12-hour sum is measured in Napf (79 mm). But again, it should be mentioned, that precipitation is not completely bound to orography, but appears already upstream over the Alpine foreland. Affected areas to the east of Switzerland obtain significantly less precipitation during this period.

North of the Alps six hours later the circle shaped large-scale rain pattern, caused by the counterclockwise moisture flux (see Fig. 4.2c), is still visible (see Fig. 4.7a). Moderate precipitation sums are measured over the Czech Republic and again highest intensities are gained over Switzerland. Banded patterns of precipitation are also recognizeable over the Swiss and Bavarian Alpine foreland. High intensities are still visible over the Swiss Jura. Figure 4.7c shows that at the eastern edges of the Alpine barrier precipitation has decreased.

Figure 4.7b demonstrates a further extension of highest precipitation intensities along the Swiss northern slopes to the east between 0600 UTC 22 August and 1200 UTC 22 August. This pattern results from the movement of the cyclone and the eastward propagating moisture (see Figs. 4.2c,d). Moderate precipitation sums appear over western Austria and southern Germany. The precipitation increases over Vorarlberg and southern parts of Bavaria, where several stations along the

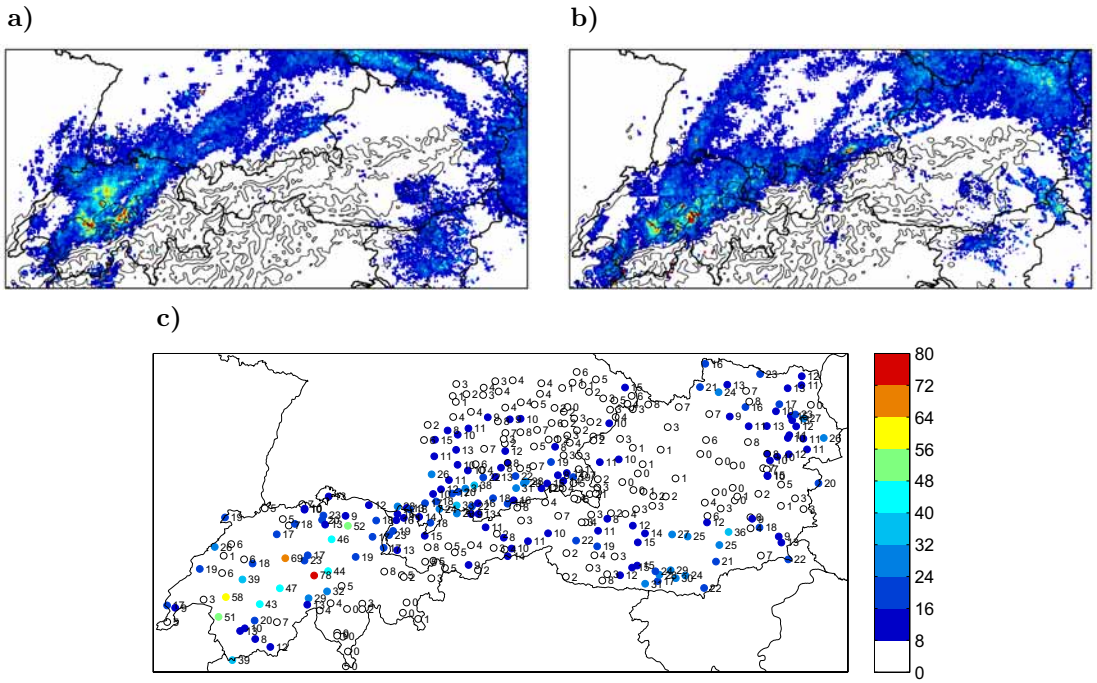

Figure 4.7: Accumulated precipitation depicted from radar composites between (a) 0000 UTC 22 Aug and 0600 UTC 22 Aug, (b) 0600 UTC 22 Aug and 12 UTC 22 Aug, and from (c) automatic rain gauge measurements between 0000 UTC 22 Aug and 1200 UTC 22 Aug 2005.

northern Alpine foothills receive more than 20 mm (see Fig. 4.7c). Again the northern parts of Switzerland are covered with precipitation and highest intensities during this period are gained over northern Alpine flanks in central Switzerland. Figure 4.7c shows that by far the highest amounts of precipitation are accumulated in central Switzerland. Several Swiss stations obtain more than 40 mm during this period. Maximum precipitation of 77.7 mm is recorded in Engelberg. Interestingly, a sharp precipitation gradient appears across the Swiss Alps, as the southern stations receive less than 5 mm during this period. In other words, due to the northeasterly flow impinging on the northern Alpine rim (see Fig. 4.1c and 4.2c), the southern parts of Switzerland, which are located at the leeside of the Alps, obtain only little rainfall. Besides the west-east elongated precipitation sums, at least one northeast-southwest orientated band with large amounts of precipitation appears over Baden-Wurttemberg and northern Switzerland. This feature is presumably the result of precipitation from convective cells that have been carried along with the flow towards the Alps.

Between 1200 UTC 22 August and 0000 UTC 23 August precipitation over western Switzerland decreases and maximal precipitation sums are obtained in eastern parts of Switzerland, in western Austria, and in the German Alpine foreland (see

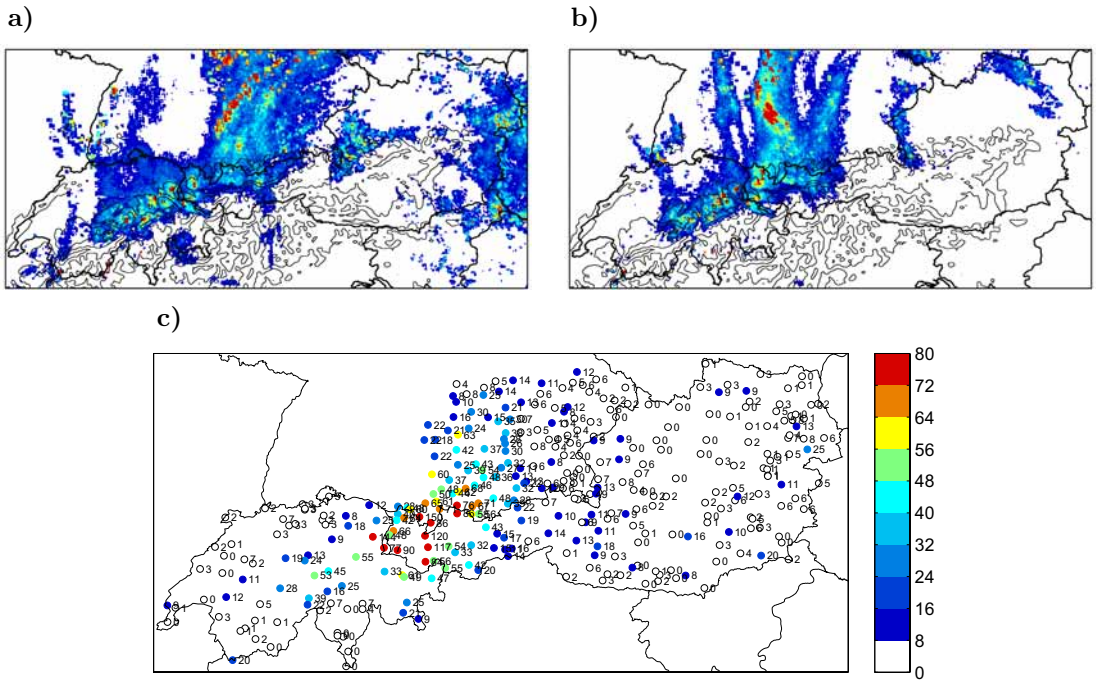

Figure 4.8: Accumulated precipitation depicted from radar composites between (a) 1200 UTC 22 Aug and 1800 UTC 22 Aug, (b) 1800 UTC 22 Aug and 0000 UTC 23 Aug, and from (c) automatic rain gauge measurements between 1200 UTC 22 Aug and 0000 UTC 23 Aug 2005.

Fig. 4.8a). Many of the eastern Swiss stations still obtain more than 45 mm (see Fig. 4.8c). The echoes received slightly north of Bavaria are unreasonably high and could result from several problems that are linked to radar measurements. Among these difficulties the presence of hail or an inappropriate Z-R relation might cause these unrealistic rain rates. Further enhancement of precipitation occurs in western parts of Austria. Again, here the radar images clearly exhibit tracks of convective precipitation located slightly north of the Vorarlberg region. This is the beginning of intensive rainfall over western Austria. Locations of high rain amounts measured by rain gauges (see Fig. 4.8c) are consistent with these results. Automatic measurements in western Austria and in the adjacent southern Bavarian region reveal extensive precipitation. The highest 12-hour sums are measured in Galzig (117 mm), Warth (120 mm), Säntis (144 mm), and Balderschwang (149.7 mm). Moderate amounts of rain is measured in northern Switzerland and also over the eastern end of the Alps.

Figure 4.8b points out extensive rainfall over a sharply restricted area during the period between 1800 UTC 22 August and 0000 UTC 23 August. To the east rainfall has now proceeded into southern parts of Bavaria, but no signals are received from southeast Bavaria, yet. Figure 4.8c proves that only negligible amounts of rainfall are obtained in southeastern Bavaria and that the east-west precipitation

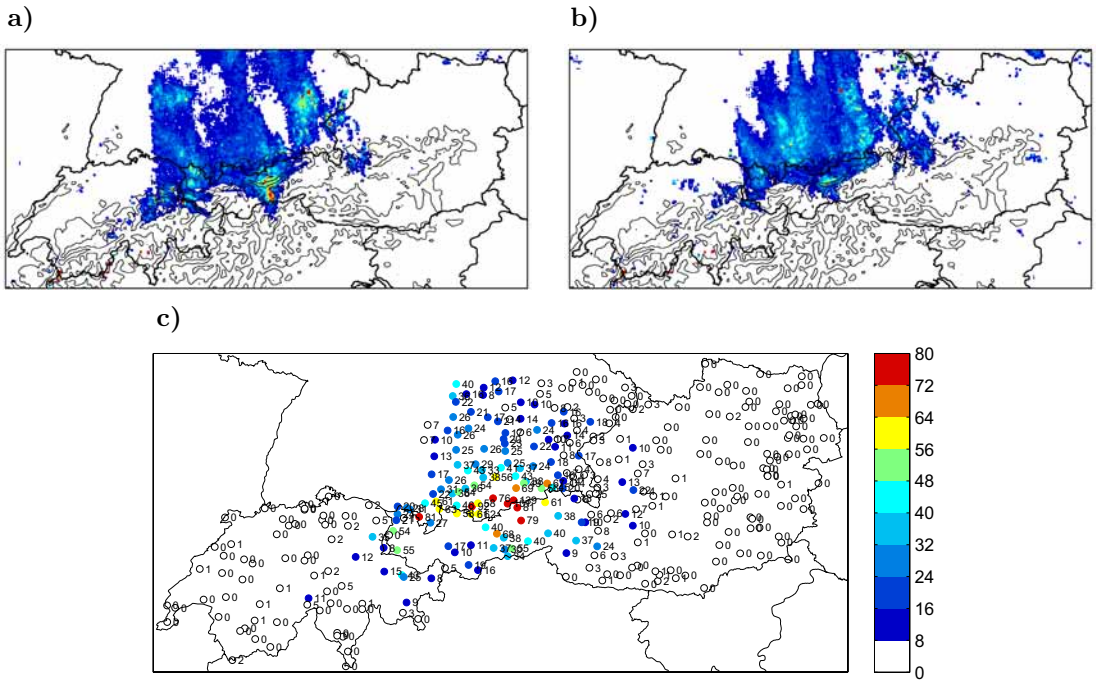

Figure 4.9: Accumulated precipitation depicted from radar composites between (a) 0000 UTC 23 Aug and 0600 UTC 23 Aug, (b) 0600 UTC 23 Aug and 1200 UTC 23 Aug, and from (c) automatic rain gauge measurements between 0000 UTC 23 Aug and 1200 UTC 23 Aug 2005.

gradient proceeds to the North, where again the western stations receive more precipitation than the eastern ones. The observed precipitation gradient can be better understood, when bearing in mind, that the moisture field (see Fig. 4.1d and 4.2d) exhibits a north-south elongated band of increased humidity, which propagates slowly from West to East. The western boundary of the precipitation area is located over central Switzerland. Heavy precipitation is measured at several locations within the precipitation area. Most of them are located in the eastern Swiss Alps and over the mountains in Vorarlberg. Another one is embedded into the southward approaching flow, right upstream of Vorarlberg. Precipitation over Switzerland seems to be restricted to the northern Alpine mountains, whereas heavy rainfall over the foreland stopped. Figure 4.8c reveals that this spatial distribution results in unequal precipitation amounts over the Swiss and German Alpine foreland.

During the period between 0000 UTC 23 August and 0600 UTC 23 August a further shift of heavy precipitation to the east is visible in Fig. 4.9a. Still intermediate precipitation is affecting the very eastern parts of Switzerland, but heavy precipitation in Switzerland ended after 0000 UTC 23 August. To the eastern end of the precipitation band southeastern Bavaria is now affected by rainfall. The period between 0600 UTC 23 August and 1200 UTC 23 August is

characterized by widespread rainfall over southern Germany and its Alpine flanks (see Fig. 4.9b). But still Vorarlberg and Tirol receive moderate precipitation and again the restricted width of the precipitation field can be recognized in Fig. 4.9b. In agreement with rain gauge observations (see Fig. 4.9c), the highest reflectivities are observed in Vorarlberg, Tirol, and Bavaria. Several Bavarian stations record more than 50 mm precipitation and only the most southeastern parts of Germany record significantly less amounts of precipitation. Maximum rainfall during this period is obtained in Lenggries (101 mm) and Kreuth (138.8 mm). Stations in Tirol/Austria receive 68 mm (Innsbruck), 79 mm (Jenbach), and 81 mm (Achenkirch). Hardly any precipitation is measured at the Swiss stations.

Finally, after 1200 UTC 23 August precipitation is only affecting the southeast of Bavaria and Salzburg (not shown). Radar images show scattered rain showers over southwest Germany and might simply reflect convective habits in the afternoon. Later radar images show no significant precipitation. Rain gauge measurements (not shown) also indicate the ending of heavy precipitation, as only the southeastern Bavarian stations are affected by moderate precipitation. Stations in the Berchtesgaden and Salzburg region record approximately 30 mm. The highest amount is obtained in Aschau/Bavaria (53.1 mm).

Chapter 5

WRF reference run

The National Center for Atmospheric Research Weather Research and Forecasting model (WRF) is used for numerical simulations, in order to investigate the impact of microphysics parameterizations on precipitation amount and its spatial distribution. In this chapter a reference run, using the WRF single-moment bulk microphysics scheme WSM6* (see section 3.4.2), is described. Mesoscale characteristics of the flow over the Alps and a comparison to observed atmospheric conditions are presented in section 5.1. The generated precipitation field is explained and validated in section 5.2. For a description of the numerical setup and experimental design refer to chapter 2.

5.1 Mesoscale aspects and validation

Before precipitation structures are analyzed, mesoscale dynamical aspects of the flow interaction with the Alpine barrier are determined. The flows simulated on the third domain of the reference run are shown in Figs. 5.1a,b and 5.2a,b, which contain the horizontal wind fields and the moisture flux at a just-above-mountain pressure level $p = 700$ hPa and at the nearly terrain-following model-level $\sigma \sim 0.97$, which is at approximately 220 m above ground. This two-way nested simulation WSM6*_2 does not yet use a fourth domain.

At 1800 UTC 21 August, winds over Switzerland are from northeast at 700 hPa (see Figs. 5.1a) and north-northeasterly near the surface (see Fig. 5.2a). The low-level moisture flux is aligned parallel to the Alpine barrier over the Swiss regions and already affecting northern Alpine flanks. Especially in western parts of Switzerland the moist flow is lifted over the northern Alpine mountains at this time. At 0000 UTC 23 August the moisture flux is impinging perpendicular on the northern Alpine rim with a maximum of 0.17 kg m^{-2} s^{-1} at the 700-hPa level over western parts of Austria and eastern parts of Switzerland (see Fig. 5.1b). Winds have picked up and

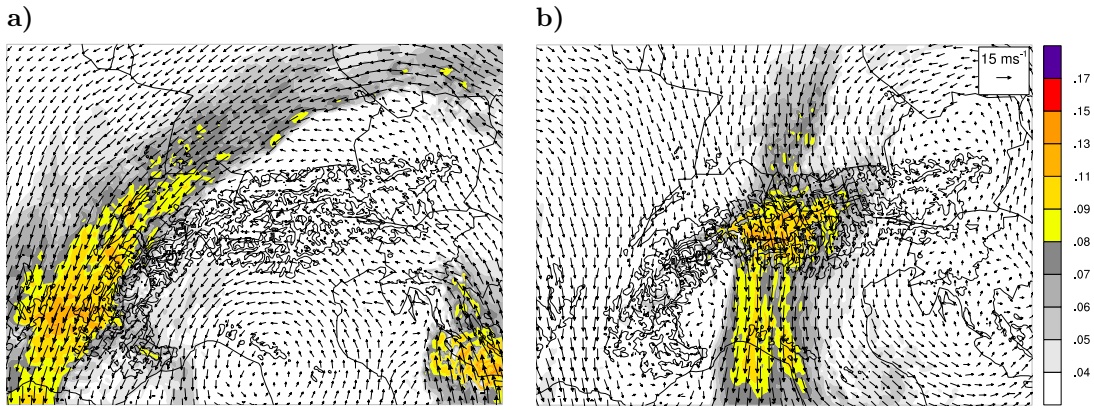

Figure 5.1: Moisture flux (kg m^{-2} s^{-1}) in 700 hPa for domain 3 of the WSM6*_2 run at (a) 1800 UTC 21 August and (b) 0000 UTC 23 August. Black contour lines indicate orography every 1000 m.

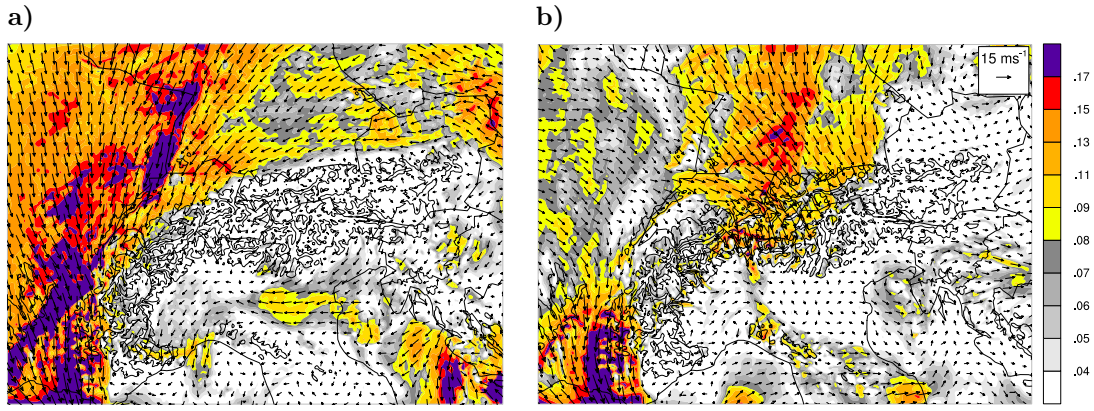

Figure 5.2: Moisture flux (kg m^{-2} s^{-1}) at a near-surface model-level ($\sigma \sim 0.97$, $z \sim$ 220 m) for domain 3 of the WSM6*_2 run at (a) 1800 UTC 21 Aug and (b) 0000 UTC 23 August. Black contour lines indicate orography every 1000 m.

the air mass is flowing over the Alps even at the near-surface level, which is indicated by the high, nearly unmodified moisture flux over the northern Alpine slopes. Low-level decelerations or deflections of the flow were neither visible upstream of central Switzerland in Fig. 5.2a nor upstream of Austria in Fig. 5.2b. The splitting of the low-level flow west of Switzerland (see Fig. 5.2b) is not of relevance for the affected areas. Note that at 0000 UTC 23 August the predicted moisture flux appears already very intensive over southeastern Bavaria. Below, a comparison of the predicted precipitation to the observed precipitation field will reveal an overprediction at these locations, due to the broadening of the highest moisture flux intensities.

The flow regime, which is identified as flow over the mountain, shows that mechanisms of precipitation enhancement triggered by a partial blocking of the flow can not be of relevance at both shown dates. Herewith, this mechanism of orographic precipitation, which is explained in e.g. Rotunno and Ferretti (2001), can not be of importance for an enhancement of precipitation during this heavy precipitation event. Cross-sections of the equivalent potential temperature, which will be shown below, prove the described flow-over regime.

In the following, rawinsonde data from Munich and Stuttgart will be compared to the model-derived vertical profiles. Thereby, the upstream vertical thermodynamic structures and wind profiles are investigated. The positions of both locations are marked in Fig. 5.9a. For both Munich and Stuttgart the atmosphere is nearly moist neutrally stratified (see Figs. 5.3a and 5.3b) at 1200 UTC 21 August. The model captures the temperature gradient at both locations. However, the reference run produces a thin dry adiabatic surface layer in Stuttgart at this time (see Fig. 5.3b), whereas the sounding reveals a moist neutral temperature gradient close to the surface. As a result of the dry mixing, the model is not saturated close to the surface. The humidity profiles above the boundary layer are captured satisfyingly at both dates. For Stuttgart the smooth decrease of humidity with height is well reproduced. For Munich the reference run produces too much moisture in lower levels (see Fig. 5.3a). A comparison to the ECMWF analysis moisture fields (not shown) in mid-tropospheric levels reveals that the position of a sharp moisture gradient with higher humidity to the south and lower humidity to the north is located slightly to far north and barely influences Munich in the simulation.

Vertical wind profiles for Munich at 1200 UTC 21 August are shown in Fig. 5.4. Soundings from the ECMWF analysis have been added to the figure, in order to allow for a quantitative comparison with the WRF model. Figure 5.4a shows that the wind profiles are captured very well at this time and unveils maximum wind speeds of 15 m s^{-1} at 4 km above mean sea level (MSL). The wind direction is continuously from east, but turns to northeast near the surface (see Fig. 5.4b). At

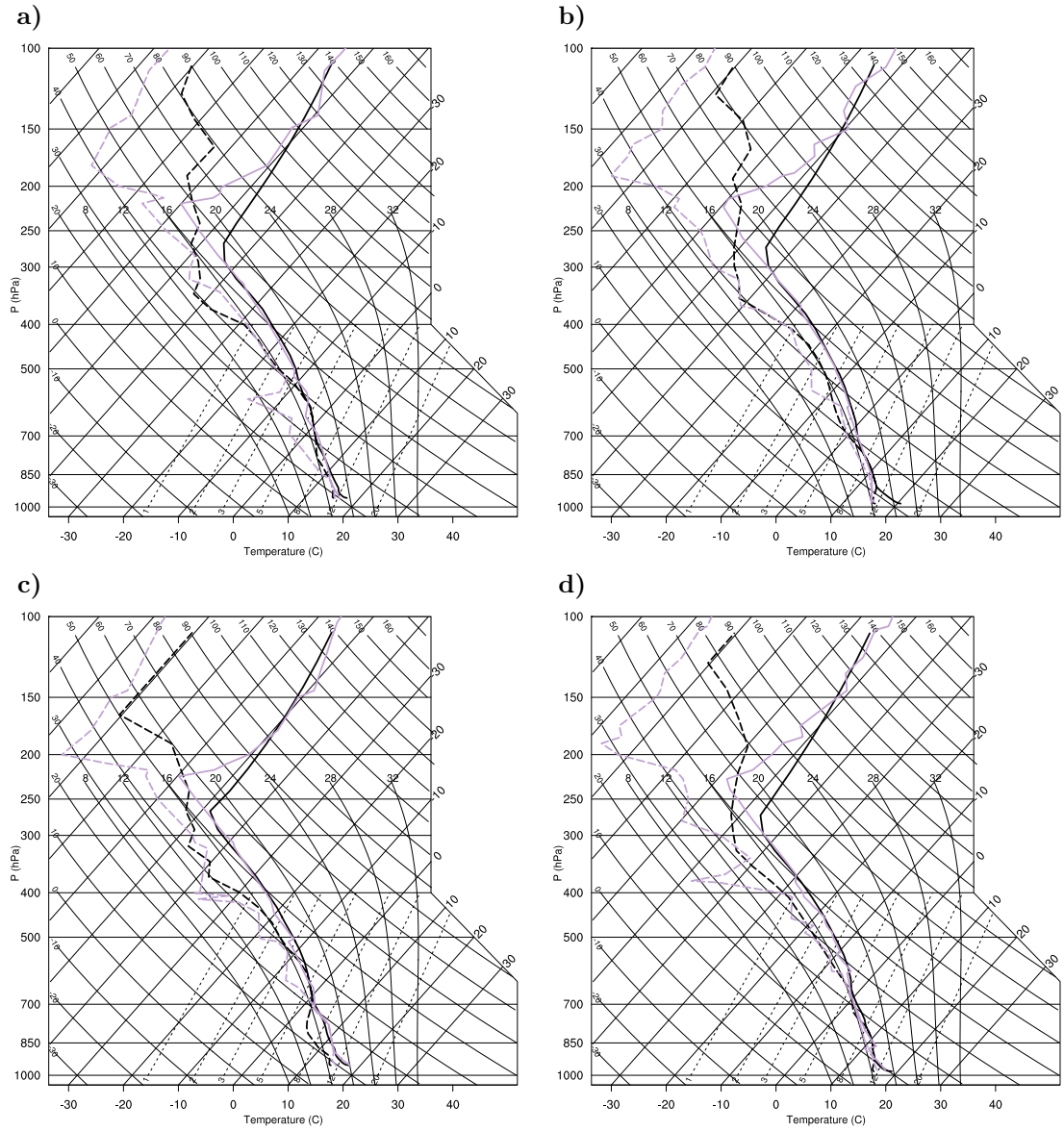

Figure 5.3: Observed (gray) and model-derived (black) skew-T profiles for Munich at (a) 1200 UTC 21 Aug and (c) 1200 UTC 22 Aug and for Stuttgart at (b) 1200 UTC 21 Aug, (d) 1200 UTC 22 Aug 2005, and (e) 0000 UTC 23 Aug 2005. Temperature profiles are shown by solid lines, dewpoint by dashed lines.

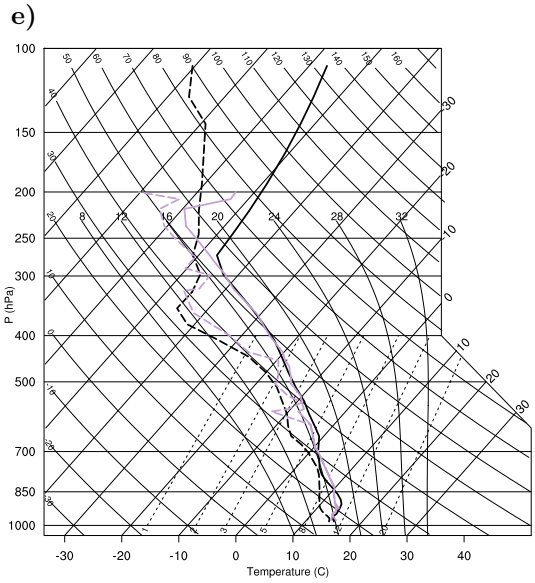

Figure 5.3: (continued)

lower levels the vertical structure of the equivalent potential temperature (θ_e) agrees with the observations, but warmer equivalent potential temperatures are produced above (see Fig. 5.4c). A maximum deviation from the sounding is reached at 4 km MSL. This results from the above shown overestimation of humidity at this level. Note that in comparison to the observation in Fig. 5.4c the ECMWF analysis reveals too low θ_e values close to the surface, which are properly captured by the reference run. All other ECMWF vertical profiles agree with both the observation and the reference run.

The wind profile at lower levels for Stuttgart at 1200 UTC 21 August (see Fig. 5.5a,b) is captured very well by the reference run. Winds are slightly weaker than at Munich with a quite uniform low-level jet of 12 m s^{-1}. Winds are easterly and turn to north closer to the surface. Observations in Fig. 5.5c exhibit less potential instability than the previous observed sounding at Munich. The lower atmosphere is nearly moist neutrally stratified and close to the surface the equivalent potential temperature is approximately 322 K, instead of roughly 327 K in Munich. The reference run shows good skill in reproducing the θ_e profile of the ECMWF analysis, which is slightly warmer than the observation close to the surface and nearly identical to the corresponding sounding for Munich.

Again a nearly moist neutral temperature profile is observed for Munich and Stuttgart at 1200 UTC 22 August (see Figs. 5.3c and 5.3d). The reference run is able to reproduce these temperature profiles. The sounding for Stuttgart (see Fig. 5.3d) exhibits a nearly perfect agreement with the moisture profile from the reference run. At this time also the observations reveal a thin dry mixed boundary layer, which is captured by the model. The moisture profile for Munich at this time (see Fig. 5.3c)

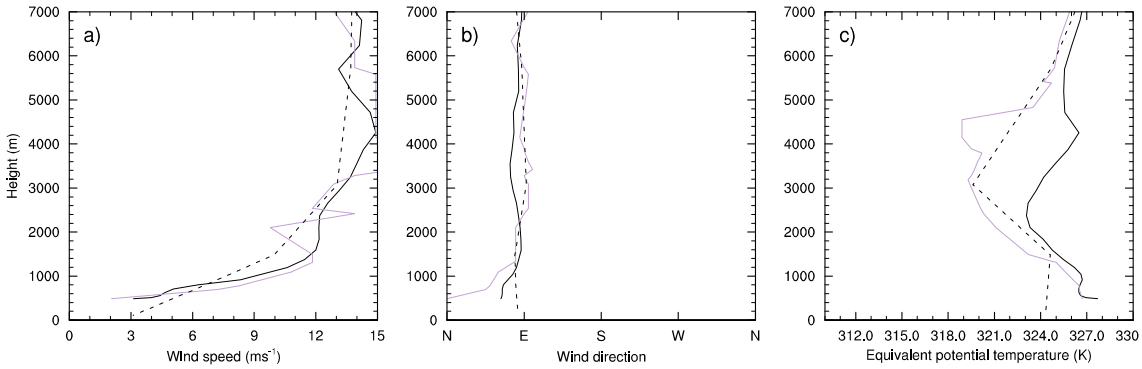

Figure 5.4: Vertical profiles from WRF (solid black), rawinsonde (gray), and ECMWF analysis (dashed black) for Munich at 1200 UTC 21 August: (a) wind speed (m s^{-1}), (b) wind direction, and (c) equivalent potential temperature (K).

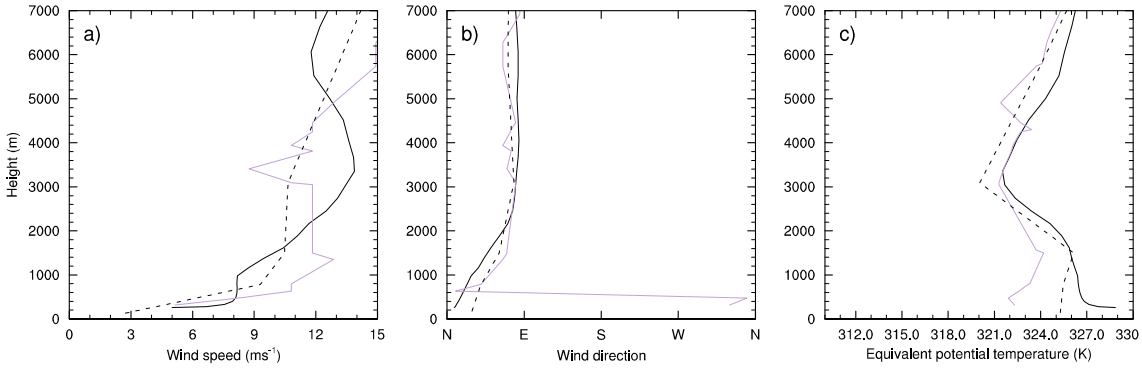

Figure 5.5: Same as Fig. 5.4, but for Stuttgart at 1200 UTC 21 August.

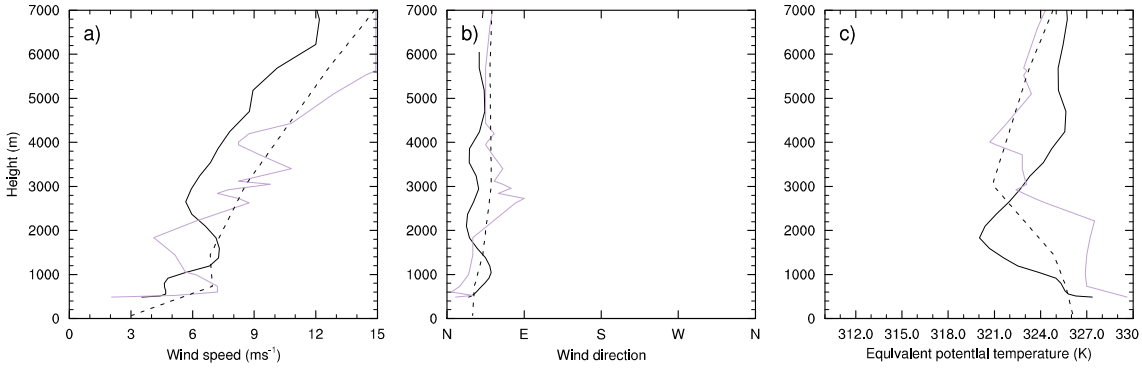

Figure 5.6: Same as Fig. 5.4, but for Munich at 1200 UTC 22 August.

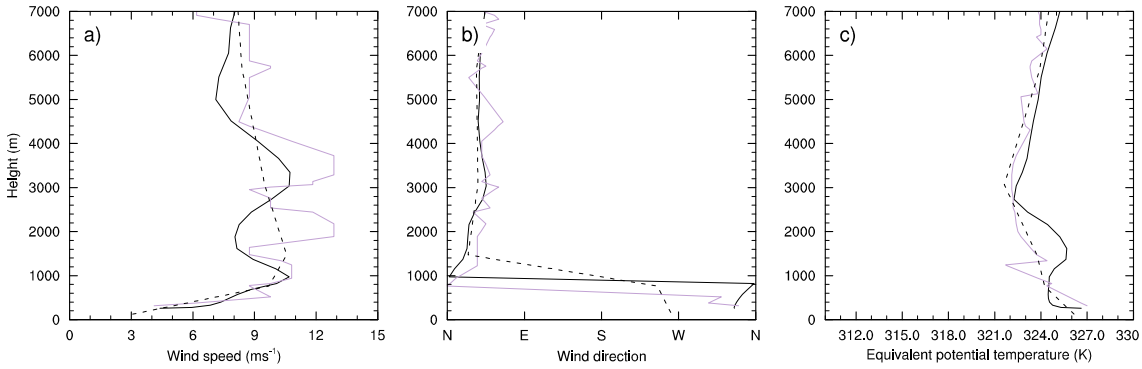

Figure 5.7: Same as Fig. 5.4, but for Stuttgart at 1200 UTC 22 August.

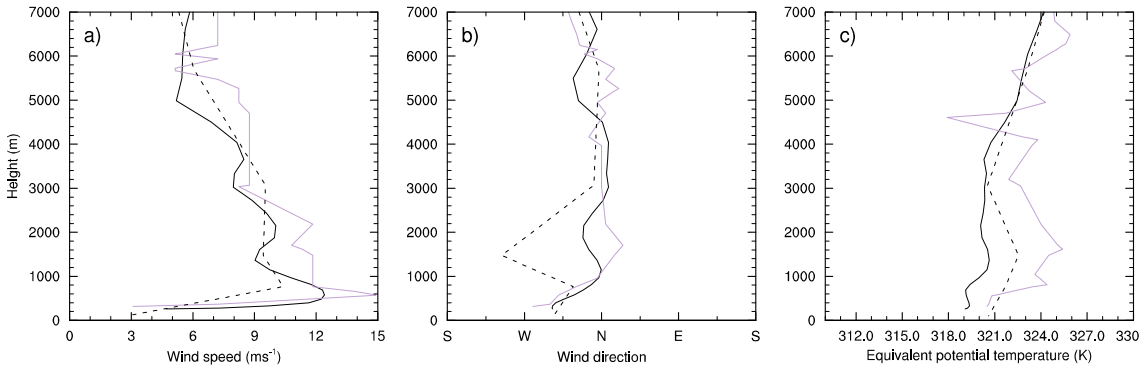

Figure 5.8: Same as Fig. 5.4, but for Stuttgart at 0000 UTC 23 August.

roughly agrees with the observed profile. In Fig. 5.6b the wind direction for Munich is northeasterly and wind speeds are less intensive than at 1200 UTC 21 August. The profile for Stuttgart (see Fig. 5.7b) reveals a predominantly northeasterly flow direction aloft, but a northwesterly low-level component. Obviously, the low-level wind direction has already turned to an Alpine normal one at Stuttgart, which is located further to the west of Munich. In Fig. 5.6c and 5.7c both vertical profiles show potential unstable layers at 1200 UTC 22 August. The θ_e inversions are less developed than at 1200 UTC 21 August, especially in Stuttgart (see Fig. 5.7c). Although the strength of the θ_e inversion is predicted satisfyingly by the reference run for Munich (see Fig. 5.6c), a very sharp θ_e gradient below 2 km MSL causes a too shallow unstable layer. The generated discrepancies in the vertical profile of θ_e are based on small variations of the low-level moisture field at this certain time (see Fig. 5.3c). For both Munich and Stuttgart the profiles of all shown parameters from the ECMWF analysis are close to and roughly follow the observed vertical profiles.

The sounding for Stuttgart at 0000 UTC 23 August is visualized by another skew-T diagram in Fig. 5.3e. An underestimation of humidity below 600 hPa of the reference run is visible. Figure 5.1b reveals that Stuttgart is located right at the western boundary of the low-level moisture flux maximum. Obviously, the WRF

reference run does not capture this strong moisture gradient at the right position. However, also the low-level moisture from the ECMWF analysis is smaller than observed. The narrow moisture band in the ECMWF analysis data is shown in Fig. 4.1d. The temperature profile, including a shallow nocturnal surface inversion is well captured. Figure 5.8a shows that the observed wind speeds appear to be nearly 15 m s^{-1}, with a maximum at 1 km MSL. The structure of the low-level jet is captured very well and the ECMWF profile is slightly improved, but the maximum velocity of the jet is underestimated by the reference simulation. Winds are northerly and turn to northwest in the lowest levels. Although the sounding shows one layer with slightly negative $\frac{\partial \theta_e}{\partial z}$, a general increase of θ_e with height is visible. Due to the underprediction of low-level moisture (see Fig. 5.3e) the reference simulation is entirely potential stable at this time. The moisture flux at the same time can be seen in Fig. 5.1b.

Note that all rawinsondes in Fig. 5.3 show a very sharp temperature inversion at the tropopause, which is smeared out by the numerical forecast. The large humidity gradient at the tropopause is not captured very well and predicted approximately 100 hPa too low.

5.2 Analysis of precipitation structures

5.2.1 3–km domain

A skillfull representation of the precipitation field in domain three, which provides the lateral boundary conditions for the one-way nested reference run in domain four, is certainly crucial for this study. Although, as will be shown later, microphysics and other factors do influence precipitation on a small high-resolution grid, the precipitation strongly depends on the moisture flux, that is provided by the coarser grid. Therefore the best possible agreement with both radar and surface observations has to be achieved before investigations in precipitation fields on a fourth high-resolution grid can be performed. In Fig. 5.9 the daily accumulated precipitation in domain three of the two-way nested model run is shown. Consult Figs. 4.3 and 4.4 in chapter 4 for a quantitative comparison with the observed daily precipitation fields. Accumulated precipitation patterns from the radar data are shown in chapter 4 as well. Because the station data is only available over the Alpine regions, the following comparison is limited to the most affected areas in Switzerland, Austria, and Germany.

On a first glance, the daily precipitation on 21 August appears in excellent agreement with the observed structures (see Fig. 5.9a). Orographic precipitation over the eastern end of the Alpine ridge is produced and both location and amount

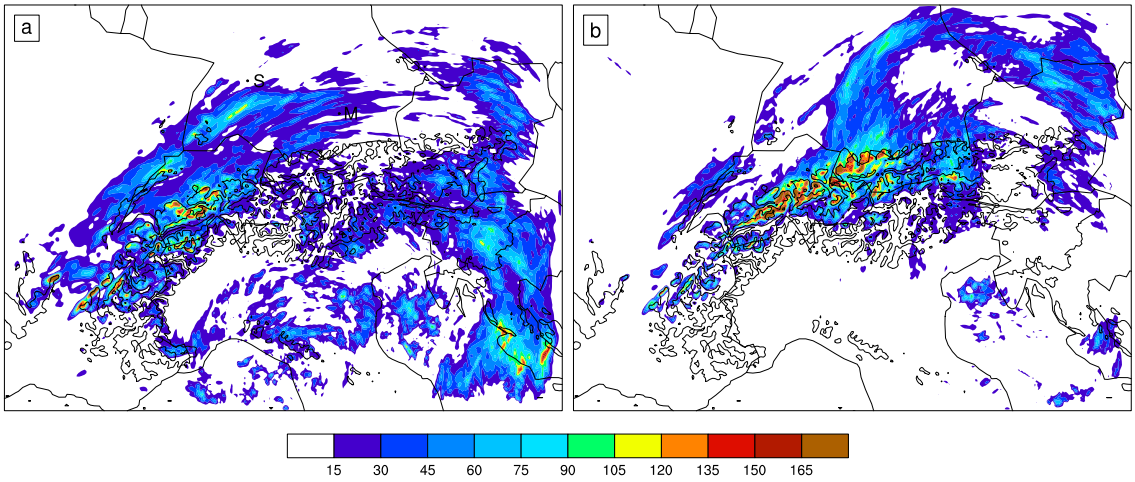

Figure 5.9: Daily accumulated precipitation (mm) in domain 3 of the WSM6*_2 run between (a) 0600 UTC 21 Aug and 0600 UTC 22 Aug and (b) 0600 UTC 22 Aug and 0600 UTC 23 Aug. Contour lines indicate orography every 1000 m. Rawinsonde locations at Munich (M) and Stuttgart (S) are indicated by black bullets.

are well captured. Well pronounced banded structures appear over the Alpine foreland in Germany, which were observed both by the radar and the automatic rain gauge measurements. Two stronger bands are visible, whereby the northern one is characterized by higher accumulated precipitation. Its structure and location is in agreement with the findings from the radar images (see Fig. 4.6b). Even the minimum of precipitation between the two most pronounced bands is well recognizeable. The origin of the precipitation band in the east of Germany is located at exactly the same position as observed by the radar (see Fig. 4.6a).

The precipitation field on 22 August (see Fig. 5.9b) shows intensive rainfall over the Swiss and Austrian northern Alpine rim. Compared to the observations (see Fig. 4.4b), too much precipitation is simulated over western Switzerland, where only little precipitation is observed. The eastern sharp edge of the observed rain band is not captured very well, as too much precipitation is produced over southeastern Bavaria and over eastern parts of Tyrol. Here the east-west precipitation gradient appears to be smoother than observed. The width of the area covered with precipitation is overestimated by the reference run, with too much heavy precipitation in the west and too much precipitation over southeastern Bavaria. Despite the above mentioned discrepancies the precipitation distribution has several features in common with the observations. Firstly, no precipitation is generated over the Swiss Alpine foreland, although the German Alpine foreland is covered with rainfall. Secondly, not only is the precipitation gradient very sharp to the north of the Swiss Alps, but even stronger to the southside of the main Alpine

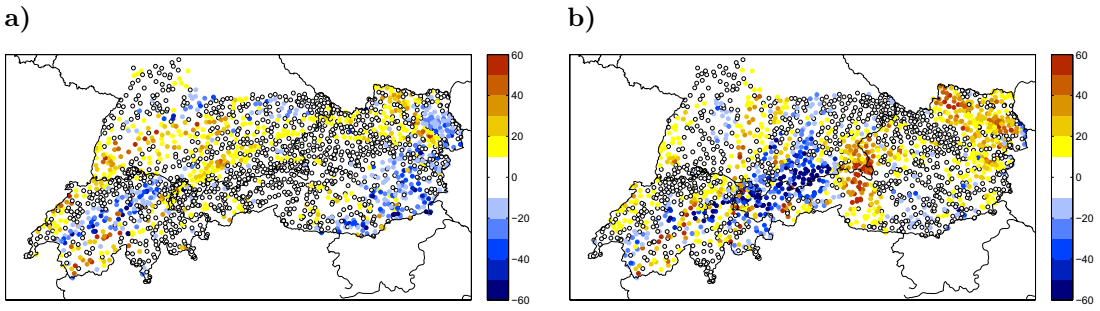

Figure 5.10: Differences between model-derived and observed daily accumulated precipitation (mm) in domain 3 of the WSM6*_2 run between (a) 0600 UTC 21 Aug and 0600 UTC 22 Aug and (b) 0600 UTC 22 Aug and 0600 UTC 23 Aug. Warm colors indicate an overprediction of precipitation and bluish colors signalize underprediction.

barrier. Only little precipitation falls over southern Switzerland. Finally, large parts of the precipitation maxima are well represented in the simulation, which shows heavy precipitation along the northern Alpine rim.

In a next step detailed intercomparison with observational data is conducted, in order to further examine the skill of the reference runs. An overview and description of the available station data is provided in section 2.2.1. Figures 5.10a,b show the difference between the simulated and observed precipitation at the locations of the observations for 21 August and 22 August, respectively. Model data has been interpolated to the station sites. Figure 5.10a shows that on one hand the model underpredicts precipitation over the northern Alpine slopes in Switzerland during 21 August. On the other hand, the reference run generates too much precipitation over the highest elevations in central Switzerland. Hence, the deviations are lower than −50 mm at some locations over the Alpine foothills, but exceed +50 mm over the higher elevations located further to the south. However, e.g., at Engelberg in central Switzerland (see Fig. 5.11b) the evolution of precipitation during 21 August is captured very well by the reference run. Figure 5.10a further reveals too heavy precipitation over southwestern Germany and the Swiss jura. Here the reference run yields an overprediction of precipitation by more than 50 mm. Figure 5.11a shows the overestimation of precipitation at Kaufbeuren in southwestern Bavaria during the 21 August. There, continuously too much precipitation is generated especially between the evening of 21 August and the morning of 22 August. In southeastern Austria an underestimation of rainfall is also recognizable. The deviations on the whole domain nearly cancel out and result in a WRF station average AVG_{sy} of 23.7 mm and a similar value for the observed station average AVG_{so}, which is 22.2 mm. The RMSE and NAE are 16.8 mm and 9.9 mm, respectively, during 21 August. Note that an overview of statistical model validation scores of the WSM6*_2 run is

given in table A.1 of the appendix.

In Fig. 5.10b the absolute deviations from the rain gauge measurements on 22 August are shown. Precipitation is overpredicted especially over eastern Tyrol, eastern Austria, and southwestern parts of Switzerland. These positive deviations confirm the above mentioned broadening of the precipitation covered Alpine area. The precipitation sequences in Engelberg/Switzerland (see Fig. 5.11b) and Berchtesgaden/Bavaria (see Fig. 5.11d) reveal the broadening of the affected precipitation area during 22 August. Especially in Berchtesgaden a significant overprediction of accumulated precipitation results from this model behavior. Additionally, the precipitation over southern Germany seems to be slightly shifted to the west, which results in a drastic underestimation of heavy precipitation over the adjacent northern Alpine foothills and an overprediction at e.g. Kaufbeuren in southwestern Bavaria (see Fig. 5.11a). The sequence of accumulated precipitation in Fraxern/Vorarlberg (see Fig. 5.11c) shows that the amount of precipitation during 22 August is captured accurately.
Apparently, the precipitation at most of the stations with large amounts of precipitation (see Fig. 4.3b) appears reduced. Hence, in terms of statistics the model has less skill on 22 August than on 21 August with a RMSE of 23.9 mm and a NAE of 15.3 mm, although the qualitative comparison of the simulated field to the observed field shows good model skill. The WRF station average AVG_{sy} of 30.6 mm is high in comparison to the observed station average AVG_{so}, which is 27.0 mm.

Although the model seems to reproduce qualitative precipitation structures and captures the locations of the precipitation maxima, both the scatter plots (see Fig. 5.10) with model deviations and the calculated statistical scores reveal that the observed amounts are not captured sufficiently accurately. The question rises, whether the applied grid-to-station interpolation is adequate for the validation of the model. Thereby model information gets lost and apparently it seems to be virtually impossible to receive an exact punctual quantitative precipitation forecast. Furthermore, the horizontal grid-point distance of 3 km might be insufficient to resolve the individual mountain ranges and valleys. Zängl (2007c) conducted simulations of heavy precipitation in the Alps and showed an improvement of model skill with higher resolutions ($\Delta x = 1$ km).

The scatter plots in Fig. 5.12 show absolute and relative differences between the simulated and observed precipitation at the locations of the observations. For both days the absolute model deviations show positive and negative values for small observed precipitation amounts and mainly an underprediction of heavy precipi-

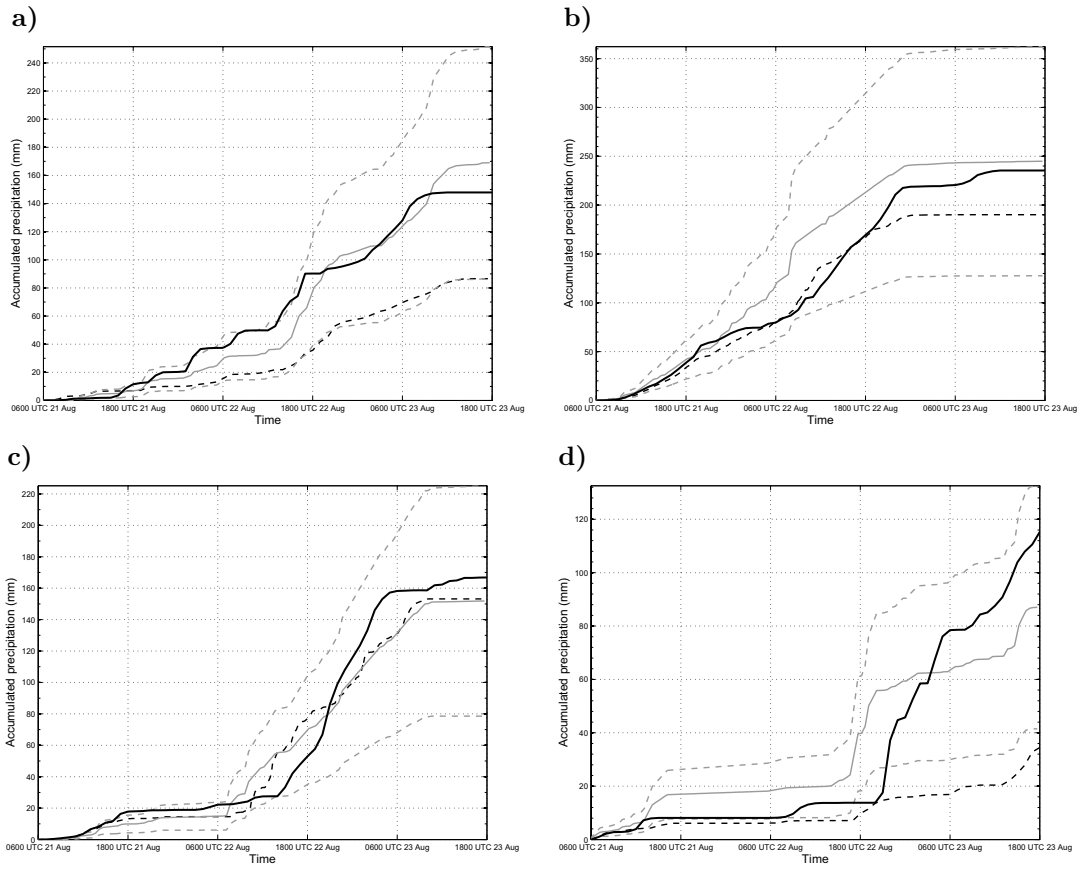

Figure 5.11: Temporal evolution of precipitation for (a) Kaufbeuren in Bavaria, (b) Engelberg in central Switzerland, (c) Fraxern in western Austria, and (d) Berchtesgaden in Bavaria. The CERAD radar measurements are drawn in gray. Gray dashed lines indicate the possible range for the calculation of accumulated precipitation and the gray solid line shows the computation by class mean values. Precipitation from automatic rain gauge measurements and from WSM6*_2 simulations are shown by the black dashed and solid lines, respectively. The locations of the stations (a),(b),(c), and (d) are indicated by the yellow, magenta, green, and blue bullets in Fig.2.2b, respectively.

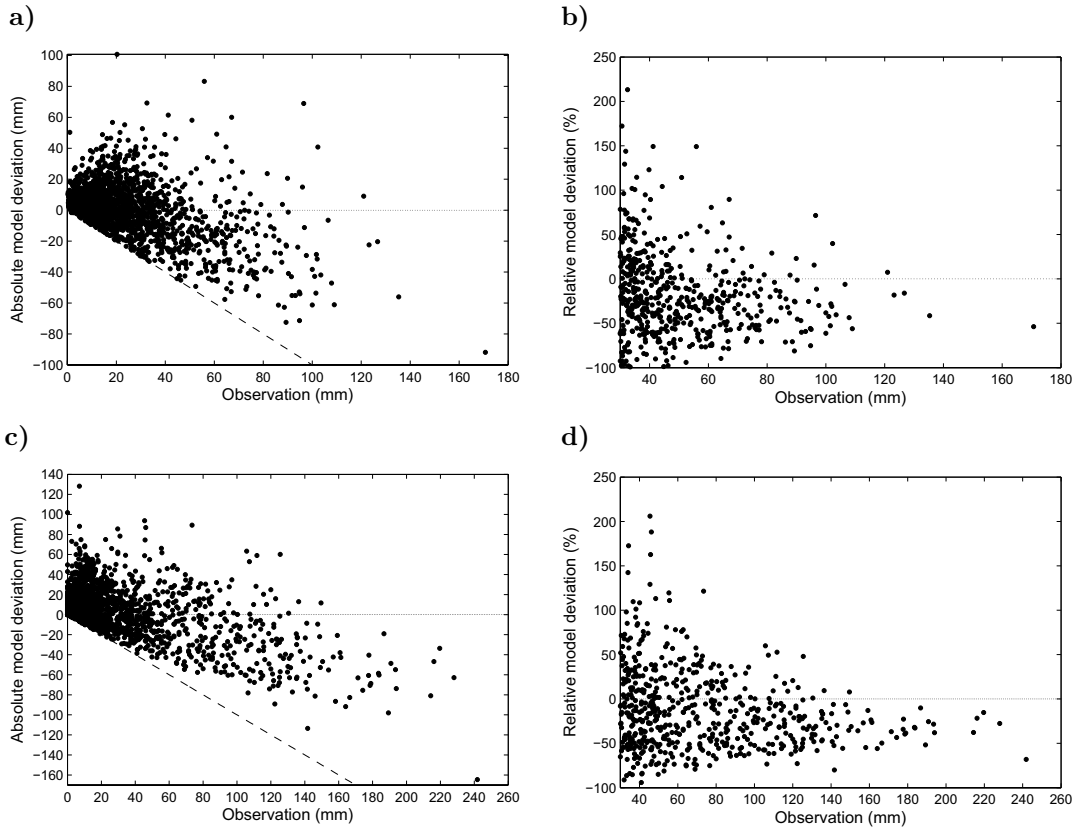

Figure 5.12: The scatter plots show (a),(c) absolute errors and (b),(d) relative errors between model-derived and observed station precipitation for the daily accumulated precipitation between (a),(b) 0600 UTC 21 Aug and 0600 UTC 22 Aug and (c),(d) 0600 UTC 22 Aug and 0600 UTC 23 Aug 2005. Note that in (b),(d) only stations with more than 30 mm observed precipitation are considered.

tation amounts. The absolute differences to the observations (see Figs. 5.12a,c) become larger with the observed precipitation amount, but the relative deviations (see Figs. 5.12b,d) show that on both days the model tends to underpredict high values of accumulated precipitation by approximately 50 %. In Figs. 5.12a,c several stations with little observed rainfall reveal no simulated precipitation at all. These are located on the long-dashed line in Figs. 5.12a,c. On the other hand, for several stations with zero observed rainfall too much precipitation is predicted. These two functionalities limit the extent of the scatter clouds. Note that in Figs. 5.12b,d a cut-off for low observed cumulative precipitation has been applied, because the relative error tends to be an order of magnitude higher for small precipitation sums.

5.2.2 1–km domain

The precipitation fields from the one-way nested REF run on the fourth, cloud-resolving domain are shown in Figs. 5.13a,b. As the coarse grid (domain three) passes only water vapor to the finer grid, i.e. hydrometeors are not included in the boundary conditions, it takes a while until precipitation has formed. Thus, a precipitation free zone occurs close to the inflow boundaries. Note that in Fig. 5.13a isolated maxima of precipitation are produced over very steep mountains close to the eastern inflow boundary. These are not produced in the corresponding two-way nested simulation, where a smooth transition from the coarse to the fine grid is ensured across four outer rows and columns of the fine grid. A gradual blending from the interpolated coarse orography to the fine orography is not applied here. Apart from that, the precipitation fields appear to be similar to the above described precipitation patterns in the 3–km domain.

Figure 5.14 shows the differences between model-derived station precipitation and the observed precipitation at the stations. Note that during both days negative deviations arise at the upstream situated domain boundaries in Figs. 5.14a,b due to the above mentioned nesting properties. This fact certainly contributes to an increase of the RMSE and NAE. Equivalent to the findings in the previous section too much precipitation is produced over the Black Forest region during 21 August, while over the Swiss Alpine foreland precipitation is underestimated. Over the German Alpine foreland in the east of the domain precipitation appears to be too high. Although the domain average AVG of 27.3 mm comes close to the observed station average AVG_{so}, which is 27.8 mm, the model-derived station average AVG_{sy} of 25.7 mm slightly underestimates the daily accumulated precipitation. The RMSE is 17.9 mm and the NAE is 8.8 mm, which is smaller than for the third domain of the reference run, because the NAE puts less weight on heavy precipitation. Note that

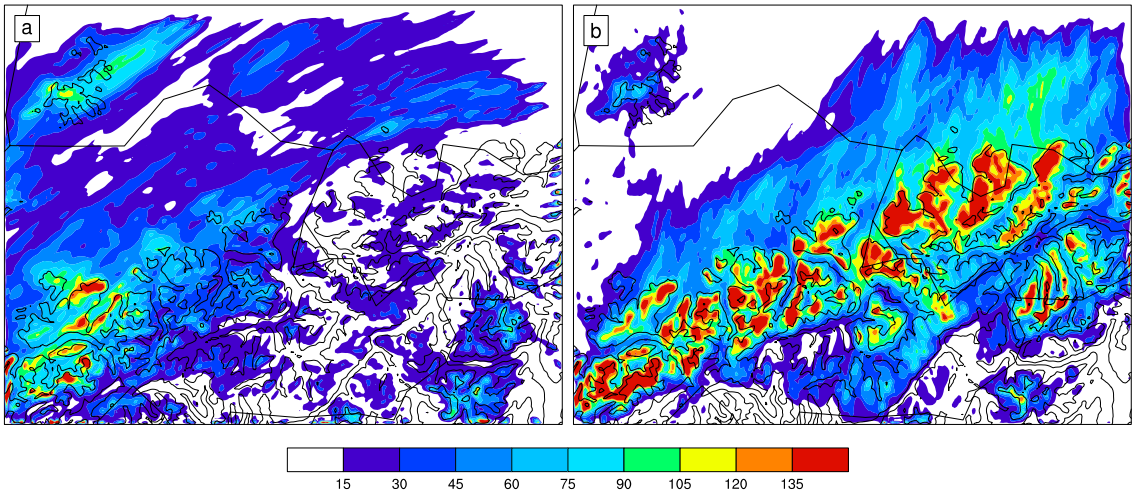

Figure 5.13: Daily accumulated precipitation (mm) in domain 4 of the one-way nested REF run between (a) 0600 UTC 21 Aug and 0600 UTC 22 Aug and (b) 0600 UTC 22 Aug and 0600 UTC 23 Aug 2005. Contour lines indicate orography every 1000 m.

both RMSE and NAE are slightly higher than for the corresponding two-way nested simulation (see Table A) on domain four, because of the decrease of precipitation close to the domain boundaries.

During 22 August most of the stations which are placed in the center of the Alps, gain not enough precipitation in the reference run. During this time the Swiss Alpine foreland receives too much rainfall. Both, the domain average AVG (47.4 mm) and the model-derived station average AVG_{sy} (49.7 mm) underpredict the observed station average AVG_{so} of 57.6 mm. The RMSE is relatively high with 31.6 mm and the NAE is 17.2 mm. A corresponding two-way nested WSM6*_2_4 simulation on domain 4 produces slightly smaller error scores than the one-way nested forecast (see Table A).

Besides the above mentioned discrepancies, the reference runs have sufficient value for further investigations and sensitivity tests. Moreover, this microphysical study is not primarily aimed at an improvement of the quantitative precipitation forecast of the reference run.

5.3 Characteristics of period 1: 1200 UTC 21 August – 00 UTC 22 August 2005

Figures 5.15a,b show the total precipitation mixing ratio in 3 km above mean sea level (MSL) and the squared moist Brunt-Väisälä frequency at 2 km MSL from

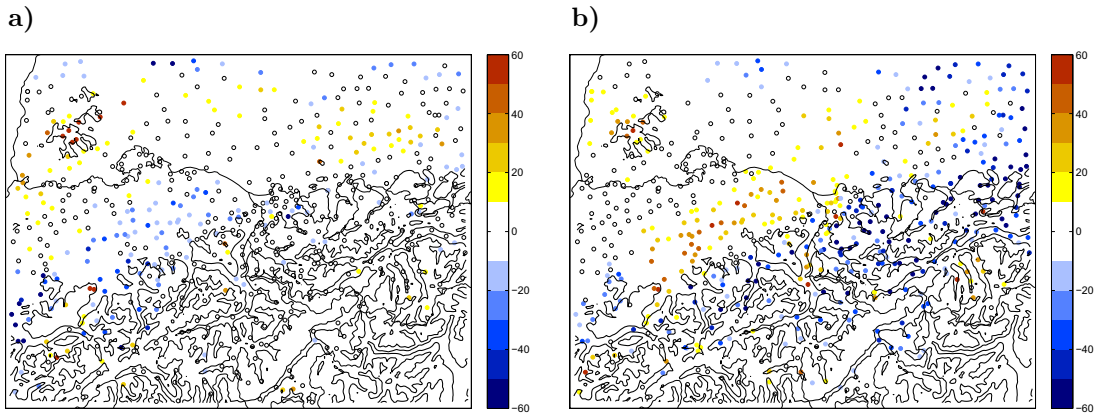

Figure 5.14: Differences between model-derived and observed daily accumulated precipitation (mm) in domain 4 of the one-way nested REF run between (a) 0600 UTC 21 Aug and 0600 UTC 22 Aug and (b) 0600 UTC 22 Aug and 0600 UTC 23 Aug 2005. Warm colors indicate an overprediction of precipitation and bluish colors signalize underprediction. Contour lines indicate orography every 1000 m.

the REF run at 1500 UTC and 1700 UTC 21 August, respectively. In Fig. 5.15a convective cells are randomly distributed over the Alpine foreland. Embedded into a moist unstable stratified air mass these disorganized cells propagate to the southwest. They are already present upstream of the main Alpine barrier. Note that outside of the unstable regions no convection is generated. Reasons for the triggering of convection ahead of the Alpine elevations can be either a very low convective inhibition due to the moist static instability or a prevailing large-scale lifting due to the cyclonic synoptic situation (see Fig. 4.1). Until 1700 UTC 21 August (see Fig. 5.15b) the area, which is affected by shallow cellular convection becomes more narrow and is located slightly closer to the main Alpine rim. The unstable stratified air mass has now further proceeded into the domain. Although the region with cellular precipitation appears to be quite narrow, organized structures of banded features are not generated. Such stationary banded structures of roll-like convection are not observed in this simulation. Also stationary precipitation structures are not produced. The here described convective situation is similar to an event with embedded cellular convection over the Coastal Range in western Oregon on 12 October 2003, described in Kirshbaum and Durran (2005b). Equivalent to the atmospheric conditions in his case, here a lack of vertical windshear in lower levels causes a primarily cellular convective type. The vertical profiles shown in Fig. 5.5 reveal a rather consistent easterly wind in the lower levels with a uniform wind speed of approximately 12 m s^{-1}. Furthermore, in this case the presence of cellular convection upstream of the Alpine crests prohibits the formation of organized banded features over the main Alpine barrier. Note that in section 4.3 banded convective precipitation patterns were clearly visible

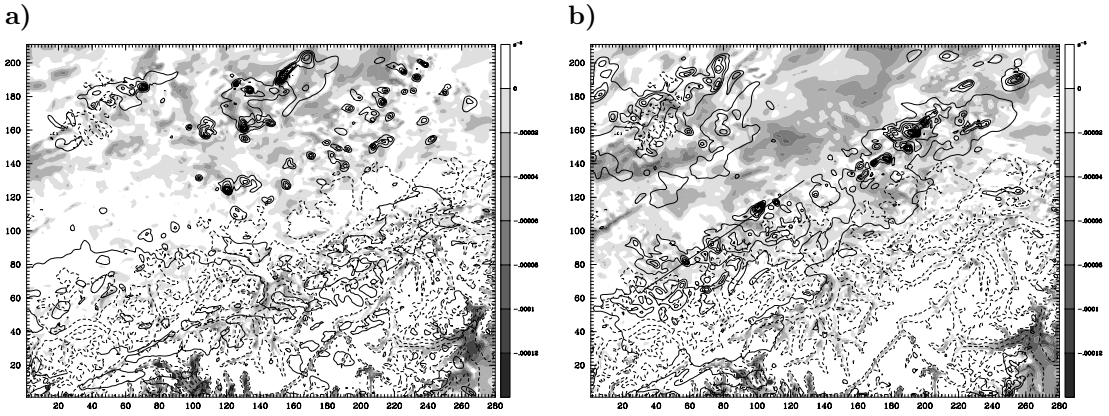

Figure 5.15: Horizontal cross-sections of the squared moist Brunt-Väisälä frequency (shading increment 2×10^5 s^{-2}, see gray scale key) at 2 km MSL; solid contours show the total precipitation hydrometeor mixing ratio (g kg^{-1}) at 3 km MSL from the REF run at (a) 1500 UTC 21 Aug and (b) 1700 UTC 21 Aug. Dashed contour lines indicate orography every 1000 m.

from radar images over the German Alpine foreland further to the east (outside of this domain). The vertical profile in Munich, which is located further to the east, reveals a stronger vertical wind shear in the lower levels (see Fig. 5.4). The wind speed continuously increases from 2 m s^{-1} near the surface to 15 m s^{-1} at 3 km MSL. Thereby the wind direction turns from north to east. Besides a low-level wind shear and the atmospheric moist static instability, small-scale topographic features might also contribute to the triggering of the banded convection.

A vertical cross-section through the highly moist unstable air mass is shown in Fig. 5.16. The cross-section is aligned parallel to the northeasterly flow direction (see Fig. 5.15b). Figure 5.16a shows rapid vertical updrafts rising in a highly potentially unstable stratified environment. The θ_e inversion is approximately 6 K. The convective updrafts exceed 5 m s^{-1}. Next to the locations with rising motions downward directed sinking motions are clearly visible. Figure 5.16b shows that downdraft regions correspond to cloud free areas and proves the presence of a continuous moist unstable stratified layer that reaches up to circa 2.8 km MSL. In the convective updrafts localized heavy precipitation occurs, while surrounding regions receive significantly less precipitation. Close to the melting line well pronounced graupel clouds are generated in the regions with updrafts. An upper ice cloud is discernable. In contrast to the graupel amount, the snow mass is inconsiderably small.

Period 1, as has been shown above, is characterized by shallow embedded cellular convection, which produces precipitation already upstream of the main Alpine

rim.

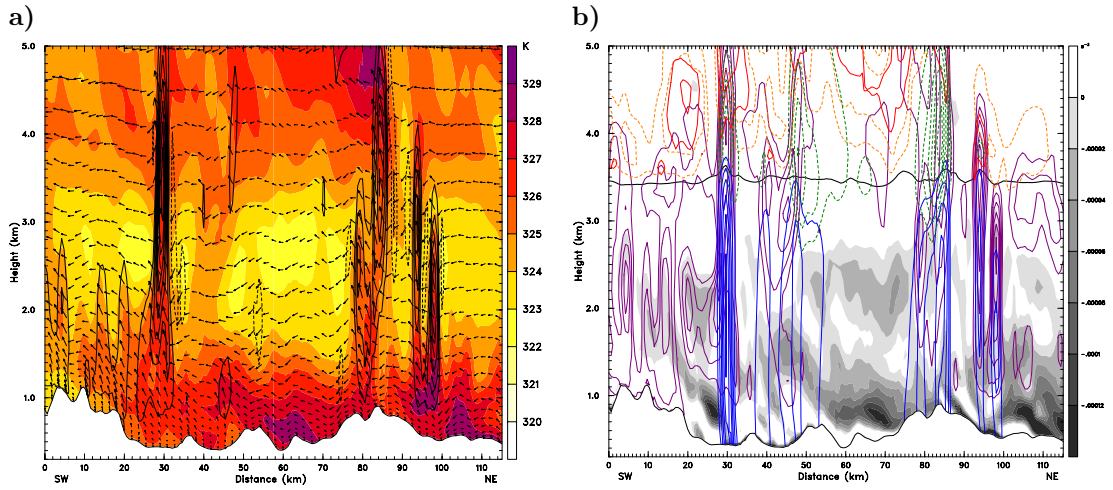

Figure 5.16: Vertical cross-sections of the REF simulation at 1700 UTC 21 Aug along the line indicated in Fig. 5.15b. (a) Wind vectors showing the components along the cross-section, equivalent potential temperature (shading increment 1 K, see color key), and vertical wind speed (contour interval 0.75 m s^{-1}, negative values dashed, no zero line). (b) Squared moist Brunt-Väisälä frequency (shading increment 2×10^5 s^{-2}, see gray scale key), mixing ratios of rain (solid blue lines, contour interval 0.4 g kg^{-1}), cloud water (solid violet lines, contour interval 0.2 g kg^{-1}), ice (dashed orange lines, contour interval 0.04 g kg^{-1}), snow (solid red lines, contour interval 0.04 g kg^{-1}), graupel (dashed green lines, contour interval 0.4 g kg^{-1}), and zero degree level (bold black line).

5.4 Characteristics of period 2: 1800 UTC 22 August – 06 UTC 23 August 2005

Horizontal cross-sections of the total precipitation mixing ratio in 3 km MSL and the squared moist Brunt-Väisälä frequency at 2 km MSL from the REF simulation at 1930 UTC 22 August and 0200 UTC 23 August are shown in Fig. 5.17. The moist static instability at 1930 UTC 22 August (see Fig. 5.17a), which is indicated by negative N_m^2, is less pronounced than during the previous period. Cellular structures of the precipitation mixing ratio are still present in the northeast of the domain. There, embedded cellular structures are triggered already upstream of the main Alpine barrier. Also over Switzerland the moist static stability is higher than during period 1, especially close to the Alpine crests. As a consequence no convective rainfall is generated upstream of and over the Swiss Alps (see also Fig. 5.19b). Precipitation is more bound to the higher elevations in the central and the western parts of the domain. In Fig. 5.17a

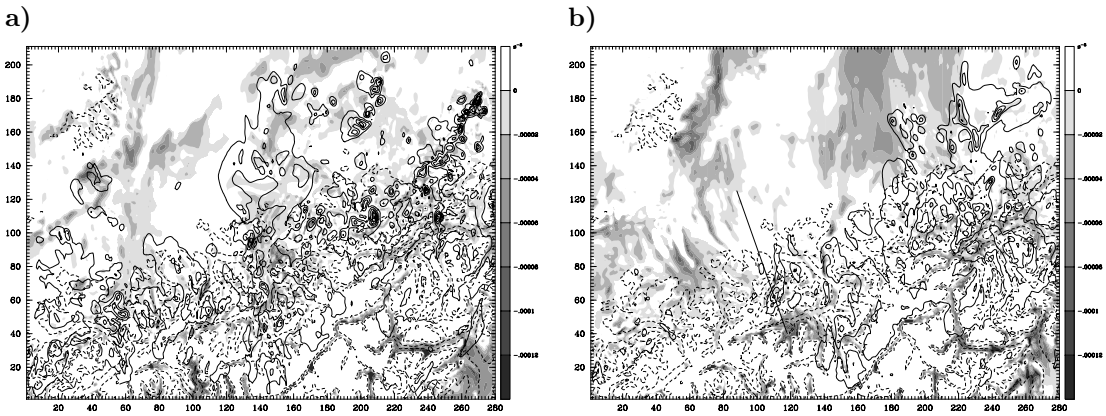

Figure 5.17: Horizontal cross-sections of the squared moist Brunt-Väisälä frequency (shading increment 2×10^5 s^{-2}, see gray scale key) at 2 km MSL; solid contours show the total precipitation hydrometeor mixing ratio (g kg^{-1}) at 3 km MSL from the reference run at (a) 1930 UTC 22 Aug and (b) 0200 UTC 23 Aug. Dashed contour lines indicate orography every 1000 m.

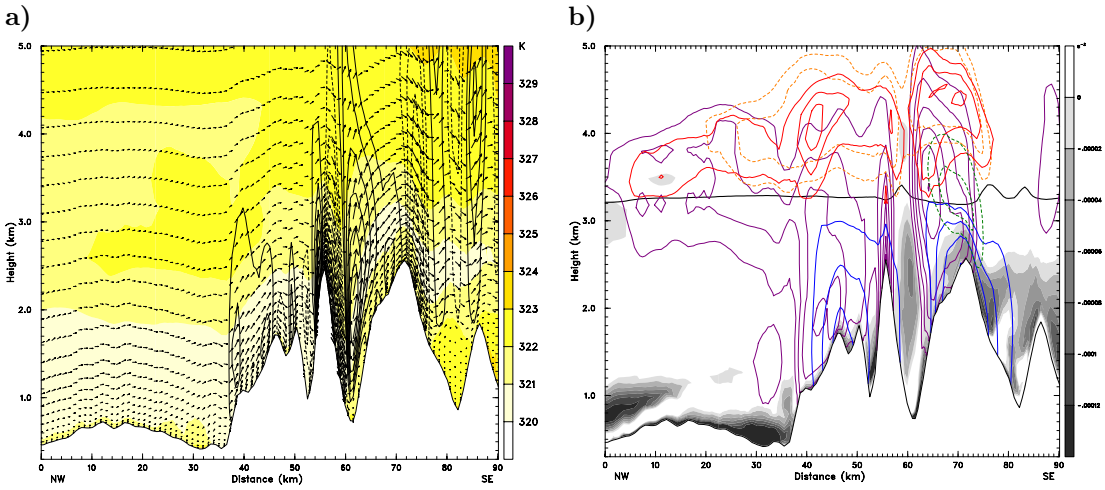

Figure 5.18: As in Fig. 5.16, but at 23 UTC 22 August and smaller contour interval for mixing ratio of rain (solid blue lines, contour interval 0.2 g kg^{-1}). The vertical cross-section is indicated in Fig. 5.17b.

the decrease of precipitation over Switzerland is already discernable, while intensive rainfall still occurs over western Austria. In the morning of 23 August (see Fig. 5.17b) precipitation is completely confined to the higher elevations over central Switzerland, because of a solely stable stratified type of orographic precipitation. Over western Austria randomly organized cellular features are still present in the moist unstably stratified air mass slightly upstream of the Alpine rim.

A vertical cross-section of θ_e over Switzerland in Fig. 5.18a shows almost moist neutral conditions at lower levels, but potentially stable conditions above. The maxima and minima of the vertical velocity field are totally restricted to the

topography, and vertical updrafts due to moist convection are not observed. Strong randomly distributed vertical updrafts are not possible under such atmospheric conditions. Moist stable conditions are dominating in Fig. 5.18b and negative values of N_m^2 can only be found close to the surface. Additionally, Fig. 5.18b reveals that precipitation only occurs over the main Alpine rim, but not over the Alpine foreland. Mostly stable stratified cap clouds are found over the mountain crests. A pronounced graupel cloud with a maximum mixing ratio of 0.8 g kg^{-1} is included in the precipitation process over the main ridge and the advection of graupel into the lee of the mountain is clearly recognizeable. Again, moderate ice amounts with a highest mixing ratio of 0.08 g kg^{-1} are present above the melting line and only inconsiderably small amounts of snow are generated. Although moderate solid precipitation is produced on some mountain tops, in this cross-section graupel is not falling to the ground.

Orographic precipitation during period 2, as described above, is dominated by orographic lifting of the weakly-stable stratified air mass. Nevertheless, moist unstable stratified regions persist to the east of the domain, where still convective precipitation is randomly triggered upstream of the main Alpine elevations. The 12-hour accumulated precipitation for period 2 is shown in Fig. 5.19b, which confirms the limitation of precipitation to the main Alpine crests over Switzerland and the convectively enhanced precipitation over the eastern parts of the domain. The 12-hour accumulated precipitation during period 1 is visualized in Fig. 5.19a, which again reveals the precipitation ahead of the main Alpine elevations. The maximum is located over the northern Alpine slopes in central Switzerland.

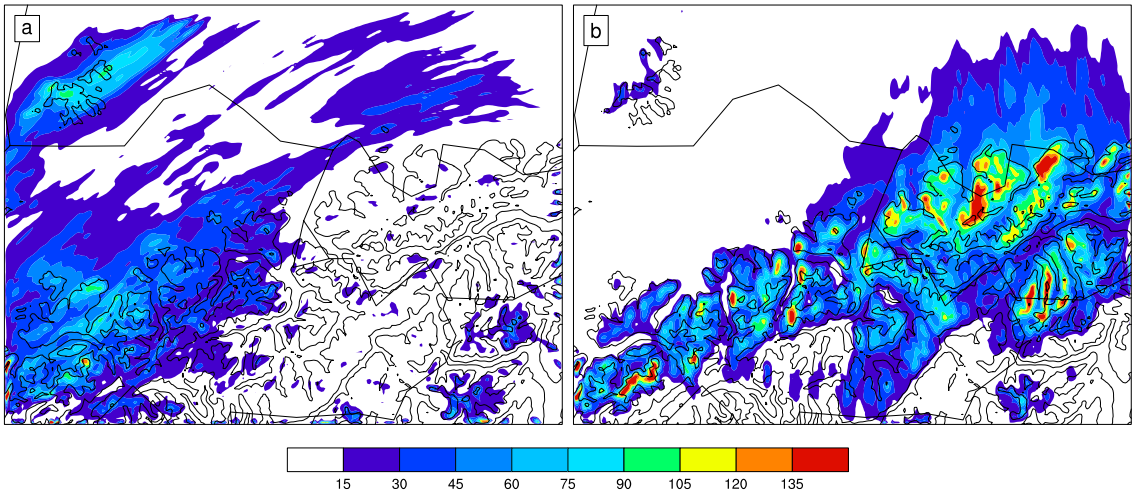

Figure 5.19: Accumulated precipitation (mm) in domain 4 of the one-way nested REF reference run during (a) period 1 (1200 UTC 21 Aug – 0000 UTC 22 Aug) and (b) period 2 (1800 UTC 22 Aug – 0600 UTC 23 Aug). Contour lines indicate orography every 1000 m.

Chapter 6

The sensitivity to microphysics parameterizations

Numerical sensitivity simulations are performed to investigate the importance of microphysics parameterizations on orographic precipitation. The underlying microphysical processes of precipitation formation are determined and the results of each scheme are compared to the reference simulation (REF), which uses the WRF single-moment bulk microphysics scheme WSM6* (see chapter 5). Special attention is given to the influence of each scheme during two certain periods, which are characterized by embedded cellular convection and stable upslope ascent, respectively. A description of both periods has been included in the analysis and validation of the REF run in the previous chapter. In sections 6.1, 6.2, and 6.3 the modifications due to different microphysics in the Kessler, WSM5*, and Thompson scheme, respectively, are presented and findings from further sensitivity experiments are shown in section 6.4.

6.1 "Kessler" run

The Kessler (1969) scheme, which is a very simple "warm rain" scheme (see section 3.4.1), is tested and compared against the reference run (REF) and the observational rain gauge data. One could hypothesize that the influence of ice microphysical processes on the production of precipitation is negligible, when the melting line is located far above the highest peaks. In the August 2005 case the melting line is situated at about 3.2 km MSL (see Fig. 5.16), which is still above the highest Alpine mountain tops. Thus, this case seems to be an appropriate test case for the "warm rain" scheme. The simulation will be abbreviated as KES in the following.

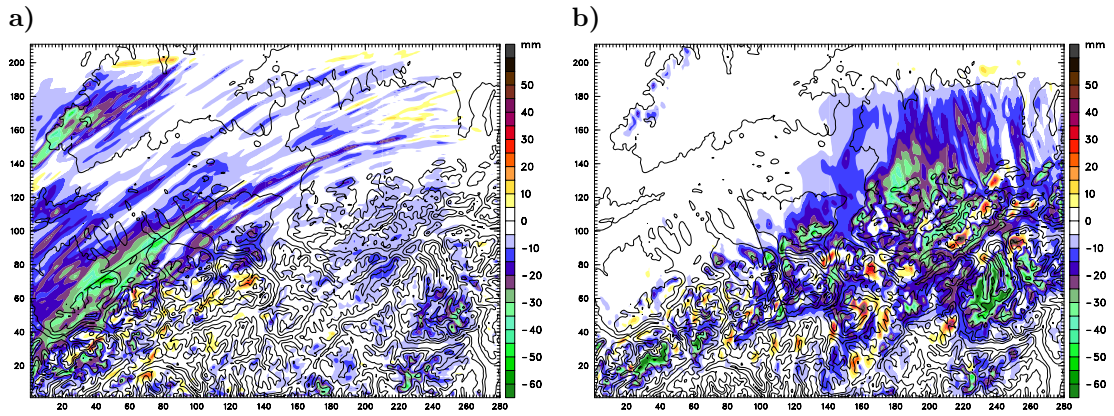

Figure 6.1: Differences in 12-hour accumulated precipitation (KES − REF) in mm for (a) period 1 and (b) period 2. Cold colors indicate less precipitation predicted by the Kessler scheme. Contour lines indicate orography every 600 m.

Figure 6.1 shows the difference in accumulated precipitation between the KES simulation and the REF run for both 12 hour periods. During period 1 (see Fig. 6.1a) the strongest negative deviations appear right at the location of the maximum accumulated precipitation over central Switzerland. Here the differences arising from the Kessler parameterization are below −50 mm. Another negative extreme of the deviation appears over the Black Forest mountains in southwestern Germany. Besides these extreme negative deviations, tracks produced by convective elements in the REF simulation, which are missing in the KES run, are well noticeable by the northeast-southwest orientated bands of moderate negative deviations. They indicate the inability of the Kessler scheme to reproduce the embedded convection as simulated by the reference scheme over the Alpine foreland. As positive deviations during period 1 (see Fig. 6.1a) only appear at isolated ridges in the center of the Alpine barrier and close to the entrance regions, the area-averaged precipitation AVG of daily precipitation in domain 4 is tremendously decreased by 39.6 % from 27.3 to 16.5 mm (see also Table A.1 in appendix). Corresponding to this decrease in precipitation the RMSE and NAE rise from 17.9 mm and 8.8 mm to 24.2 mm and 17.6 mm, respectively. The difference between the station averages (AVG_{so} − AVG_{sy}) for 21 August is increased to 12.5 mm, with the WRF model underestimating the precipitation at the locations of the stations.

Figure 6.2a reveals that the Kessler parameterization reduces the vertical updrafts in embedded cellular convection. In comparison to the REF run (see Fig. 5.16a) Fig. 6.2a shows significantly less convective behavior and lower vertical velocities in 3-4 km MSL, where randomly distributed rapid updrafts are produced in the REF run. The air mass upstream of the left hill in Fig. 6.2a possesses a less pronounced equivalent potential temperature inversion than shown in Fig. 5.16a. Slightly colder θ_e values are located at the foothills of this mountain in the KES

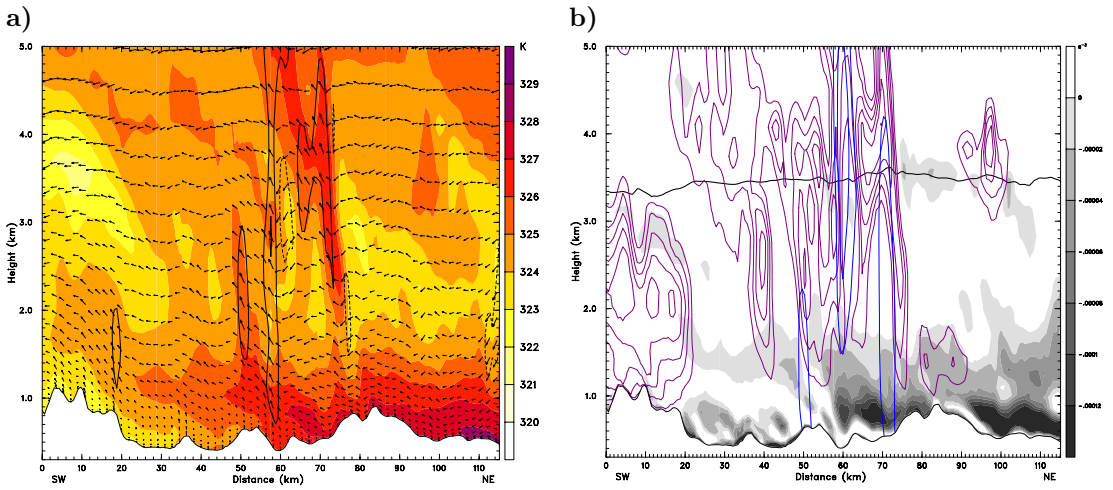

Figure 6.2: As in Fig. 5.16, but for the KES simulation. The vertical cross-section is indicated in Fig. 6.1a.

simulation and add further potential stability, at least to lower levels. In comparison to the REF run, the advection of the low-level warm θ_e values seems to be delayed, but analysis at later dates reveals that the strength of the potential instability of the REF run is never achieved, leading to a continuous reduction of vertical updrafts.

In the Kessler scheme only water vapor, cloud water and rain are considered and no mixed or ice phase categories are present (see Fig. 6.2b). In comparison to the REF run the rain mixing ratio decreases by 1.6 g kg^{-1} in the updraft in the middle of the cross-section. A comparison of the depth of the layer with negative squared Brunt-Väisälä frequency in Figs. 6.2b and 5.16b proves the decrease of moist static instability. Above 1.8 km MSL the layer appears less continuous and the moist static instability in the left part of the cross-section, where most of the rain is produced in the REF run, is decreased.

One reason for the damping of vertical velocities, which results in less precipitation fallout over the Alpine foreland and the northern Alpine ridges, is the missing latent heat release due to freezing processes. Additional latent heating, produced by water phase changes from liquid to solid, possibly strengthens vertical updrafts in embedded convection, that reaches above the melting line. This result is consistent with previous studies (e.g., Levi and Saluzzi 1996), which showed that energy released by the freezing of cloud droplets strengthens convective updraft in weak static unstable atmospheric conditions. On the other hand also the consumption of energy during melting processes can reinforce small-scale horizontal discrepancies of the vertical velocity (Szyrmer and Zawazki 1999; Unterstrasser and Zängl 2006).

During period 2 (see Fig. 6.1b) the differences are again negative in most parts

of the domain. Areas with extreme reduction of more than 60 mm are located over high mountains in the southeast and southwest of the domain, regions where the REF run produces significant amounts of solid precipitation. A larger area of negative differences also appears over western Austria and eastern Switzerland, where convective rainfall in the REF run is still enhancing precipitation upstream of the main Alpine crest during the afternoon. Equivalent to the findings for 21 August, the daily area-averaged precipitation AVG of domain 4 significantly decreases from 47.4 mm to 34.5 mm by 27.2 %. Both RMSE and NAE increase by approximately 8.5 mm (see Table A.2 in appendix). The WRF station average AVG_{sy} is also decreased by 14 mm, now even further underestimating the observed rainfall.

Further analysis shows that during period 2 (see Fig. 6.1b), which was primarily dominated by stable orographic precipitation, the KES simulation does not only underpredict orographic precipitation over high mountains that are embedded in the main Alpine ridge, but also over smaller mountain peaks with crests below 1.8 km MSL. In Fig. 6.1b the magnitudes of the reduction of the precipitation by the KES run are larger than 15 mm over the relatively smooth hills of the southern Black Forest in the northwest of the domain and reductions of more than approximately 20 mm are produced over smaller elevations belonging to the northern Alpine foothills in the center of the domain. This reduction of precipitation over the windward slopes of smaller northern Alpine mountains does not result from the exclusion of ice phase processes, e.g. melting of graupel or snow, because the maxima of the graupel mixing ratios in the REF simulation are located over the summits and the lee sides of the ridges (see Fig. 5.18b). A more important impact on warm rain production has the autoconversion of cloud water to rain drops. Figure 3.1 in section 3.4.1 shows assumptions for its different parameterizations. As already mentioned, within the WSM6* a smaller critical cloud water mixing ratio for autoconversion is assumed and, if the cloud water mixing ratio exceeds its critical value, the conversion rates are approximately twice as high as within the Kessler scheme. Thus, rain production in the KES run sets in only for high amounts of cloud water (critical value is 1 g kg^{-1}) and works less efficient. Furthermore, the growth rate of rain by accretion of cloud water, as shown in Fig. 3.1 in section 3.4.1, is assumed to be smaller than in the WSM6* scheme.

Only small isolated peaks of positive deviations appear at scattered locations (see Fig. 6.1b) preferentially in the right half of the domain and result, at least to some degree, from different locations of convective releases. Isolated peaks of increased precipitation also occur at locations where the small-scale distribution of precipitation is slightly modified during this period of stably stratified flow. The KES run seems to produce more precipitation over some of the high mountain peaks, but

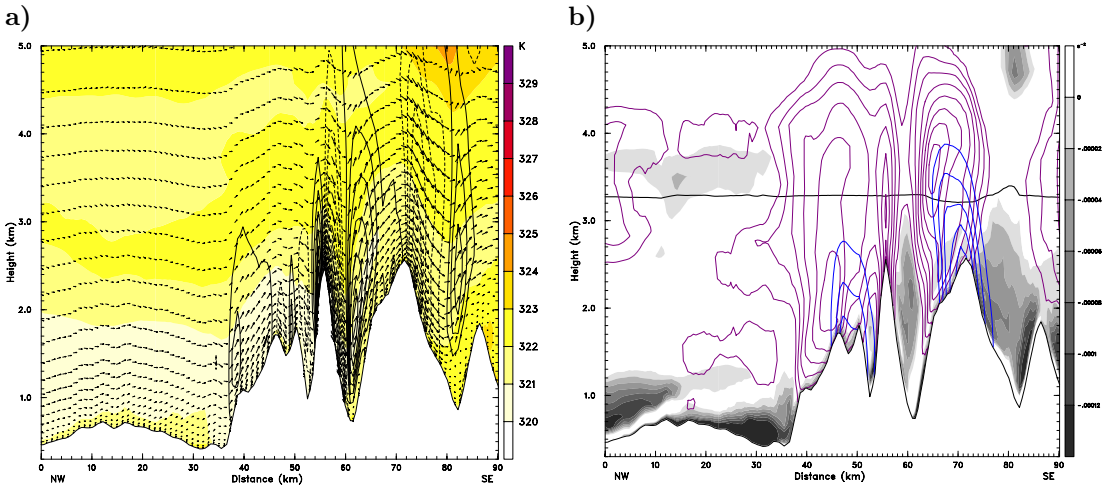

Figure 6.3: As in Fig. 5.18, but for the KES simulation. The vertical cross-section is indicated by the solid black line in Fig. 6.1b.

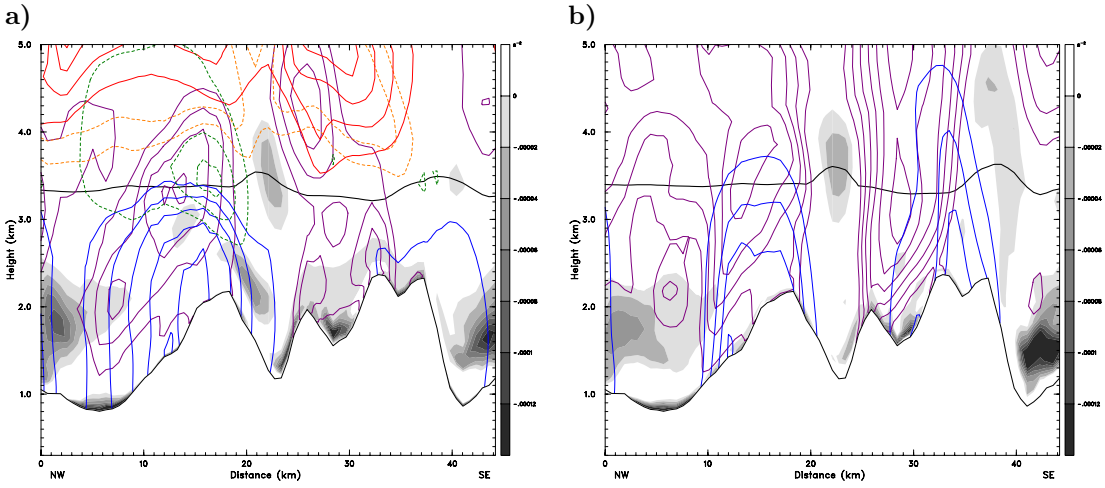

Figure 6.4: Hydrometeor mixing ratios and moist squared Brunt-Väisälä frequency as in Fig. 5.18b, but (a) for the REF simulation at 2230 UTC 22 Aug and (b) for the KES simulation at 2230 UTC 22 Aug. The vertical cross-section is indicated by the dashed black line in Fig. 6.1b.

less precipitation is formed slightly upstream and downstream of these peaks (see Fig. 6.1b). Figure 6.3a shows, equivalent to the cross-section of the REF run in Fig. 5.18a, that the atmosphere is potentially stable stratified. Figure 6.3a reveals no significant differences to the REF simulation, both in the temperature and the wind field. However, the hydrometeor distribution (see Fig. 6.3b) over complex terrain is different. The REF run (see Fig. 5.18b), which includes ice and mixed phase hydrometeors, produces more widespread rainfall over the high mountain crests, whereas in Fig. 6.3b an abrupt and localized rain production over the mountain peaks is identifiable. In the KES simulation both the entrance and exit regions of the rain covered area are located slightly closer to the mountain top. The REF simulation in Fig. 5.18b shows a pronounced non-precipitating graupel cloud over the right mountain, which causes more precipitation due to melting over the lee side of the ridge. Although the precipitation over this right mountain appears broader in the REF simulation, the KES simulation predicts the maximum rain mixing ratio over this ridge by 0.4 g kg^{-1} higher than the REF simulation, because of less total precipitating water content over the upstream located ridge.

Figures 6.4a,b demonstrate another example for the modifications of the small-scale precipitation structures. The precipitation pattern in the cross-section of the REF run appears to be broader and rain is carried further downstream of the first peak. Again a graupel cloud aloft is recognizable. A more strictly defined and 0.4 g kg^{-1} higher maximum of the rain mixing ratio is visible over the peak at the right end of the cross-section in the KES simulation. As a consequence horizontal rain mixing ratio gradients are stronger over both ridges in the KES simulation.

The above mentioned differences in small-scale precipitation distribution are a consequence of the higher critical cloud mixing ratio for autoconversion, which causes both the onset of rain production over the upslope and the exit of the precipitation region over the lee side to be closer located to the mountain top. Furthermore, the lower terminal velocity of graupel causes increased precipitation over the lee side of the ridge where the downstream advected graupel cloud melts.

6.2 “WSM5*” run

The WRF single-moment bulk microphysical scheme with five prognostic hydrometeor species (WSM5*), as introduced in section 3.4.2, is compared to the reference run (REF) and observations. At first, differences to the precipitation field of the REF run during period 1 are analyzed. Figure 6.5a shows that in most parts of the domain the modifications are not significant. Both negative and positive deviations appear over the northern Alpine flanks, where the locations of convective precipitation are slightly out of phase. The modification of the positions of convective

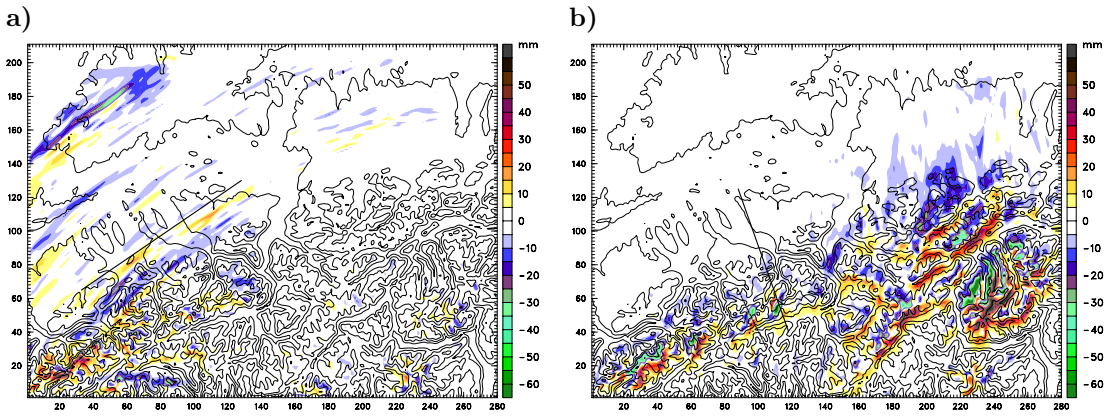

Figure 6.5: Differences in 12-hour accumulated precipitation (WSM5* − REF) in mm for (a) period 1 and (b) period 2. Contour lines indicate orography every 600 m.

precipitation causes a banded structure of positive and negative deviations. The precipitation pattern over the Alpine foreland undergos only inconsiderably small modifications. An area with negative deviations appears over the southern Black Forest region, where convective precipitation decreased. The WRF area average of daily accumulated precipitation decreases by only 3 % in terms of the domain average and by 2 % in terms of the station average. The validation of the simulation with observations reveals a slightly improved model performance. In particular the RMSE and NAE decrease by 0.5 and 0.3 mm, respectively (see Table A.1 in appendix). This follows from the reduction of convective precipitation over the Black Forest region in the northwestern part of the domain, which is slightly overestimated by the REF run.

Figure 6.6a shows cross-sections of θ_e and the vertical velocity over the Alpine foreland. A comparison to Fig. 5.16a shows, that the structure of potential instability is the same as in the REF simulation and rapid vertical updrafts grow from a thick moist unstable stratified layer. The vertical velocity field in Fig. 6.6a confirms the modification of the locations with maximum updrafts and verifies the presence of embedded cellular convection. Comparable amounts of snow in the WSM5* run (see Fig. 6.6b) and graupel in the REF run can be observed, but the maxima of snow mixing ratio in the WSM5* tend to occur at higher altitudes, which might simply result from the comparatively smaller fall speed of snow (see Fig. 3.2).

For a better illustration, horizontal distributions of the snow and graupel mixing ratios are examined. A detailed comparison to the REF run at 1800 UTC 21 August is given in Fig. 6.7, which shows the sum of the graupel and the snow mixing ratios for horizontal cross-sections located at 3 and 4 km MSL, respectively. As already shown above, the REF run generates only insignificant amounts of snow, thus contributing inconsiderably small amounts to the shown mixed-phase hydrometeor sums. Equivalent to the findings in Fig. 6.6b, the maximum mixing ratios in the

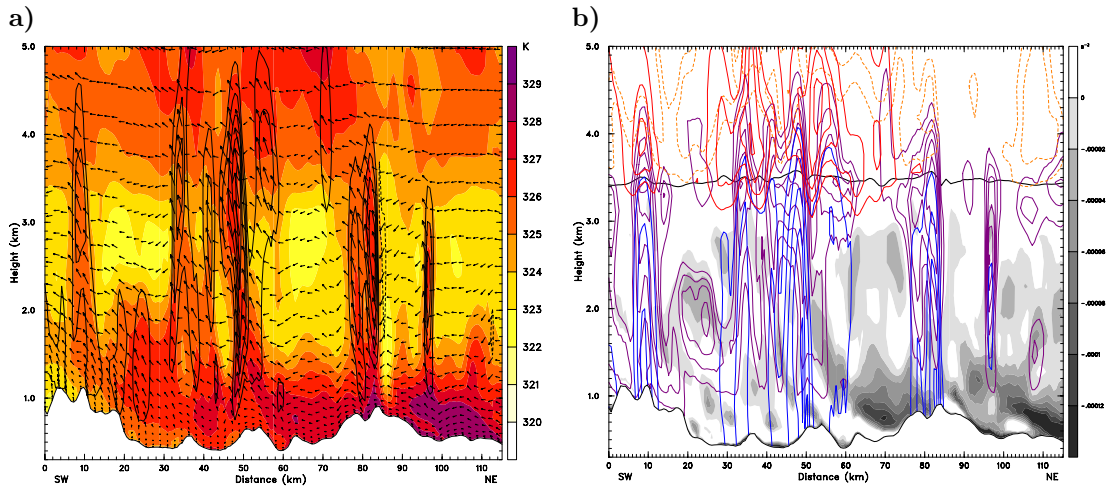

Figure 6.6: As in Fig. 5.16, but for the WSM5* simulation and larger contour interval for mixing ratio of snow (thin dashed black lines, contour interval 0.4 g kg^{-1}). The vertical cross-section is indicated by the solid black line in Fig. 6.5a.

WSM5* run, in comparison to the REF simulation, are located at higher altitudes, which results from the different fall speeds of snow and graupel particles. Although the amount of snow mass is increased above the melting line, the surface precipitation field over the Alpine foreland (see Fig. 6.5a) is hardly influenced, because of reduced melting of the slower falling snow crystals. Both in 3 and 4 km MSL the WSM5* run produces more snow over high mountain peaks of the main Alpine crest, which can be seen in the southwestern and southeastern corners of the domain in Fig. 6.7b and over large parts of the Alpine crest in Fig. 6.7d. However, localized peaks of the snow mixing ratio at 3 km MSL over the Alpine foreland and the Black Forest appear to be smaller in the WSM5* simulation. Thus, judging from the snow field in 3 km MSL, the structure of cellular convection appears to be less pronounced at this height. At a higher elevation of 4 km MSL the mixing ratio at the center positions of the cells are still smaller than in the REF run, but the differences have significantly decreased. However, the areas surrounding the cellular spots receive significantly more snow particles than graupel particles in the REF run, as the WSM5* run increasingly spreads the snow around the convective updrafts.

In Figure 6.5a an area with large positive deviations ($>$ 60 mm) is noticeable over two ridges located in the southwestern part of the domain. A corresponding cross-section (see Fig. 6.8) exhibits two very high mountains with peaks reaching above the melting line. Although both the wind field (not shown) and the stratification pattern are nearly identical, the WSM5* simulation produces a maximum snow mixing ratio of 1.8 g kg^{-1}, which is higher than the maximum graupel mixing ratio of 0.7 g kg^{-1} in the REF simulation. As a consequence, mountainous regions

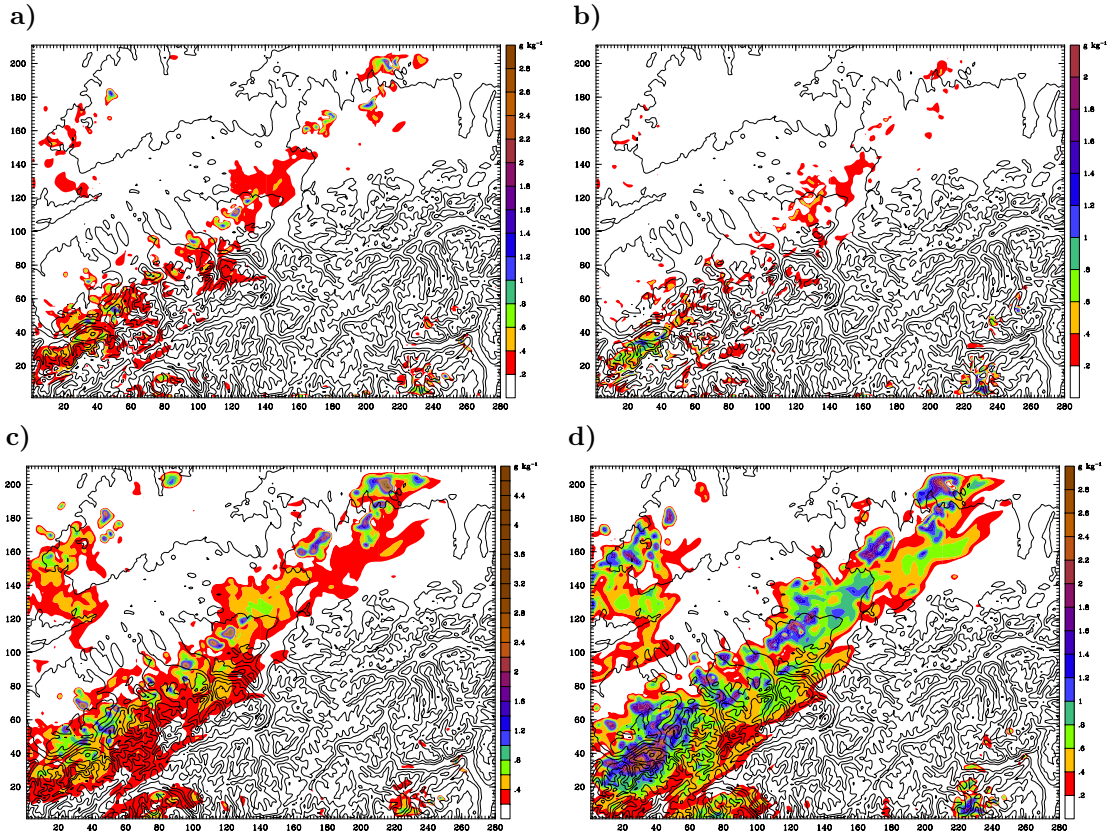

Figure 6.7: Subfigures (a),(c) show the sum of snow and graupel mixing ratios in g kg^{-1} at 1800 UTC 21 Aug at height level (a) 3 km and (c) 4 km from the REF simulation. Subfigures (b),(d) show the snow mixing ratio from the WSM5* simulation for the same heights. Contour lines indicate orography every 600 m.

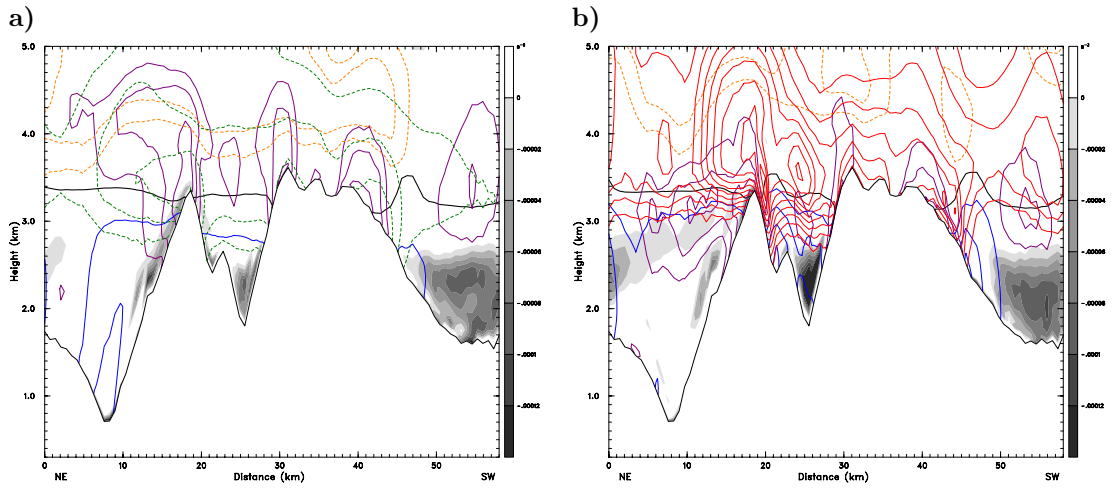

Figure 6.8: Hydrometeor mixing ratios and moist squared Brunt-Väisälä frequency as in Fig. 5.18, but (a) for the REF simulation at 1800 UTC 21 Aug and (b) for the WSM5* simulation at 1800 UTC 21 Aug. For quantitative comparison the contour interval for mixing ratio of snow and graupel is changed (contour interval 0.2 g kg^{-1}). The vertical cross-section is indicated by the dashed black line in Fig. 6.5a. Flow direction is from left to right.

reaching close to or above the melting line receive higher amounts of solid precipitation in the WSM5* run, which becomes obvious in Fig. 6.5. Note that in the REF run the supercooled liquid water cloud reaches higher above the melting line. Thus, the total precipitable water is presumably still the same as in the WSM5* run.

In a next step accumulated precipitation of the WSM5* run during period 2, which is dominated by stable orographic precipitation, is compared to the REF simulation. Figure 6.5b shows the differences in accumulated precipitation. Changes to the REF run appear mainly over the main Alpine crests at isolated locations with high mountains in the center and the western part of the domain. At several of these locations both a minimum deviation and a maximum deviation is discernable. The modifications to the spatial precipitation distribution reveal an increase of precipitation along the lee sides of the mountain ridges and downstream located valley locations, but a reduction on top of the ridges. The described effect is completely bound to high mountains. Over low mountains, e.g. at the northern rim of the Alpine barrier or the Black Forest mountains, no remarkable modifications during this period of moist stable stratified flow are observed. In terms of statistical parameters the WRF area average AVG is decreased by 2 %. The RMSE and NAE reduce correspondingly small by 0.7 mm and 1.5 mm, respectively.

A vertical cross-section of the vertical velocity field is shown in Fig. 6.9a. It appears unmodified and nearly identical to the REF run (see Fig. 5.18a). Mountain

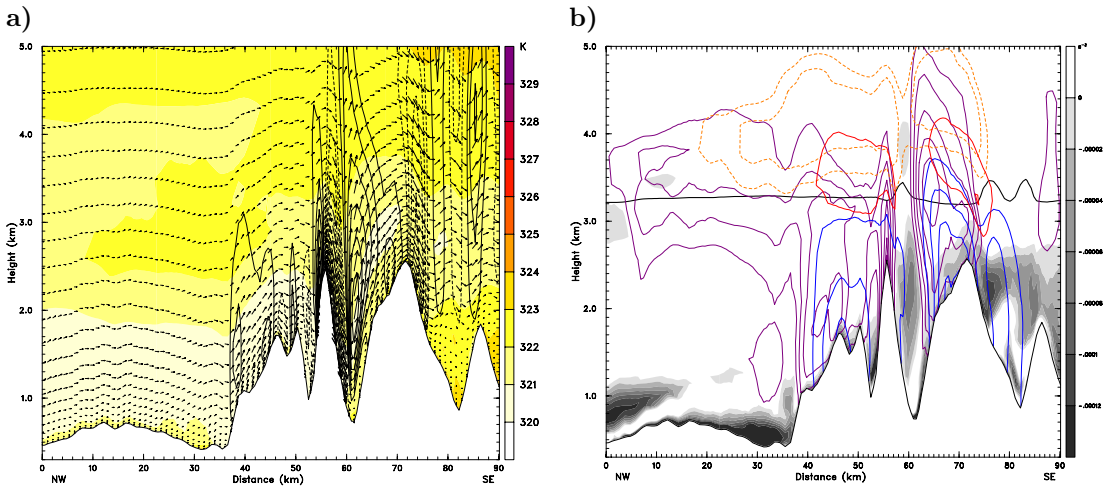

Figure 6.9: As in Fig. 5.18, but for the WSM5* simulation and snow mixing ratio contour interval equivalent to the graupel contour interval in Fig. 5.18 (0.4 g kg^{-1}). For quantitative comparison the contour interval for mixing ratio of snow and graupel is changed (contour interval 0.2 g kg^{-1}). The vertical cross-section is indicated by the solid black line in Fig. 6.5b.

induced up- and downdrafts of unchanged magnitudes are visible. Figure 6.9b shows moist stable atmospheric conditions and hardly any differences to the REF run (see Fig. 5.18b) can be found. The lee side advection of precipitating mixed-phase hydrometeors is clearly visible in both simulations, but it is increased in the WSM5* simulation, which produces a snow cloud that reaches further downstream into the lee. Thus, in contrast to the REF run, the fallout of rain is delayed and therefore shifted downstream into the lee of the mountain, where the snow crystals melt. A secondary maximum of precipitation is gained from this spillover.

To prove the above described results, another vertical cross-section is shown in Fig. 6.10. The location of the cross-section is shown in Fig. 6.5b. Again the comparison of the hydrometeor mixing ratios over and downstream of the highest mountain uncovers a shift of precipitation into the lee side of the crest. The snow cloud in the WSM5* run, which has approximately twice the mass of the graupel cloud in the REF simulation, is located both slightly more downstream and at a higher altitude. A secondary maximum of rain over the lee side results from the melting of large amounts of downstream advected snow crystals. This enhancement of lee side precipitation results from a slower conversion from snow crystals to the liquid water phase, because snow particles have a smaller terminal velocity than graupel (see Fig. 3.2) and cause less efficient coalescence and collision with rain drops and cloud particles. Apparently, the described delay of precipitation is bound to higher elevations where snow crystals are available. Note that for a comparison to the Thompson scheme an additional cross-section through the western part of the domain is presented in section 6.3.

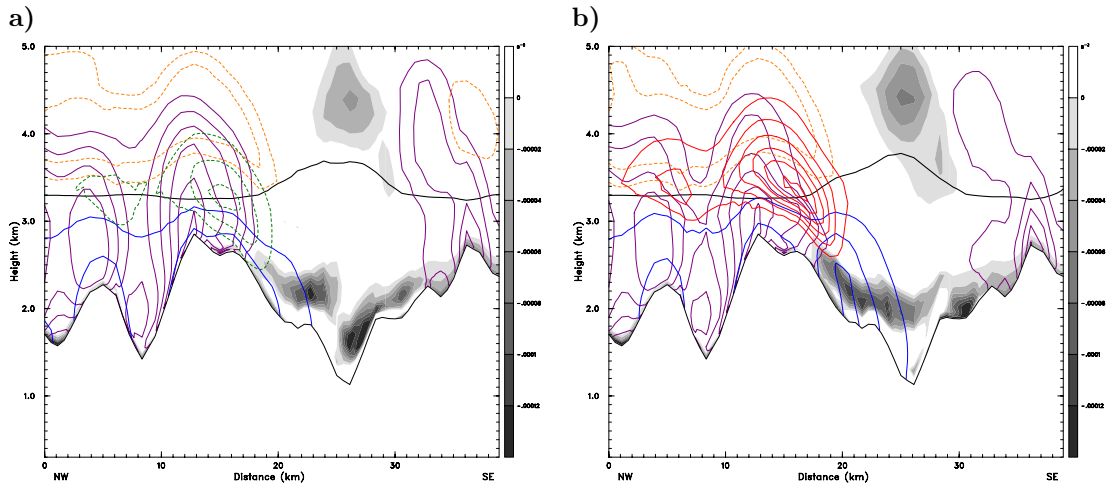

Figure 6.10: Hydrometeor mixing ratios and moist squared Brunt-Väisälä frequency as in Fig. 5.18, but at 2200 UTC 22 August. For quantitative comparison the contour interval for mixing ratio of snow and graupel is changed (contour interval 0.2 g kg^{-1}). The vertical cross-section is indicated by the dashed black line in Fig. 6.5b.

6.3 "Thompson" run

The Thompson scheme, as partly described in section 3.4.3, is used in a numerical simulation (THOM), which is here described and compared to observations, the reference run (REF), and the WSM5* run. Figure 6.11a reveals a general reduction of precipitation during period 1 when the Thompson scheme is applied instead of the WSM6* scheme. The Black Forest region receives 40 mm less rain. Precipitation over the southeast of the domain, where the flow is entering the domain, is also significantly lowered. Banded structures of negative differences (< -20 mm) appear over the Alpine foreland, but are not compensated at locations with increased convective precipitation, as it is the case in the WSM5* run. Only infrequently, e.g., downstream of the Black Forest or over the southwest of the domain, low positive banded patterns from increased embedded convective precipitation are visible. The WRF area-averaged precipitation significantly decreases by 21 %. Both error scores RMSE and NAE increase by 1.6 mm and 2.7 mm, respectively.

Horizontal cross-sections of hydrometeor mixing ratios are analyzed next. Actually only very small amounts of ice crystals are present above 7 km MSL (not shown). Graupel mixing ratios are also neglectably small in comparison to the generated snow mixing ratios. Figure 6.12, which shows the sum of snow and graupel mixing ratios from the THOM simulation, allows a quantitative comparison to the distributions of the REF and WSM5* runs, which are shown in Fig. 6.7. At 4 km MSL a significant increase of the snow mixing ratio is discernable in the THOM simulation. In comparison to the REF run the mixing ratios are higher and seem to be more widespread. However, in the centers of the embedded convective cells the

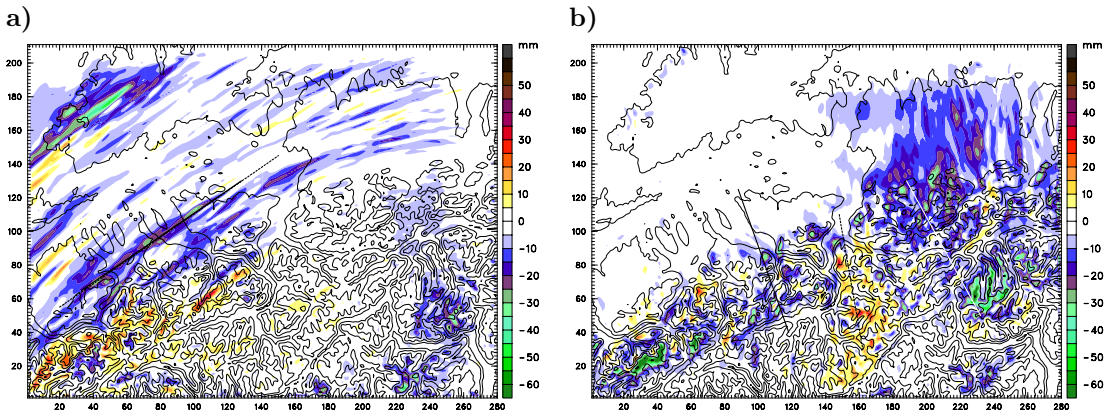

Figure 6.11: Differences in 12-hour accumulated precipitation (THOM − REF) in mm for (a) period 1 and (b) period 2. Cold colors indicate less precipitation predicted by the Thompson scheme. Contour lines indicate orography every 600 m.

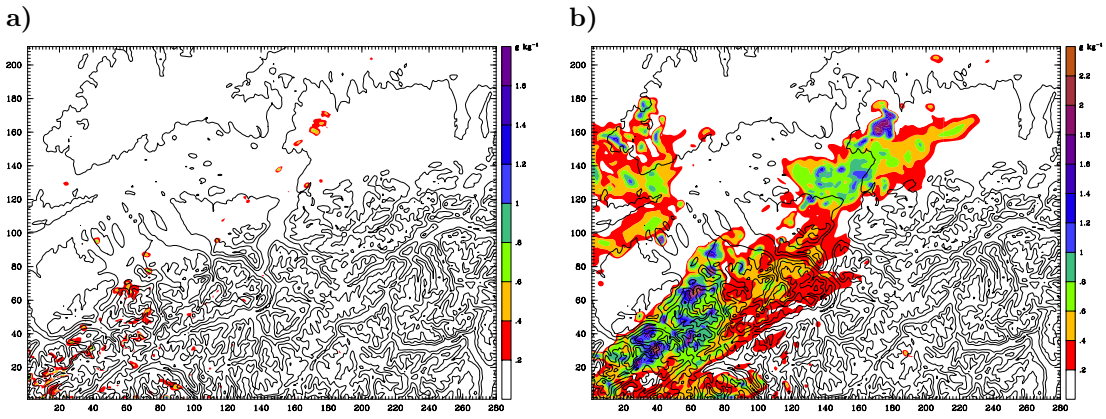

Figure 6.12: The sum of snow and graupel mixing ratios in g kg^{-1} for the THOM simulation at (a) 3 km and (b) 4 km MSL at 1800 UTC 21 Aug. Contour lines indicate orography every 600 m.

graupel mixing ratios from the REF run are still higher, which results in isolated peaks of larger graupel mixing ratios and stronger horizontal mixing ratio gradients in the REF run. At 3 km MSL cellular convective activity in the THOM run is indicated by isolated peaks of small amounts of snow over the Alpine foreland. At this height and region the REF run produces more graupel than there is snow produced by the THOM simulation. The same fact accounts for the Black Forest region. Compared to the WSM5* simulation (see Fig. 6.7) the THOM run produces less snow over the nearly flat terrain north of the main Alpine crests.

The lack of graupel in the THOM simulation surely contributes to the discrepancies in the precipitation field because the snow crystals, which have a smaller terminal velocity than graupel particles and are thus located at a higher altitude. Thereby the potential available snow mass for melting near the freezing level is reduced, causing a decrease of liquid water production due to melting. Note that besides warm-rain processes mixed-phase processes contribute to the formation of liquid water. Figures 6.14 and 6.17 show larger mixing ratios of snow than of cloud water. The introduced changes to the properties of snow, as explained in section 3.4.3, might cause the differences to the snow fields of the WSM5* run. Assumptions for the interaction between snow and graupel are shown in section 3.4.3. In this case the production of graupel from snow might be too weak. However, reasons can only be found on a hypothetical basis. In section 6.4.3 a sensitivity test regarding the graupel-snow interaction is conducted.

To further explain the differences to the REF run during period 1, cross-sections of θ_e and the vertical velocity are shown in Fig. 6.13a. A pronounced θ_e inversion is present, causing highly potentially unstable atmospheric conditions. The maxima of vertical velocity reveal that convective cells are placed at several locations in the cross-section, but in comparison to the REF run, these locations of embedded convective cells are altered and updraft velocities appear smaller. The hydrometeor fields show low rain mixing ratios and nearly no snow, graupel, and ice mass at this time and location, a fact that results from a lack of moist convection at this location and time step. Another example for hydrometeor distributions during embedded cellular convection is shown in Figs. 6.14a,b. At this time both simulations are characterized by an approximately 2.5 km thick unstable layer, leading to heavier moist convection than in the previously described cross-section of the THOM run. Again no ice crystals are present above the freezing level in the THOM run. However, a pronounced snow cloud is now visible in Fig. 6.14b and the snow mixing ratios are comparable with or even exceed the graupel mixing ratios of the REF run. Evidently, the maximum amount of graupel is located further below the melting line than the maximum of the snow amount in the THOM simulation, a fact that originates from the different terminal velocities of the hydrometeor

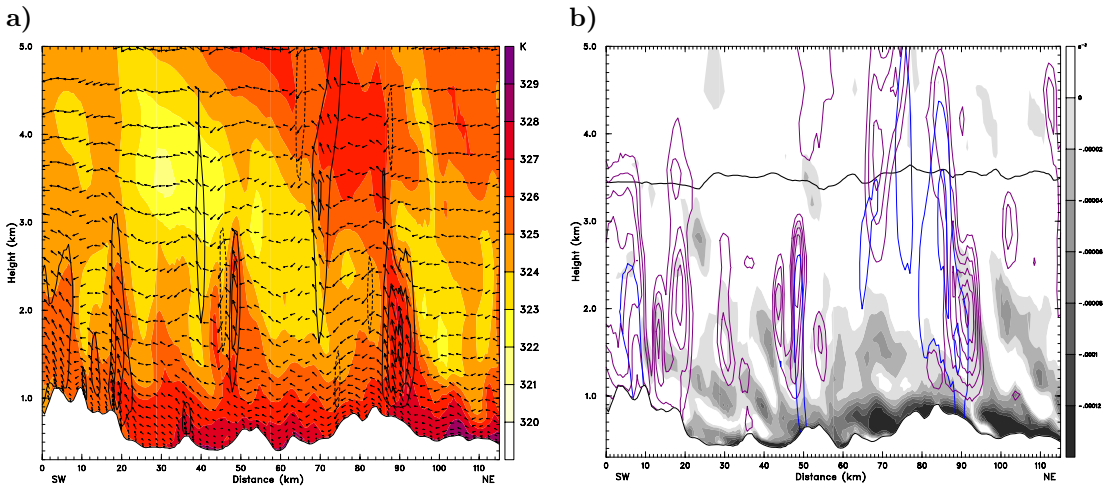

Figure 6.13: As in Fig. 5.16, but from Thompson simulation. The vertical cross-section is indicated by the black line in Fig. 6.11a.

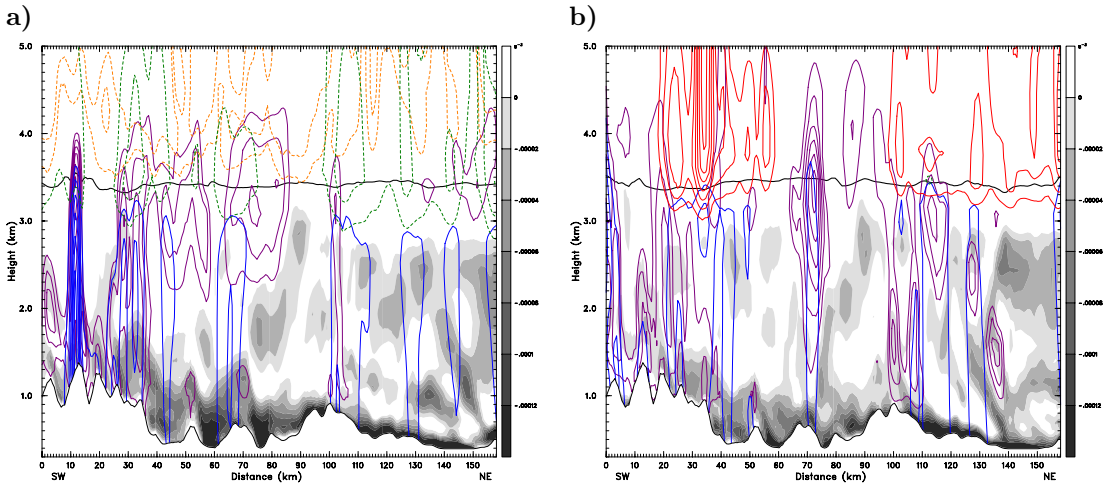

Figure 6.14: As described in Fig. 5.18, but (a) from the REF and (b) from Thompson simulation both at 1830 UTC 21 August. Snow and graupel mixing ratio contour interval are both 0.2 g kg^{-1}. The vertical cross-section is indicated by the gray line in Fig. 6.11a.

categories. The precipitation of the REF simulation in Fig. 6.14a appears increased over mountains at the left end of the cross-section, where the melting of graupel is involved in the precipitation process. Such high rain mixing ratios are not achieved in the THOM run in this cross-section, although large snow mixing ratios would be potentially available above the melting line in the left part of the cross-section.

Figure 6.11b shows the differences in accumulated precipitation patterns of the REF and THOM simulation during period 2. A general decrease of orographic precipitation is visible over the main Alpine crest in the center of the domain. Also the convective precipitation over the Alpine foreland in the western part of the domain is reduced by 20 mm. Two regions receive significantly less solid precipitation than

the REF run. At both locations over the highest mountains in the southwest and over the southeast of the domain the precipitation is reduced by more than 60 mm. Precipitation over the main Alpine barrier and the eastern Alpine foreland is also decreased. One area with increased precipitation appears in the south, right in the middle of the domain, over the main Alpine crests. The tendency to generate a systematically modified small-scale precipitation pattern over complex terrain is not noticeable. The reduction of precipitation reduces the WRF area-averaged precipitation by 15 % during 22 August. As a consequence the RMSE and NAE increase by 4.1 and 2.9 mm, respectively.

In order to gain better knowledge of the microphysical processes during the period of stable stratified orographic precipitation in a next step horizontal cross-sections of hydrometeor mixing ratios are explored. They reveal that only a few isolated locations with noticeable graupel mixing ratio are present. However, their magnitudes are negligible. The ice mixing ratio, in agreement with the findings during period 1, appear to be of extremely low magnitudes. The sums of the snow and graupel fields from both the THOM and the REF run at 2300 UTC 22 August

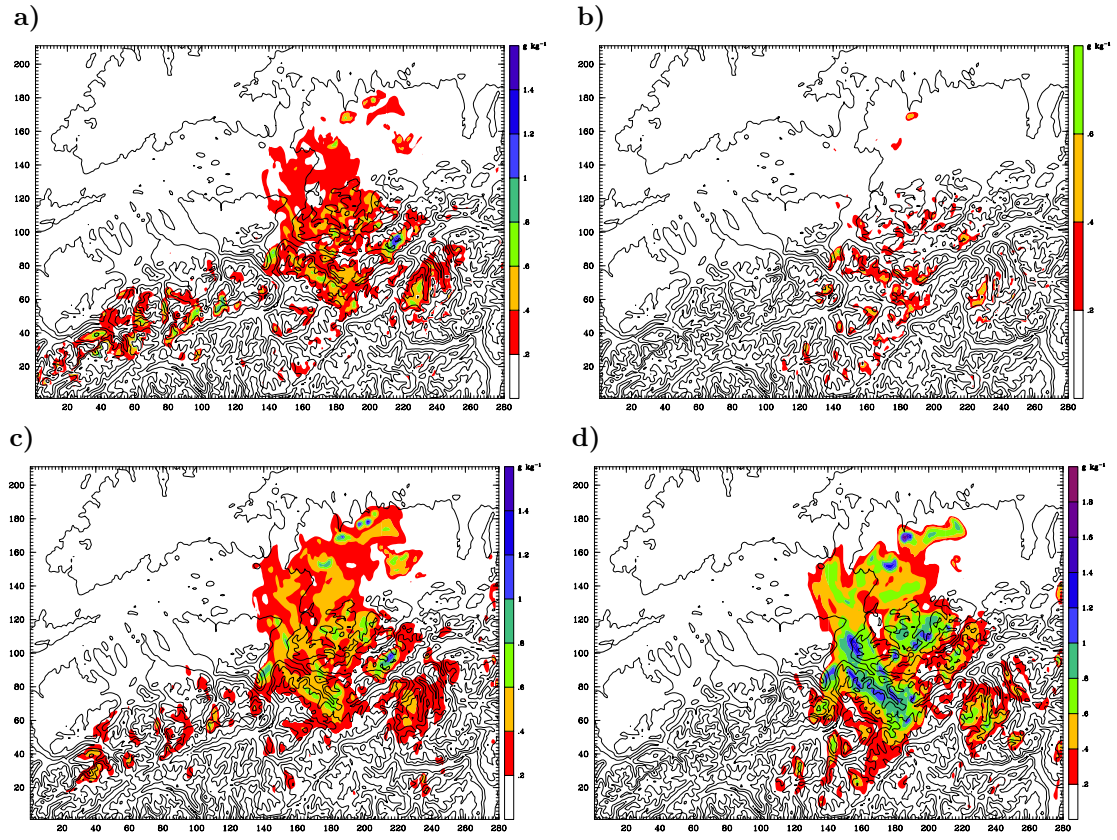

Figure 6.15: Subfigures (a),(c) show the sum of snow and graupel mixing ratios in g kg^{-1} at 2300 UTC 22 Aug at (a) 3 km MSL and (c) 4 km MSL from the REF simulation. Subfigures (b),(d) show the results from the THOM simulation for the same heights. Contour lines indicate orography every 600 m.

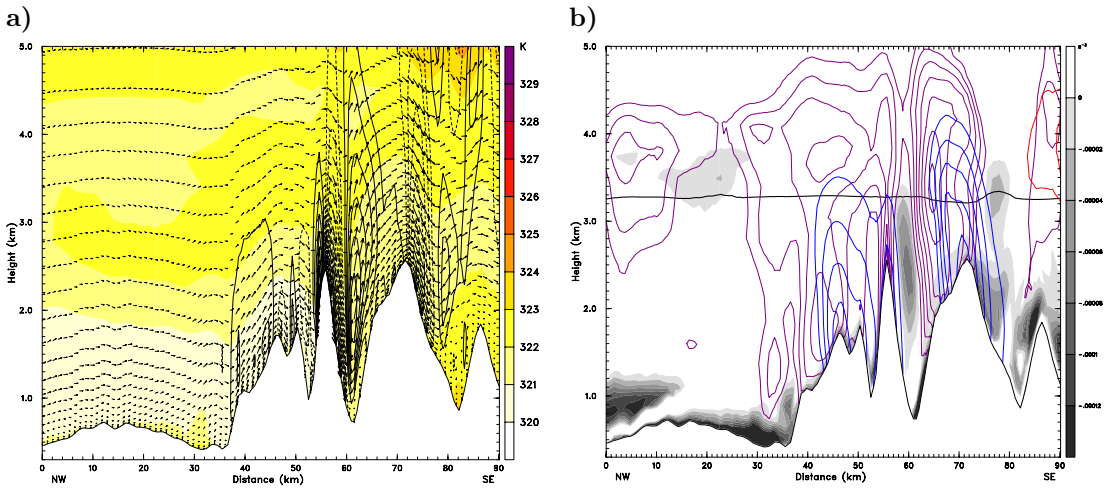

Figure 6.16: As in Fig. 5.18, but from Thompson simulation. The vertical cross-section is indicated by the black line in Fig. 6.11b.

are shown in Fig. 6.15. As already shown for period 1, due to a smaller terminal velocity snow reaches its maximum mixing ratio at approximately 4 km MSL above sea level in the THOM run, whereas the graupel mixing ratios in the REF run appear most pronounced slightly above 3 km MSL. At 3 km MSL only few isolated dots of mentionable amounts of mixed phase hydrometeors appear in the THOM run (see Fig. 6.15b), which is significantly less than in the REF run (see Fig. 6.15a). In both 3 and 4 km MSL the area covered by the snow cloud appears much more confined than in the REF run, as no snow is produced in the west of the domain. The horizontal cross-sections in 4 km MSL (see Fig. 6.15c,d) uncover large amounts of snow in the THOM simulation, but again only over a quite restricted region. A possible reason for the reduction of the snow mass in the west of the domain is a decreased production from ice crystals, as only small amounts of ice are present.

In the following a vertical cross-section at 2300 UTC 22 August is explored. The location of the transect is indicated in Fig. 6.11b. Figure 6.16a shows a hardly altered field of vertical velocities and potential stable conditions. The moist static stability is only marginally affected. The comparison of hydrometeor mixing ratio fields (see Fig. 6.16b) with the reference cross-section in Fig. 5.18b shows lower mixing ratios of ice crystals and graupel particles. Actually hardly any snow hydrometeors are produced at this location, as at this time the cross-section is not intersecting the snow cloud (see Fig. 6.15d). Astonishingly, the rain mixing ratio is higher in Fig. 6.16 than in the REF run, although the precipitation is decreased during this time. However, further inspection of the same cross-section, but at earlier dates, reveals comparatively low rain mixing ratios.

The previously mentioned small area of positive deviations in the south of the do-

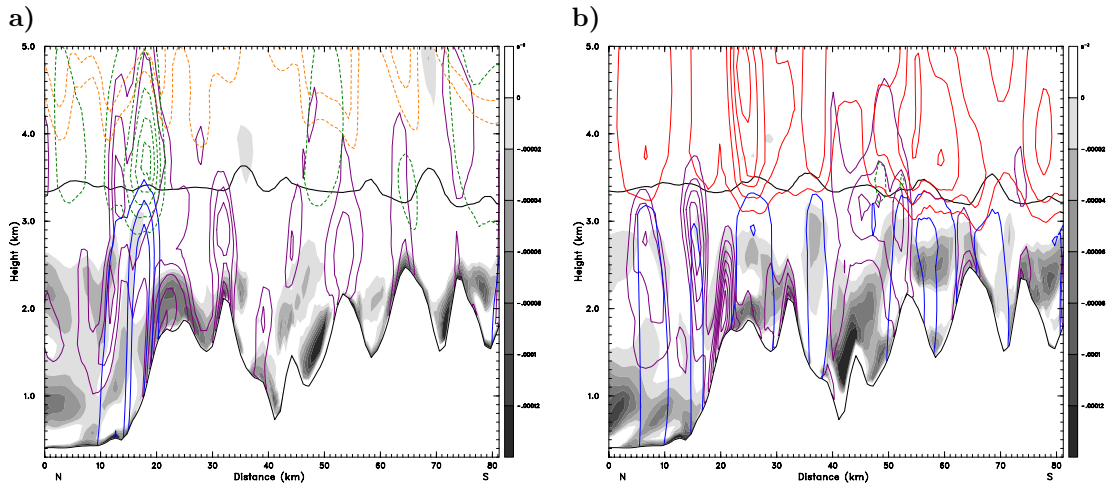

Figure 6.17: Hydrometeor mixing ratios and squared moist Brunt-Väisälä frequency as described in Fig. 5.16, but (a) for the REF and (b) for the THOM simulation both at 1830 UTC 22 August. Snow and graupel mixing ratio contour interval are both 0.4 g kg^{-1}. The vertical cross-section is indicated by the gray line in Fig. 6.11b.

main (see Fig. 6.11), is now discussed. Figure 6.17 shows, that at 1850 UTC 22 August and at this certain location the stratification is still slightly moist unstable, which may be a reason for discrepancies in the precipitation patterns of the two simulations. What seems to be more important is the amount of snow produced by the THOM run. A persistent increase in precipitation is predicted at this location, which results from melting of a pronounced snow cloud aloft. A graupel cloud of comparable mixing ratios does not form in the REF simulation. The REF run generates increased graupel mixing ratios only over the first mountain in Fig. 6.17a, but not over the further downstream located peaks. Thus, in comaprison to the REF run the precipitation reaches deeper into the mountainous parts of the shown cross-section.

One reason, why no systematic modification or shift of the small-scale precipitation pattern over complex terrain is yielded, is the limited extent of the snow cloud. The WSM5* run (see section 6.3) persistently produced larger amounts of snow over the entire Alpine barrier and showed, that the substitution of snow for graupel causes a delay of the precipitation fallout to the lee sides of high ridges. However, also in the regions with larger amounts of snow the THOM run does not exhibit organized sytematic discrepancies in the small-scale spatial precipitation distribution. A comparison of vertical cross-sections of the hydrometeor fields of the THOM and REF simulation is shown in Fig. 6.18 at 0230 UTC 23 August. At this time the WSM5* run (see Fig. 6.18a) produces pronounced snow clouds that reach into the lee of the mountain peaks and result in secondary maxima of the rain mixing ratios due to melting. Although at this location snow crystals are generated close to the melting line, the THOM simulation bears no significant secondary lee side precip-

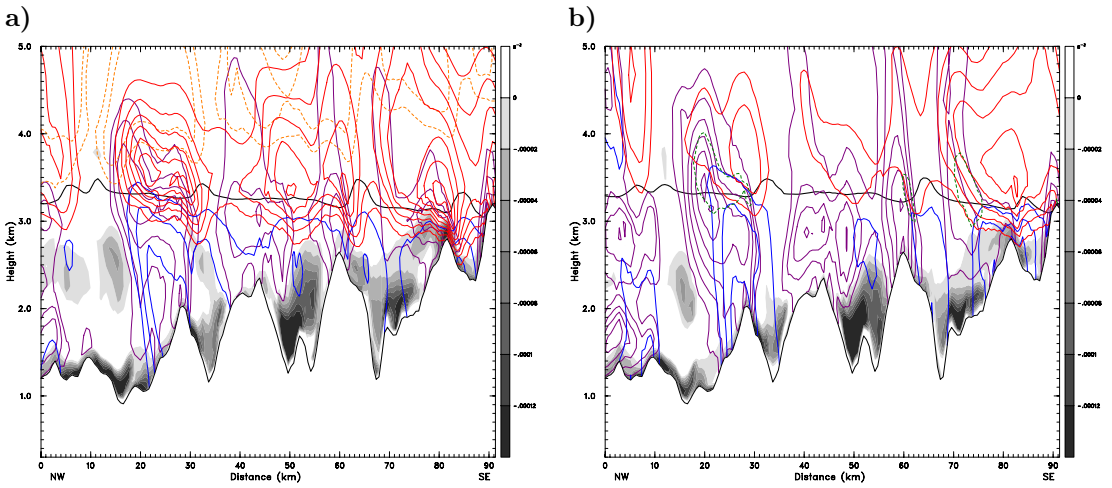

Figure 6.18: As described in Fig. 5.18, but (a) from the WSM5* and (b) from THOM simulation both at 0230 UTC 23 August. Snow and graupel mixing ratio contour interval are both 0.2 g kg^{-1}. The vertical cross-section is indicated by the white line in Fig. 6.11b.

itation from melting snow (see Fig. 6.18b), as the mass of the snow cloud is by at least 0.6 g kg^{-1} smaller. Additionally, in the THOM simulation moderate amounts of graupel particles over the first main ridge in the cross-section in Fig. 6.18b might accelerate the fallout of precipitation.

6.4 Microphysics sensitivity experiments

6.4.1 Maritime cloud

The complexity of interacting microphysical processes of the WRF single-moment bulk microphysics scheme WSM6* is described in section 3.4.2. One of the processes that determines the amount of rain production is the autoconversion from cloud water to rain droplets. This production term, as already shown in section 3.4.2, is indirect proportional to the cloud droplet number concentration ($\sim N_c^{-1/3}$). Thus, the autoconversion decreases with increasing number concentration N_c. For the WRF reference run (REF) a value of 300 cm^{-3} was used, which corresponds to a continental cloud type with a large number of CCN. In the sensitivity run presented in this section a lower value of 50 cm^{-3}, which is typical for a cloud of maritime type, is assumed. It should be mentioned that also heterogeneous freezing of supercooled cloud droplets is influenced by a modification of the cloud droplet number concentration, because the corresponding freezing term is, as described in section 3.4.2, indirect proportional to the cloud droplet number concentration ($\sim N_c^{-1}$). But, as heterogeneous freezing only occurs above the melting line, which is situated above most of the mountain crests in this case, the dominating effect should be an increase in rain production due to autoconversion. The results of this sensitivity simulation are again compared to the REF run. In the following the sensitivity simulation will be abbreviated as MAR.

Figure 6.19a shows the difference between the accumulated precipitation fields of the REF and the MAR run for period 1. Only small modifications are visible over the northern Alpine foreland, where the deviations to the REF run are smaller than

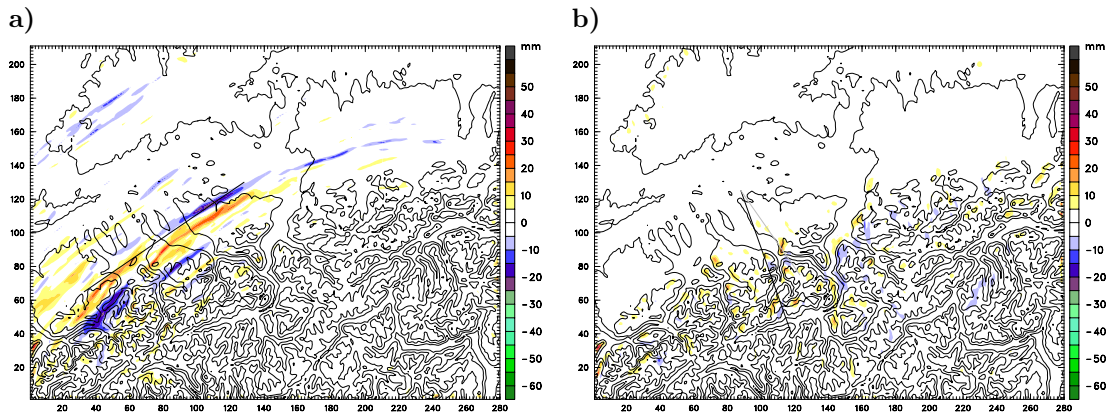

Figure 6.19: Differences in 12-hour accumulated precipitation (MAR − REF) in mm for (a) period 1 and (b) period 2. Cold colors indicate less precipitation predicted by the simulation with maritime cloud droplet number concentration. Contour lines indicate orography every 600 m.

5 mm. Larger discrepancies are only noticeable at the location with extreme amounts of precipitation over central Switzerland. Again, here the small-scale variability of precipitation is produced by the embedded convective cells, that are slightly out of phase in the two experiments. A decrease of precipitation is visible over the Black Forest region, but compensating positive changes are obtained at adjacent locations. The precipitation field in Fig. 6.19a shows that the modification of the cloud number concentration influences the prediction of moist convection and its resulting spatial precipitation pattern. Due to the stochastic component in the prediction of convective precipitation, here already fine modifications of a model constant (N_c) lead to a different precipitation pattern. The tendency to produce higher precipitation amounts can not be seen from these random diversifications. In terms of statistical behavior no remarkable modifications are obtained, as in most parts of the domain the precipitation field is nearly unaltered. The area average AVG of daily accumulated precipitation and the station average AVG_{sy} only increase by 2 % from 27.3 mm to 27.8 mm and by 0.8 % from 25.7 mm to 25.9 mm, respectively. Both the RMSE, which increases slightly by 0.1 mm, and the NAE, which decreases by 0.2 mm, are nearly unaffected. Analysis of vertical cross-sections (not shown) reveal only insignificant modifications of the wind and θ_e fields. However, the numerical randomness of the prediction of moist convection is indicated by slightly altered positions of the updrafts. Furthermore, they reveal that, despite unmodified hydrometeor distributions, convective precipitation decreases over the Black Forest region.

Again only small differences to the accumulated precipitation field of the REF run are yielded during period 2 (see Fig. 6.19b). Regions with an increase of the amount of precipitation are obtained over the windward slopes of the mountains in the center and the western parts of the domain. Little enhancement of precipitation is also visible over the Black Forest mountains. In the eastern parts of the domain both positive and negative deviations to the REF run appear over the mountainous regions, because there the precipitation field is very sensitive to the moist unstable atmospheric stratification. Note that all above described changes in hydrometeor mixing ratios are relatively small and exert only little influence on the precipitation field. The simulation with modified cloud number concentration results in an increase of the WRF domain average AVG by only 1.7 % from 27.3 mm to 27.8 mm. The model-derived station average AVG_{sy} also increases by 0.5 mm to a value of 50.2 mm. Despite these modifications in terms of precipitation averages, both the RMSE and the NAE increase by 0.7 and 0.4 mm, respectively.

Further insight into the microphysical modifications is gained by the cross-section of the hydrometeor species in Figs. 6.20a,b. Figure 6.20a is identical to Fig. 5.18b, but a finer spacing for the contour lines of rain and cloud water mixing

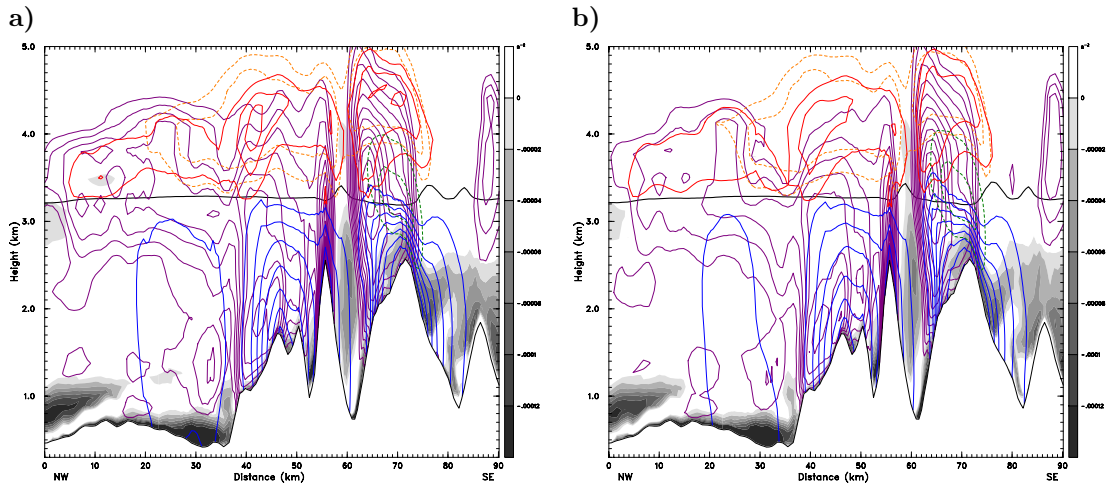

Figure 6.20: As described in Fig. 5.18, but (a) for the REF run and (b) for the MAR sensitivity experiment. Rain and cloud water mixing ratio contour interval are both 0.1 g kg^{-1}. The vertical cross-section is indicated by the black line in Fig. 6.19b.

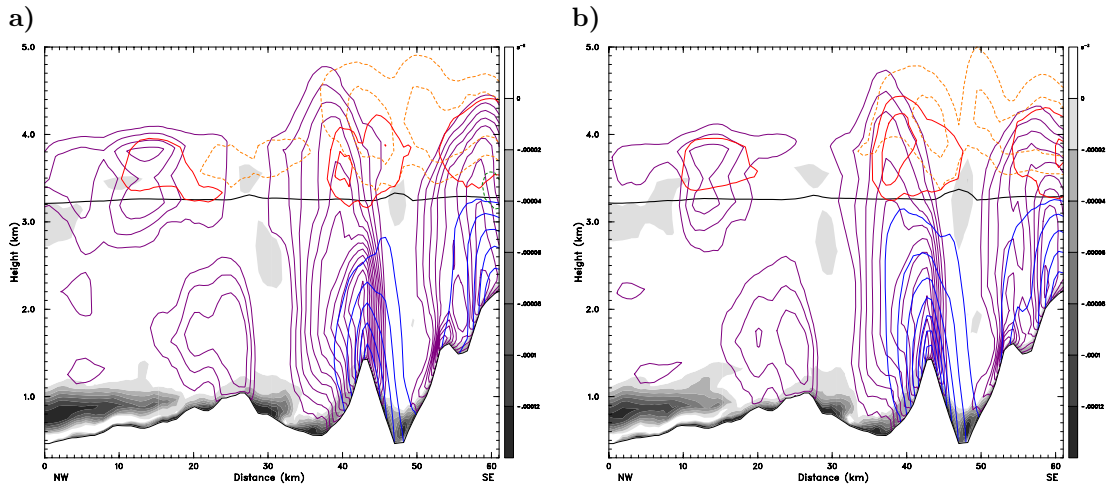

Figure 6.21: As described in Fig. 5.18, but (a) for the REF run and (b) for the MAR sensitivity experiment. Rain and cloud water mixing ratio contour interval are both 0.1 g kg^{-1}. The vertical cross-section is indicated by the gray line in Fig. 6.19b.

ratio is used. Figure 6.20b shows a small decrease ($\sim$ 0.1g kg^{-1}) of the low-level water cloud over the adjacent flatland and the upstream facing slope in the MAR experiment, because of the reduction of the critical droplet size for autoconversion (see section 3.4.2). However, at this certain time step no increase in rain mixing ratio is achieved. Additionally, a decrease of cloud water of approximately the same size is noticeable slightly above the melting line due to an increase of heterogeneous freezing of supercooled water. In order to prove these modifications, another comparison of hydrometeor mixing ratios is shown in Fig. 6.21. This time, as one would expect, the maximal rain mixing ratio in the MAR experiment is by 0.2 g kg^{-1} higher than in the REF run. A balancing decrease of the cloud mixing ratio by 0.2 g kg^{-1} is produced in the region of the rain cloud. A rapid decrease of supercooled cloud water with height is evident above the melting line in all of the three cloudy regions of the cross-section. However, an increase of ice crystal mixing ratios is not perceptible.

6.4.2 Gamma size distribution for graupel within Thompson

Thompson et al. (2004) suggest to assume a generalized gamma distribution for the graupel size distribution instead of the exponential Marshall-Palmer distribution, in order to improve numerical quantitative precipitation forecasts. To investigate the importance of the shape of the hydrometeor size distribution of the graupel category, here a sensitivity experiment (THOM_GD) with a gamma size distribution ($\mu = 1$ in Eq. 3.24) is conducted and compared to the previous Thompson run (THOM) run, in which an exponential distribution ($\mu = 0$) was assumed.

Figure 6.22 shows the differences in accumulated precipitation between the THOM and THOM_GD runs for both periods. Hardly any modifications to the precipitation field are generated. Embedded convective precipitation is slightly out

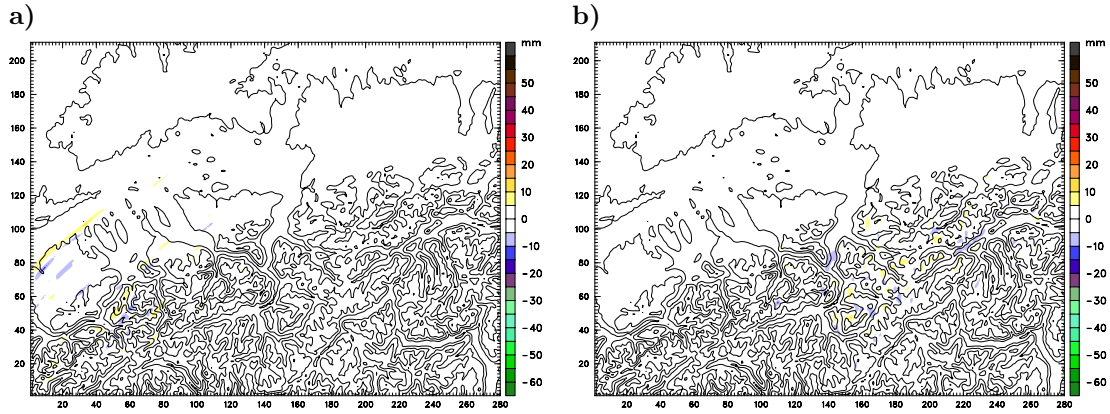

Figure 6.22: Differences in 12-hour accumulated precipitation (THOM_GD − THOM) in mm for (a) period 1 and (b) period 2. Contour lines indicate orography every 600 m.

of phase over central Switzerland, which results in adjacent banded differences with low magnitudes ($\sim$ 10 mm). Apparently, the precipitation field over the remaining areas of the domain is unchanged. During period 2 the precipitation field of the sensitivity experiment hardly diverges from the THOM simulation. At some locations in the eastern parts of the domain, where the precipitation is heavier and the moist static stability lower, small differences with maximum magnitudes of only 5 mm arise. The modifications appear to be even smaller than during period 1, where the inherent presence of moist convection caused higher variability between the simulations.

6.4.3 Enhanced snow to graupel transformation within Thompson

According to Thompson et al. (2008) the transformation of rimed snow crystals to the graupel category constitutes one of the largest uncertainties in the microphysics parameterization. The current method assigns partially rimed snow to graupel particles, as soon as the ratio between riming of snow and depositional growth of snow exceeds a fixed threshold (see section 3.4.3). Here a sensitivity experiment (THOM2) with a modified, increased graupel production from snow is tested and the results are compared to the original THOM run. The modifications yield an enhanced graupel production as soon as the riming of snow is three times as large as the depositional growth of snow. Further explanations of the parameterization are presented in section 3.4.3 and details about the implementation in the Thompson scheme are included in appendix B.

Figure 6.23 shows the differences in accumulated precipitation between the THOM and THOM2 run for both periods. Simlilar to the previous sensitivity experiment, only marginal modifications arise from the increased graupel production. Apparently, only insignificant differences (<15 mm) appear at scarce locations in central Switzerland (see Fig. 6.23a), where banded structures of both decreased and increased precipitation originate from a low predictability of convective precipitation during period 1. The magnitudes of the modifications in the rest of the domain remain smaller than 5 mm. During period 2, which is characterized by a higher atmospheric stability, the modifications to the original THOM run are even smaller (see Fig. 6.23b) than during period 1. The precipitation field is marginally altered at scattered locations over the main Alpine rim in the eastern part of the domain. The area-averaged daily precipitation AVG is unaffected and both the NAE and the RMSE increase only marginally during both periods.

Both the snow and graupel mixing ratios at 3.5 km MSL are plotted in Fig. 6.24 at 2300 UTC 22 August. Obviously, only an insignificant increase of the graupel

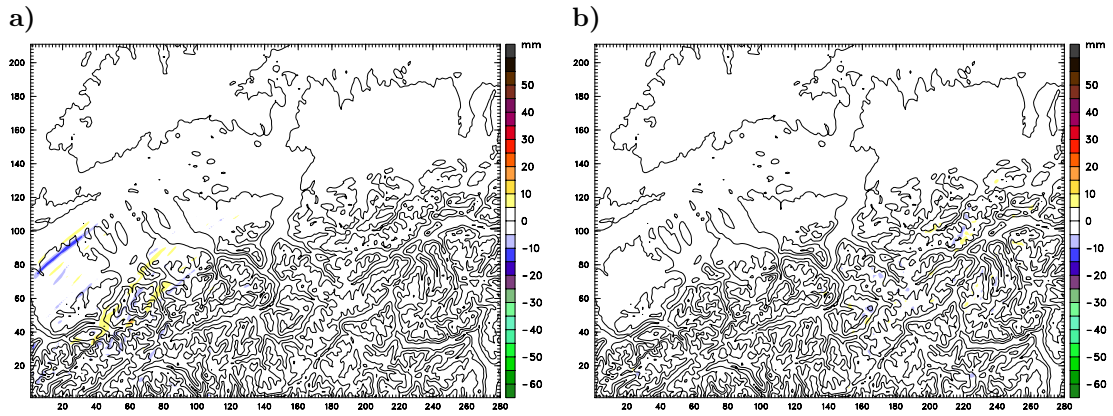

Figure 6.23: Differences in 12-hour accumulated precipitation (THOM2 − THOM) in mm for (a) period 1 and (b) period 2. Cold colors indicate less precipitation predicted by the modified THOM2 experiment, which transfers more snow to the graupel category. Contour lines indicate orography every 600 m.

mixing ratio and a marginal decrease of the snow crystals is discernable. The introduced parameterization of the graupel production does not considerably alter the precipitation field in this sensitivity run, but appears to be of secondary importance, as the small differences over the east of the domain could also result from the random appearance of convective precipitation.

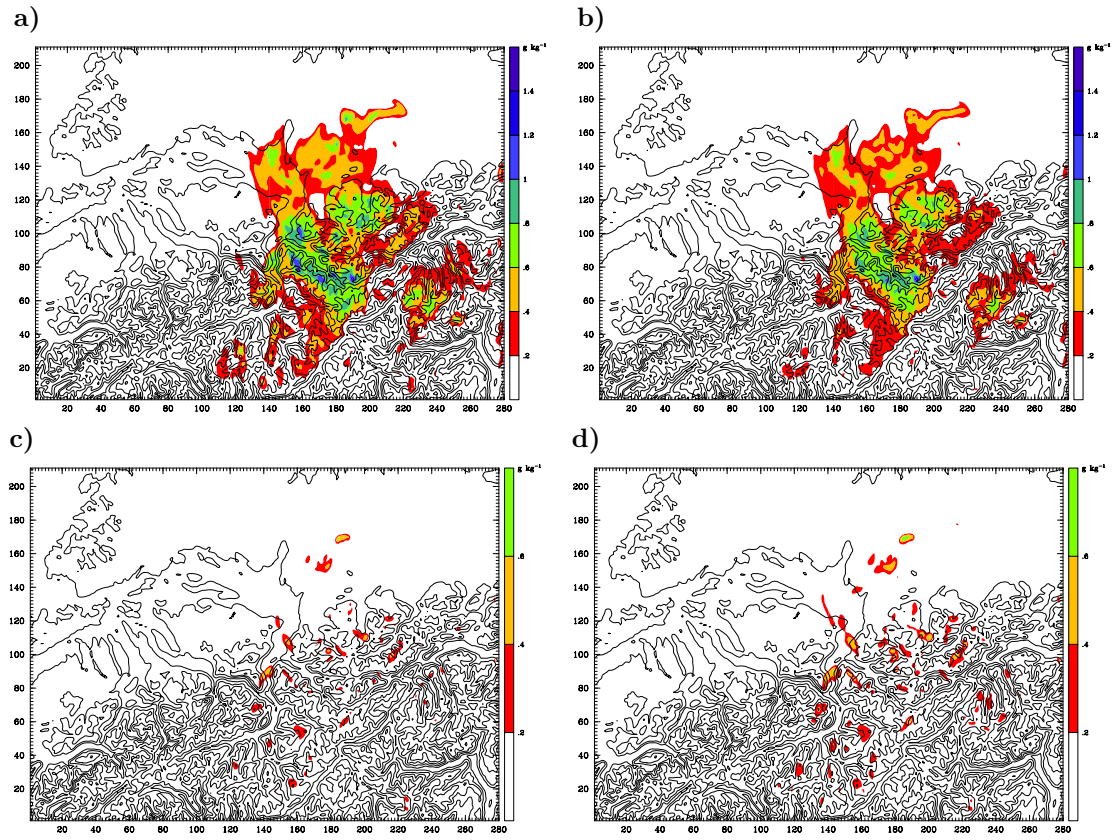

Figure 6.24: The left subfigures show (a) snow and (c) graupel mixing ratios at 3.5 km MSL in g kg^{-1} at 2300 UTC 22 Aug from the original THOM simulation. The right subfigures show (b) snow and (d) graupel mixing ratios from the modified THOM2 simulation with the increased snow to graupel transformation. Contour lines indicate orography every 600 m.

Chapter 7

Summary and conclusions

In this thesis numerical simulations of the August 2005 Alpine flood have been conducted using the Weather Research and Forecasting model (WRF) with a 1-km horizontal grid spacing in the innermost domain. Mechanisms of orographic precipitation and their sensitivity to microphysics parameterizations have been investigated.

The event was characterized by a slowly moving cyclone, which attributed to a permanent lifting of the air mass at the northern Alpine flanks on 21-23 August 2005. The WRF reference simulation showed good skill in capturing the observed surface precipitation and reproduced the precipitation structures of the radar measurements. However, the largest amounts of observed precipitation over western Austria were underestimated during 22 August 2005 and the extent of the affected precipitation area over the Alpine rim was predicted slightly too wide with too much precipitation over central Switzerland and southeastern Germany. In agreement with observations the maximum of accumulated precipitation was generated over central Switzerland on 21 August and over a more elongated area over the main Alpine rim on 22 August 2005.

Two characteristic periods with distinctive mechanisms of orographic precipitation have been identified during the event. Firstly, embedded in the northeasterly flow, convective cells propagated to the Swiss Alpine foreland during the second half of 21 August 2005. As a consequence the precipitation was enhanced already over the low-mountain terrain belonging to the Alpine foreland. At this time the air mass was characterized by a pronounced moist unstable stratified layer ($N_m^2 < 0$). Secondly, moist neutral and weakly stable stratified lifting ($N_m^2 > 0$) dominated the orographic precipitation over the northern Alpine flanks in central Switzerland during the second half of 22 August 2005 and the morning of 23 August 2005. The low-level jet was directed nearly perpendicular to the Alpine barrier at this time. It should be mentioned, that during this time moderate convective enhancement was still produced over eastern Switzerland and western Austria due to weak moist

unstable atmospheric conditions.

For both periods the precipitation fields of simulations with varied microphysics schemes have been compared to the reference run that used the WRF single-moment bulk microphysics scheme (WSM6*), which predicts six hydrometeor species including graupel. A Kessler type warm-rain scheme (no ice-phase) significantly reduced the precipitation by $\sim 40\%$ and $\sim 30\%$ during the first and second period, respectively, although the melting line was situated above most of the highest mountain crests. During the first period the intensity of shallow embedded cellular convection was remarkably decreased over the Alpine foreland compared to the reference run. As shown also in previous studies, the release of latent heat during freezing and the destabilization of the atmosphere by melting are necessary for the formation of rapid convective updrafts. Compared to the rain production in the reference run, the rate of autoconversion from cloud droplets to rain drops is too small in the Kessler scheme and causes a reduction of precipitation. However, the decrease of precipitation is inhomogeneous, as modifications of the small-scale precipitation distribution can cause relatively small reductions over some mountain peaks. In comparison to the reference run, a higher critical cloud mixing ratio for the autoconversion of cloud water to rain particles is assumed in the Kessler scheme. As a consequence, the formation of precipitation can be delayed and occur rather abrupt close to the mountain top, whereas the precipitation over the lee side reaches not that far downstream of the mountain crests.

Only small discrepancies to the precipitation field of the WSM6* scheme resulted from omitting the graupel category in the simulation with the WSM5* scheme. The WSM5* simulations exhibited large amounts of snow mass at about 4 km MSL, which are roughly twice as high as the graupel amount of the reference WSM6* scheme, which was located at 3 km MSL. The different heights of the maxima presumably result from the smaller terminal velocity of snow crystals. During the first period the amount of precipitation was only marginally decreased over the Alpine foreland, as both effects, the increase of snow mass and the higher altitude of maximum snow mixing ratios, seem to compensate each other. Thereby, the potential snow mass available for melting processes close to the melting line remains unmodified. During stable stratified precipitation the summits of high mountains, embedded in the main Alpine ridge, received significantly less precipitation, whereas the precipitation over leeward slopes and adjacent valleys was increased. There the downstream advection of the slower falling snow crystals led to an enhanced rain production by melting.

Compared to the WSM6* run, the Thompson microphysics scheme considerably reduced the precipitation amount by $\sim 20\%$ and $\sim 15\%$ during the first and second period, respectively. Only marginal amounts of graupel mass were produced, while

significantly more snow mass existed than in the WSM6* reference run. However, the produced snow mixing ratios remained smaller than in the WSM5* simulations and were restricted to a smaller area. Again, the altitude of the maximum snow mixing ratios was positioned higher than for graupel particles in the reference run. In the Thompson simulation the reduction of the melting of snow crystals inhibited the formation of comparable amounts of rain. An experimental simulation with enhanced graupel production from rimed snow revealed no influence on the generated precipitation field, as both graupel and snow mixing ratios were nearly insensitive to the introduced modifications. Although more snow crytals were produced by the Thompson scheme than by the WSM6* scheme, a systematic delay of the precipitation to the leeward slopes due to slower falling snow crytals is not achieved. In contrast to the WSM5* scheme, which produced secondary precipitation maxima due to increased lee side melting of snow crystals, the Thompson scheme predicted less potential snow mass for lee side melting.

Further sensitivity experiments with altered cloud microphysics were conducted. One WSM6* simulation with a typical maritime cloud droplet number concentration of 50 cm^{-3} (instead of a continental cloud with 300 cm^{-3}), and two further Thompson simulations with a gamma size distribution for graupel (instead of the exponential Marshall-Palmer distribution) and an increased transformation of rimed snow to graupel, respectively, were performed. All three simulations produced only marginal modifications to the precipitation fields of the original simulations during both periods. These simulations suggested that their precipitation field was more sensitive to the low predictability of embedded cellular convection than to microphysical conditions and processes during the first period. Consistent with previous studies (Hohenegger et al. 2006; Hohenegger et al. 2008; Trentmann et al. 2008), the timing and location of the convective updrafts varied among all simulations, although only small initial microphysical modifications were implemented. The relatively small area of the innermost model domain could probably have contributed to the marginal impacts of modifications in the microphysics scheme on the surface precipitation field.

References

Amt der Vorarlberger Landesregierung, 2005: Das Starkregen- und Hochwasserereignis des August 2005 in Vorarlberg. [Available online at http://www.vorarlberg.at/pdf/naturereignisdokumentatio.pdf].

Bader, M., and W. Roach, 1977: Orographic rainfall in warm sectors of depressions. *Quart. J. Roy. Meteor. Soc.*, **103**, 269–280.

Bayerisches Staatsministerium für Umwelt, Gesundheit und Verbraucherschutz, 2006: August-Hochwasser 2005 in Südbayern. [Available online at http://www.hnd.bayern.de/ereignisse/hw220805/hw200508_endbericht.pdf].

Bergeron, T., 1959: Über den Mechanismus der ausgiebigen Niederschläge. *Ber. Deut. Wetterd.*, **12**, 225–232.

Bezzola, G.R., and C. Hegg, 2007: Ereignisanalyse Hochwasser 2005. Teil 1 - Prozesse, Schäden und erste Einordnung. [Available online at http://www.wsl.ch/publikationen/books/7970_DE].

Bigg, E.K., 1953: The supercooling of water. *Proc. Phys. Soc.*, **66**, 688–694.

Bolton, D., 1980: The computation of equivalent potential temperature. *Mon. Wea. Rev.*, **62**, 2810–2828.

Bougeault, P. and Coauthors, 2001: The MAP Special Observing Period. *Bull. Amer. Meteor. Soc.*, **82**, 433–462.

Chen, S.H., and W.Y. Sun, 2002: A one-dimensional time dependent cloud model. *J. Meteor. Soc. Japan*, **80**, 99–118.

Colle, B.A., 2004: Sensitivity of orographic precipitation to changing ambient conditions and terrain geometries: An idealized modeling perspective. *J. Atmos. Sci.*, **61**, 588–605.

Colle, B.A., M.F. Garvert, J.B. Wolfe, C.F. Mass, and C.P. Woods, 2005: The 13–14 December 2001 IMPROVE-2 event. Part III: Simulated microphysical budgets and sensitivity studies. *J. Atmos. Sci.*, **61**, 3535–3558.

Colle, B.A., and C.F. Mass, 2000: The 5–9 February 1996 flooding event over the Pacific northwest: Sensitivity studies and evaluation of the MM5 precipitation

forecasts. *Mon. Wea. Rev.*, **128**, 593–617.

Colle, B.A., C.F. Mass, and K.J. Westrick, 2000: MM5 precipitation verification over the Pacific northwest during the 1997-99 cool seasons. *Wea. Forecasting*, **15**, 730–744.

Cooper, W.A., 1986: *Ice initation in natural clouds*, Volume 21 of *Meteor. Monogr.*, Chapter Precipitation enhancement: A scientific challenge, pp. 29–32. Amer. Meteor. Soc.

Cosma, S., E. Richard, and F. Miniscloux, 2002: The role of small-scale orographic features in the spatial distribution of precipitation. *Quart. J. Roy. Meteor. Soc*, **128**, 75–92.

Dudhia, J., 1989: Numerical study of convection observed during the winter monsoon experiment using a mesoscale two-dimensional model. *J. Atmos. Sci.*, **46**, 3077–3107.

Durran, D.R., and J.B. Klemp, 1982: On the effects of moisture on the Brunt-Väisälä frequency. *J. Atmos. Sci.*, **39**, 2152–2158.

Evans, A.G., J.D. Locatelli, M.T. Stoelinga, and P.V. Hobbs, 2005: The IMPROVE-1 storm of 12 February 2001. Part II: Cloud structures and the growth of precipitation. *J. Atmos. Sci.*, **62**, 3456–3473.

Frei, C., and C. Schär, 1998: A precipitation climatology of the Alps from high-resolution rain-gauge observations. *J. Climatol.*, **18**, 873–900.

Fuhrer, O., and C. Schär, 2005: Embedded cellular convection in moist flow past topography. *J. Atmos. Sci.*, **62**, 2810–2828.

Fuhrer, O., and C. Schär, 2007: Dynamics of orographically triggered banded convection in sheared moist orographic flows. *J. Atmos. Sci.*, **64**, 3542–3561.

Garvert, M.F., C.P. Woods, B.A. Colle, C.F. Mass, P.V. Hobbs, M.T. Stoeling, and J.B. Wolfe, 2005: The 1314 December 2001 IMPROVE-2 event. Part II: Comparisons of MM5 model simulations of clouds and precipitation with observations. *J. Atmos. Sci.*, **62**, 3520–3534.

Hohenegger, C., D. Lüthi, and C. Schär, 2006: Predictability mysteries in cloud-resolving models. *Mon. Wea. Rev.*, **134**, 2095–2107.

Hohenegger, C., A. Walser, W. Langhans, and C. Schär, 2008: Cloud-resolving ensemble simulations of the August 2005 Alpine flood. *Quart. J. Roy. Meteor. Soc.*, **134**, 889–904.

Hong, S.Y., J. Dudhia, and S.H. Chen, 2004: A revised approach to ice microphysical processes for the bulk parametrization of clouds and precipitation. *Mon. Wea. Rev.*, **132**, 103 – 120.

Hong, S.Y., and J.O.J. Lim, 2006: The WRF single-moment 6-class microphysics scheme (WSM6). *J. Korean Meteor. Soc.*, **42**, 129–151.

Hong, S.Y., K.S.S. Lim, J.H. Kim, J.O.J. Lim, and J. Dudhia, 2008: Sensitivity study of cloud-resolving convective simulations with WRF using two bulk microphysical parameterizations: Ice-phase microphysics versus sedimentation effects. *J. Appl. Meteor.*, in press.

Houze, R., P.V. Hobbs, P.H. Herzegh, and D.B. Parsons, 1979: Size distributions of precipitation particles in frontal clouds. *J. Atmos. Sci.*, **36**, 156–162.

Houze, R., and S. Medina, 2005: Turbulence as a mechanism for orographic precipitation enhancement. *J. Atmos. Sci.*, **62**, 3599–3623.

Kain, J., and J. Fritsch, 1990: A one-dimensional entrainment/detrainment plume model and its application in convective parameterization. *J. Atmos. Sci.*, **47**, 2784–2802.

Kain, J., and J. Fritsch, 1993: *The representation of cumulus convection in numerical models*, Volume 24 of *Meteor. Monogr.*, Chapter Convective parameterization for mesoscale models: The Kain-Frisch scheme, pp. 29–32. Amer. Meteor. Soc.

Kessler, E., 1969: *On the distribution and continuity of water substance in atmospheric circulation*, Volume 10 of *Meteor. Monogr.* Amer. Meteor. Soc., 84 pp.

Kirshbaum, D.J., and D. Durran, 2004: Factors governing cellular convection in orographic precipitation. *J. Atmos. Sci.*, **61**, 682–698.

Kirshbaum, D.J., and D. Durran, 2005a: Atmospheric factors governing banded orographic convection. *J. Atmos. Sci.*, **62**, 3758–3774.

Kirshbaum, D.J., and D. Durran, 2005b: Observations and modeling of banded orographic convection. *J. Atmos. Sci.*, **62**, 1463–1479.

Levi, L., and M.E. Saluzzi, 1996: Effects of ice formation on convective cloud development. *J. Appl. Meteor.*, **35**, 1587–1595.

Lin, Y.L., D. Richard, and H. Orville, 1983: Bulk parametrization of the snow field in a cloud model. *J. Appl. Meteor.*, **22**, 1065–1092.

Medina, S., B. Smull, and R. Houze JR., 2005: Cross-barrier flow during orographic precipitation events: Results from MAP and IMPROVE. *J. Atmos. Soc.*, **62**, 3580–3598.

MeteoSchweiz, 2006a: Eine Länder übergreifende Niederschlags-Analyse zum August-Hochwasser 2005: Ergänzung zu Arbeitsbericht 211. *Arbeitsberichte der MeteoSchweiz*, **213**, 11.

MeteoSchweiz, 2006b: Starkniederschlagsereignis August 2005. *Arbeitsberichte der MeteoSchweiz*, **211**, 63.

Mlawer, E.J., S.J. Taubmann, P.D. Brown, M.J. Iacono, and S.A. Clough, 1997: Radiative transfer for inhomogeneous atmosphere: RRTM, a validated correlated-k model for the longwave. *J. Geophys. Res.*, **102**, 16 663–16 682.

Mudelsee, M., M. Borngen, G. Tetzlaff, and U. Grunewald, 2004: Extreme floods in central Europe over the past 500 years: Role of cyclone pathway "Zugstrasse Vb". *J. Geophys. Res.*, **109**, doi:10.1029/2004JD005034.

Pruppacher, H.R., and J.D. Klett, 1980: *Microphysics of cloud and precipitation.* D. Reidel publishing company, 714 pp.

Queney, P., 1948: The problem of airflow over mountains: A summary of theoretical studies. *Bull. Amer. Meteor. Soc.*, **29**, 16–24.

Randeu, W., K. Köck, and T. Leitner, 1996: Realisation of the Central European Weather Radar Network (CERAD). Final report, Technical University Graz, Austria.

Reisner, J., R.M. Rasmussen, and R.T. Bruintjes, 1998: Explicit forecasting of supercooled liquid water in winter storms using the MM5 mesoscale model. *Quart. J. Roy. Meteor. Soc.*, **124**, 1071–1107.

Roe, G., 2005: Orographic precipitation. *Annu. Rev. Earth Planet. Sci.*, **33**, 645–671.

Rotunno, R., and R. Ferretti, 2001: Mechanisms of intense Alpine rainfall. *J. Atmos. Sci.*, **58**, 1732–1749.

Schär, C., 2002: Mesoscale mountains and the larger-scale atmospheric dynamics: A review. In: *Meteorology at the Millennium*, pp. 29–42. Academic Press.

Schneidereit, M., and C. Schär, 2000: Idealized numerical experiments of Alpine flow regimes and southside precipitation events. *Meteor. Atmos. Phys.*, **72**, 233–250.

Skamarock, W.C., and J. Klemp, 1992: The stability of time-split numerical methods for the hydrostatic and the nonhydrostatic elastic equations. *Mon. Wea. Rev.*, **120**, 2109–2127.

Skamarock, W.C., J. Klemp, J. Dudhia, D. Gill, D.M. Barker, W. Wang, and J. Powers, 2005: A description of the Advanced Research WRF version 2. NCAR Technical note TN-468+STR, National Center for Atmospheric Research, USA.

Smith, R.B., 1979: The influence of mountains on the atmosphere. *Adv. Geophys.*, **27**, 87–230.

Stoelinga, M.T. and Coauthors, 2003: Improvement of microphysics parameterization through observational verification experiment. *Bull. Amer. Meteor. Soc.*, **84**, 1807–1826.

SwissRe, 2006: Natural catastrophes and man-made disasters 2005: high earthquake casualties, new dimension in windstorm losses. Sigma 2, SwissRe. 40 pp. [Available online at http://www.swissre.com].

Szyrmer, W., and I. Zawazki, 1999: Modeling of the melting layer. Part I: Dynamics and microphysics. *J. Atmos. Sci.*, **56**, 3573–3592.

Thompson, G., P. Field, R. Rasmussen, and W. Hall, 2008: Explicit forecasts of winter precipitation using an improved bulk microphysics scheme. Part II: Implementation of a new snow parametrization. *Mon. Wea. Rev.*, in press.

Thompson, G., R. Rasmussen, and K. Manning, 2004: Explicit forecasts of winter precipitation using an improved bulk microphysics scheme. Part I: Description and sensitivity analysis. *Mon. Wea. Rev.*, **132**, 519–542.

Trentmann, J. and Coauthors, 2008: Multi-model simulations of a convective situation in low-mountain terrain in central Europe. *Meteor. Atmos. Phys.*, doi: 10.1007/s00703–008–0323–6.

Tripoli, G., and W. Cotton, 1980: A numerical investigation of several factors contributing to the observed variable intensity of deep convection over South Florida. *J. Appl. Meteor.*, **19**, 1037–1063.

Unterstrasser, S., and G. Zängl, 2006: Cooling by melting precipitation in alpine valleys: An idealized numerical modelling study. *Quart. J. Roy. Meteor. Soc.*, **132**, 1489–1508.

Van Bebber, W.J., 1890: *Meteorologie*. Verlag von Ferdinand Enke, 391 pp.

Walko, R., W. Cotton, M. Meyers, and J. Harrington, 1995: New RAMS cloud microphysics parametrizations. Part I: The single-moment scheme. *Atmos. Res.*, **38**, 29–62.

Woods, C.P., M.T. Stoeling, J.D. Locatelli, and P.V. Hobbs, 2005: Microphysical processes and synergistic interaction between frontal and orographic forcing of precipitation during the 13 December 2001 IMPROVE-2 event over the oregon cascades. *J. Atmos. Sci.*, **62**, 3493–3519.

Woods, C.P., M.T. Stoeling, J.D. Locatelli, and P.V. Hobbs, 2007: The IMPROVE-1 storm of 12 February 2001. Part III: Sensitivity of a mesoscale model simulation to the representation of snow particle types and testing of a bulk microphysical scheme with snow habit prediction. *J. Atmos. Sci.*, **64**, 3927–3948.

Zängl, G., 2004: The sensitivity of simulated orographic precipitation to model components other than cloud microphysics. *Quart. J. Roy. Meteor. Soc.*, **130**, 1857–1875.

Zängl, G., 2007a: An adaptive vertical coordinate formulation for a nonhydrostatic model with flux-form equations. *Mon. Wea. Rev.*, **135**, 228–239.

Zängl, G., 2007b: Interaction between dynamics and cloud microphysics in orographic precipitation enhancement: A high-resolution modeling study of two north-Alpine heavy precipitation events. *Mon. Wea. Rev.*, **135**, 2817–2840.

Zängl, G., 2007c: To what extent does increased model resolution improve simulated precipitation fields? A case study of two north-Alpine heavy-rainfall events. *Meteor. Z.*, **16**, 571–580.

Appendix A

Statistical overview of simulations

Name	Domain	AVG	AVG_{sy}	AVG_{so}	RMSE	NAE
WSM6*_2_4	3	15.6	22.8	22.2	16.2	9.2
WSM6*_2	3	16.4	23.7		16.8	9.9
WSM6*_2_4	4	30.9	28.7	27.8	17.6	7.5
REF	4	27.3	25.7		17.9	8.8
WSM5*	4	26.5	25.1		17.4	8.5
THOM	4	21.6	20.2		19.5	11.5
THOM_GD	4	21.6	20.1		19.7	11.7
THOM2	4	21.5	20.2		19.5	11.5
KES	4	16.5	15.3		24.2	17.6
MAR	4	27.8	25.9		18.0	8.6

Table A.1: Statistics gained from WRF simulations and rain gauge measurements for the period between 0600 UTC 21 Aug and 0600 UTC 22 Aug 2005. For evaluation of the WRF domains 3 and 4 WRF output is interpolated to 2094 and 598 stations, respectively. A cubic interpolation has been chosen. Calculated parameters are the domain average of accumulated precipitation AVG, WRF station-averaged precipitation AVG_{sy}, observed station-averaged precipitation AVG_{so}, root mean squared error RMSE, and normalized absolute error NAE.

Name	Domain	AVG	AVG_{sy}	AVG_{so}	RMSE	NAE
WSM6*_2_4	3	11.1	29.1	27.0	21.9	13.4
WSM6*_2	3	11.7	30.6		23.9	15.3
WSM6*_2_4	4	50.1	52.6	57.6	31.1	15.9
REF	4	47.4	49.7		31.6	17.2
WSM5*	4	46.6	48.8		30.9	15.7
THOM	4	40.2	42.0		35.7	20.1
THOM_GD	4	40.2	41.7		36.1	20.6
THOM2	4	41.9	39.9		35.8	20.1
KES	4	34.5	35.4		40.3	25.6
MAR	4	48.2	50.2		32.3	17.6

Table A.2: As in Table A.1, but for the period between 0600 UTC 22 Aug and 0600 UTC 23 Aug 2005.

Appendix B

WRF code modification

In order to achieve an increased graupel production in the Thompson scheme, the transformation of snow to graupel is modified. The assumptions for this mass exchange process between the two hydrometeor species are shown in section 3.4.3. In the following the corresponding code modifications to the Thompson microphysics routine *module_mp_thompson.F* are described. The riming of snow, which is the same as the collection of cloud drops by snow, at model level k is expressed by the parameter *prs_scw(k)*. The depositional growth of snow is *prs_sde(k)* and $eps = 10^{-29}$ is a numerical threshold value. Finally, *g_frac* determines the fraction of snow, which is transformed to graupel. The modification implies that graupel is produced already for a ratio of three. Furthermore, the percentage of transformed rimed snow reaches from 25 % to 95 %, which is always at least 20 % more than in the original formulation. The remainder (1. - *g_frac*) accounts for the production of snow by riming. The terminal velocity of snow is unmodified and increases linearly with the degree of riming. Only the relevant part of the code is shown here:

```
!.. wolfgangl(2008): Increased graupel production from snow,
!.. vts_boost remains nearly unchanged
!.. A portion of rimed snow converts to graupel
!.. but some remains snow.
!.. Interp from 25 to 95% as riming factor increases
!.. from 3.0 to 30.0
!.. This remains ad-hoc and should
!.. be revisited.
```

```
      if (prs_scw(k).gt.3.0*prs_sde(k) .and. &
                   prs_sde(k).gt.eps) then
```

```
 r_frac = MIN(30.0D0, prs_scw(k)/prs_sde(k))
 g_frac = MIN(0.95, 0.25 + (r_frac-3.)*(0.95-0.25)/(30.-3.))

 vts_boost(k) = MIN(1.5, 1.1 + (r_frac-3.)*.016)
 prg_scw(k) = g_frac*prs_scw(k)
 prs_scw(k) = (1. - g_frac)*prs_scw(k)
endif
```

Acknowledgments

First of all, I would like to thank my advisor Alexander Gohm for his engagement in supervising this work and for helpful and interesting discussions. I also appreciate that he offered me the opportunity to attend the AMS Mountain Weather Conference in Whistler, which was a great experience. I am also grateful to Günther Zängl for his advice about running WRF.

Furthermore, I would like to acknowledge Cathy Hohenegger and Christoph Schär for getting the ball rolling by offering me the internship position at IAC. This internship awakened my interest in orographic precipitation and the August 2005 Alpine flood.

Here, I would also like to thank my family for their support during my time in Innsbruck. Especially, I am grateful to my brother Stephan and also to John, who both assisted me with proofreading this thesis. Finally, I am thankful to my friends and my girlfriend, who shared some funny moments with me in Innsbruck and the surrounding mountains.

Curriculum Vitae

Personal Details

Wolfgang Langhans
Hauptstrasse 32
83367 Petting
Germany
Email: wolfgang.langhans@student.uibk.ac.at

Born on November 27, 1983 in Traunstein, Germany

Education

10/08–11/09	Diploma thesis under the guidance of Dr. Alexander Gohm, Innsbruck: *"Cloud-resolving simulations of the August 2005 Alpine flood - The sensitivity to microphysics parameterizations"*
10/03–11/09	Meteorology and Geophysics, Leopold-Franzens-Universität, Innsbruck, Austria
09/94–05/03	Chiemgau-Gymnasium Traunstein, Germany, Abitur
09/89–06/94	Elementary school, Petting, Germany

Past activities and experiences

08/08	EMS Youth Scientist Travel Award 2008
08/08	13th AMS Mountain Meteorlogy Conference, Whistler, poster presentation: *Numerical sensitivity study of August 2005 Alpine flood*
08/08	AMS/COMET/MSC Mountain Weather Workshop, Whistler: *Bridging the Gap Between Research and Forecasting*
05/08	ECMWF training course, Reading: *Parametrizations of diabatic processes*
05/08 – 06/08	Work as tutor in the exercises to geophysical fluid dynamics, Innsbruck
03/08 – 04/08	Work as tutor in the exercises to theoretical meteorology II, Innsbruck

02/08	Internship at Max-Planck Institute for Meteorology, Hamburg, Germany: *Intercomparison of ECHAM5 and REMO simulations for climate scenario A1B*
07/07–09/07	Summer-Internship at IAC, ETH Zürich, Switzerland: *Dynamical aspects of August 2005 Alpine flood*
07/07	Convective and Orographically-induced Precipitation Study, Black Forest, Germany: *COPS summer school*

Publications

Hohenegger, C., A. Walser, W. Langhans, and C. Schär, 2008: Cloud-resolving ensemble simulations of the August 2005 Alpine flood. *Quart. J. Roy. Meteor. Soc.*, **134**, 889–904.

Langhans, W., and A. Gohm, 2008: Numerical sensitivity study of August 2005 Alpine flood (poster presentation)